UC Berkeley
UC Berkeley Electronic Theses and Dissertations

Title
Magnetism of Complex Oxide Thin Films and Heterostructures

Permalink
https://escholarship.org/uc/item/6fh476wk

Author
Iwata, Jodi

Publication Date
2012

Peer reviewed|Thesis/dissertation

Magnetism of Complex Oxide Thin Films and Heterostructures

by

Jodi Mari Iwata

A dissertation submitted in partial satisfaction of the

requirements for the degree of

Doctor of Philosophy

in

Engineering – Materials Science and Engineering

and the Designated Emphasis

in

Nanoscale Science and Engineering

in the

Graduate Division

of the

University of California, Berkeley

Committee in charge:

Professor Junqiao Wu, Chair
Professor Yuri Suzuki
Professor Ramamoorthy Ramesh
Professor Constance Chang-Hasnain

Fall 2012

Magnetism of Complex Oxide Thin Films and Heterostructures

Abstract

Magnetism of Complex Oxide Thin Films and Heterostructures

by

Jodi Mari Iwata

Doctor of Philosophy in Materials Science and Engineering

Designated Emphasis in Nanoscale Science and Engineering

University of California, Berkeley

Professor Junqiao Wu, Chair

Studies of magnetism at reduced scales have revealed new phenomena that are distinctly different from their bulk counterparts providing insight to the fundamental mechanisms that govern magnetism and other correlated properties. To this end, the use of heteroepitaxy and heterostructures is invaluable for investigating magnetism at reduced dimensions and at surfaces and interfaces. This dissertation is a compilation of investigations examining the magnetic properties of spinel-structure oxide thin films and heterostructures. Of particular interest are non-collinear spin systems as closely competing exchange interactions between magnetic moments give rise to a plethora of ground state degeneracies and phenomena inaccessible in the bulk.

The first part of this dissertation highlights the use of heteroepitaxial lattice distortions as a method to tune spin functionality and potentially lift ground state degeneracies more broadly in frustrated magnets. It discusses the first synthesis of heteroepitaxial thin films of the frustrated canted-moment ferrimagnet, $CuCr_2O_4$, and demonstrates the modification of exchange interaction strengths which results in greater collinear spin ordering and enhanced magnetization compared to the bulk. The data illustrates the sensitivity of the strong competing exchange interactions suggesting that strain is a promising instrument for perturbing the delicate balance of the exchange interactions in frustrated materials.

The second part of this dissertation probes magnetic proximity effects induced by interfaces and unconventional transport properties when $CuCr_2O_4$ is incorporated as a barrier layer in magnetic tunnel junctions comprised of ferromagnetic $La_{0.7}Sr_{0.3}MnO_3$ and Fe_3O_4 electrodes. It is surprising that a heterostructure composed entirely of magnetic materials can achieve distinct magnetic and resistive switching given the complexities present at the two barrier-electrode interfaces. Studies of the $CuCr_2O_4/Fe_3O_4$ interface again illustrate the delicate balance between exchange interactions as proximity effects by Fe_3O_4 are believed to modulate alignment in the Cr moments. Additionally, the bias dependence of JMR displays a local

minimum at zero bias which is believed to be the result of the Fe_3O_4 band structure and spin filtering properties of the $CuCr_2O_4$ barrier.

To my grandparents and the men of the 100th Infantry Battalion and 442nd Regimental Combat.
May your legacy live on forever.

Table of Contents

Chapter Four: La$_{0.7}$Sr$_{0.3}$MnO$_3$/CuCr$_2$O$_4$/Fe$_3$O$_4$ Magnetic Tunnel Junctions

All of the acronyms are defined in the text of this dissertation. However, this provides a source of the most common acronyms and definitions

AFM	Atomic force microscopy
ALS	Advanced Light Source
CCO	$CuCr_2O_4$
CFO	$CoFe_2O_4$
JMR	Junction magnetoresistance
LAO	$LaAlO_3$
LBNL	Lawrence Berkeley National Laboratory
LSMO	$La_{0.7}Sr_{0.3}MnO_3$
MAO	$MgAl_2O_4$
MR	Magnetoresistance
NFO	$NiFe_2O_4$
PIXE	Particle induced X-ray emission
PLD	Pulsed laser deposition
RBS	Rutherford backscattering spectroscopy
RMS	Root-mean-square
SQUID	Superconducting quantum interference device
SRO	$SrRuO_3$
SSRL	Stanford Synchrotron Radiation Lightsource
STO	$SrTiO_3$
TEY	Total electron yield
XA	X-ray absorption
XMCD	X-ray magnetic circular dichroism
XRD	X-ray diffraction

I would like to begin by thanking my advisor, Yuri Suzuki, for giving me the opportunity of a lifetime. The opportunity to do graduate research at U.C. Berkeley and the collaborations you have so generously facilitated were beyond this simple girl's wildest dreams. I will always be grateful.

To my closest counterparts: Virat Mehta, Franklin Wong, and Urusa Alaan. The many late nights spent with you brought ideas to life, and helped me through the most difficult parts of graduate school. Thanks for being such a special part of my graduate school career.

To those who mentored me as a green post-baccalaureate engineering student: Emily Allen, Kyeongjae Cho, Luisa Bozano, Campbell Scott, Ayusman Sen, Guohan Hu, and David Braunstein. I have never forgotten how much your words of encouragement, and in some cases tough love, meant to me. Never in a million years did I think that my first REU at Stanford would have led me here. The journey has been a thrill.

To my former lab members: Rajesh Chopdekar, Brittany Nelson-Cheeseman, and Joanna Bettinger. Thanks for your patience and helping me get going.

To my Nanolab friends and heterostructure buddies: Long Yu, Morgan Trassin, David Carlton, Patrick Bennett, Marie Mayer, Amit Lakhani, Roger Chen, Peter Matheu, and Yi Rao. Thanks for making heterostructure growth and junction fabrication just a little bit easier.

To my collaborators Kin Man Yu, Brian Kirby, Julie Borchers, Marco Liberati, Kate Jenkins, Michael Toney, and Elke Arenholz. Thanks for making much of this work possible.

To my current lab members: Matthew Gray, Alex Grutter, Ted Sanders, and Charles Flint. Thanks for being the muscles that helped me move dewars and finish up. Best of luck to you all.

To my friends who have checked in to make sure I was still alive, fed me home-cooked dinners, and sat through my practice qual talks. Thanks much!

To my parents and sister. Thank you for your unconditional love and support throughout the years. You've always encouraged me to follow my dreams and give everything 110%. Much of my success is due to you. I hope that I have made you proud.

Finally, to my husband, Shane, thanks for being my partner in this journey. Without complaint or hesitation, you've generously supported my many late work nights and weekends away from home. Your curiosity has always inspired me and I have so often wondered why I am the graduate student and not you. We've discovered so much about each other and I know this would not have been possible without you.

In the middle of difficulty lies opportunity

-   Albert Einstein

Magnetism has fascinated civilization for thousands of years with stories of the peculiar properties of lodestone being dated as far back as the first century B.C. In the present day, magnetism continues to fascinate society with levitating trains and ever increasing information storage capabilities. Magnetic oxides are a class of magnetic materials that have attracted much attention for their wide range of electrical, optical and magnetic properties. This is in large part due to the ease at which they can be chemically doped leading to an expansive range of compositional differences. This chapter presents the basic concepts and nuances of magnetism in $3d$ transition metal oxides. In particular, the chapter describes the crystal chemistry and ferrimagnetism in the spinel crystal structure.

§1.1 Introduction

Complex oxides are a broad class of materials the possess charge, spin, orbital, and lattice degrees of freedom. Complexity reflects the intimate coupling and strong interactions between these different degrees of freedom that have given rise to collective phenomena like superconductivity and multiferroicity. A central theme in this dissertation is magnetism, another collective phenomenon, which has strong electron correlations that align the spin axes of different electrons relative to one another. Magnets have been technologically significant for motors, generators, sensors, and data storage. However, unlike silicon-based technology, magnet-based technologies have not scaled well because magnetism at reduced dimensions at surfaces and interfaces is not completely understood. This is in part due to the enormous complexities associated with correlation effects that make magnetism difficult to study. However, it is also this complexity in spinels that has given rise to spinel oxide half-metals, ferrimagnetic insulators, and superconductors which have tremendous potential in spin-based electronics.

Ongoing studies of magnetism at reduced scales have revealed emergent new phenomena that have tremendous technological potential. To harness this potential hinges on our ability to exercise control at reduced scales. Advances in thin film synthesis can realize film growth with near atomic precision and form atomically sharp interfaces. In addition, advances in characterization and fabrication techniques allow for probing the properties in such reduced dimension systems. To this end, the use of heteroepitaxy and heterostructures has been invaluable for investigating magnetism at reduced dimensions and at surfaces and interfaces. Together these techniques have revealed thin film and interfacial magnetism properties distinctly different from their bulk counterparts, thus providing deeper insight regarding the fundamental mechanisms that govern magnetism and other correlated properties.

In particular, this dissertation examines the nature of ferrimagnetism in spinel structure $3d$ transition metal oxides (Figure 1.1). Ferrimagnets are often described as being ionic solids.

This leads to highly localized electrons that give rise to insulating properties. However, in transition metal oxides the directional nature of the valence d orbitals finds that their bonds with O^{2-} anions have a degree of covalent character implying that the d electrons are not truly localized. Thus, it is more accurate to describe the bonding in spinels as predominantly ionic with partial covalent character. Note that the term "localized" is used with respect to the valence orbital electrons as the d orbitals are more localized to the nucleus of the transition metal ion than the s and p orbitals, but much less so when compared to the core orbitals.
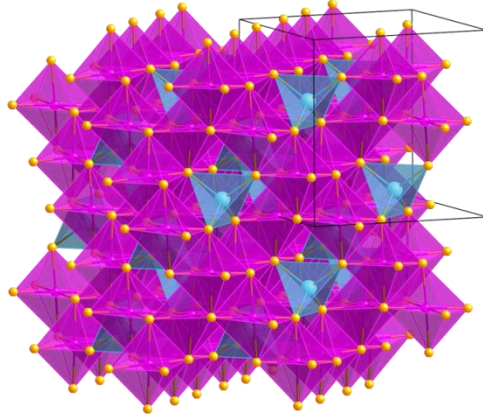
Figure 1.1. The spinel (MN_2O_4) oxide crystal structure is composed of oxygen anions (yellow, not drawn to scale) which form a face-centered cubic lattice. Within the oxygen lattice, cations occupy the octahedral (fuschia) and tetrahedral (periwinkle) interstitial sites. The black cube outlines one spinel unit cell.

§1.2 The Pauli Exclusion Principle and Hund's Rules

Electron localization allows us to examine magnetism in oxides using a single ion model. Similar to a free ion, the energy levels are discrete and an integral number of electrons can be associated with an ion. This is fortuitous because while I am concerned with a many-body system, the fundamental magnetic and electronic properties can be understood through a more simplistic picture.

The Pauli exclusion principle and Hund's rules provide a set of fundamental concepts for understanding the method in which electrons occupy orbitals.[1-4] The Pauli exclusion principle dictates that no two electrons can have the same set of quantum numbers (n, l, m_l, m_s). In accordance with the Pauli exclusion principle, Hund's rules consist of three rules that govern the arrangement of electrons in the p-, d- and f- orbitals of free atoms in order to identify the lowest energy electron spin configuration. These rules assume that spin-orbit coupling is weak, and the individual spin and orbital angular momenta are strong. The first rule is concerned with spin arrangement in order to maximize the total electron spin, S. By placing electrons in different orbitals with parallel spins they are as far apart as possible effectively minimizing Coulombic repulsion. The second rule seeks to maximize the total orbital angular momentum, L. Each time two electrons approach one another the Coulomb energy of the system increases.

If these electrons are orbiting in the same direction, it reduces the frequency at which they meet when their orbital paths cross. Finally, the third rule takes into account the coupling interaction between L and S with its origin being the spin-orbit coupling of an electron. It asserts that the lowest energy electronic configuration is that which gives the lowest total spin and orbital angular momenta, J. If the electron filling of the energy levels is more than half-filled, $J = L + S$. If the electron filling of the energy levels is less than half-filled, $J = |L - S|$.

While Hund's rules were developed for a free atom it can also be applied to a solid or many-body system in which the electrons of the constituent atoms are highly localized leading to discrete energy levels like that of a free atom. For ionic solids, we can use a modified version of Hund's rules to predict the spin arrangement and magnetic properties of the constituent magnetic cations. In accordance with the Pauli exclusion principle, spins in a partially filled shell are arranged to produce the maximum spin imbalance. The difference for a free atom versus a $3d$ transition metal cation is that the presence of the electric field generated by the surrounding ions often quenches the orbital angular momentum contribution ($L = 0$) resulting in $J = S$. Quenching, the result of strong orbital-lattice coupling, prevents the orbitals from reorienting themselves along the direction of an applied field. As a result, they are considered to provide no contribution to the observed magnetic moment.

§1.3 Crystal Field Theory and Its Extensions
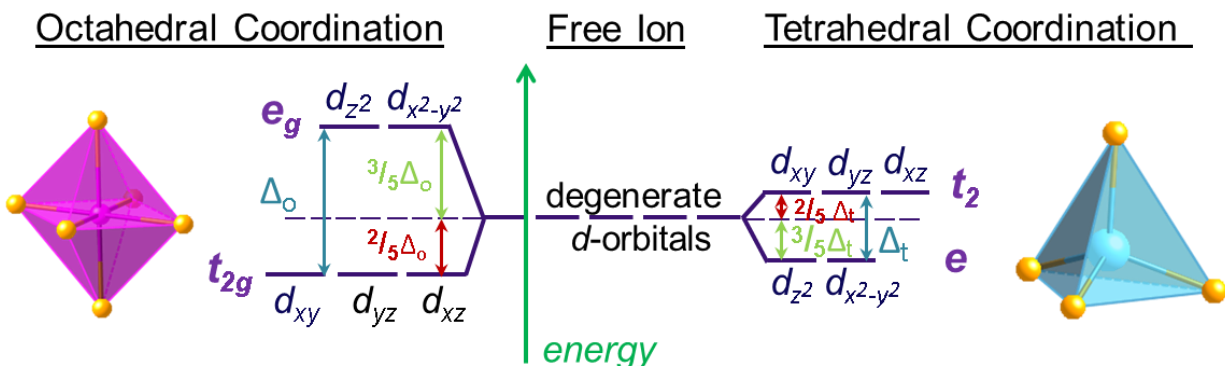
Figure 1.2. A comparison of the relative energies due to crystal field splitting for a $3d$ transition metal cation in octahedral and tetrahedral environments.

The next few sections are intended to present the fundamental concepts necessary to understand the material presented in this dissertation, including crystal field theory, differing spin states, Jahn-Teller distortions, the spinel crystal structure, and exotic spin configurations. To begin, I employ crystal field theory. While crystal field theory is based on an ionic model, and neglects covalent bonding character, it provides a qualitative description of transition metal oxides.

Consider an isolated $3d^n$ transition metal cation as shown in Figure 1.2. The energy levels associated with its d orbitals are fivefold degenerate. When placed in a crystal field, the

$3d$ valence electrons feel the electrostatic field created by the oxygen ligands, and the energy is raised due to the Coulombic repulsion between the valence electrons of the cation and surrounding ligands. The reduced symmetry finds that the energy of the system is lowered by lifting the fivefold degeneracy of the d orbitals and splitting them into two energy levels: a triply degenerate level consisting of the d_{xy}, d_{yz}, and d_{xz}, orbitals and a doubly degenerate level consisting of the d_{z2} and d_{x2-y2} orbitals.

The symmetry of the crystal field affects the relative positions of the energy levels.[5] This can be understood for the octahedral and tetrahedral symmetries by visualizing the orientation of the d orbitals together with their oxygen ligands. In an octahedral environment, the transition metal cation is surrounded by six nearest neighbor ligands. In this coordination, Figure 1.2 shows that the d orbitals split into lower energy t_{2g} orbitals and higher energy e_g orbitals adopting the electronic configuration $(t_{2g})^m(e_g)^n$ where m and n are integers and t_{2g} and e_g are group symmetry notation. The t_{2g} orbitals consist of the d_{xy}, d_{yz}, and d_{xz} orbitals, and the e_g orbitals consist of the d_{z2} and d_{x2-y2} orbitals. Representing the oxygen ligands as point charges (purple circles), their spatial position is shown in Figure 1.3 with respect to the three coordinate axes, x, y, and z for each d orbital. The e_g orbitals point directly at the ligands where the crystal field is greatest: d_{z2} points along the z axis, and d_{x2-y2} points along the x and y axes. The t_{2g} orbitals, d_{xy}, d_{yz}, and d_{xz}, do not point along the coordinate axes, but rather in between them, where the field is weaker. Stronger crystal field effects due to their atomic arrangement creates greater electrostatic repulsion between the electrons of the e_g orbitals and ligands. This raises their potential energy making them energetically less stable than the stabilized t_{2g} orbitals which have lower energy because of smaller crystal field effects.

In tetrahedral symmetry, a cation is surrounded by four negative anions. The crystal field also splits the fivefold degenerate d orbitals into triply and doubly degenerate energy levels as shown in Fig. 1.2. However, the relative positions of these energy levels are reversed. The d orbitals split into lower energy e orbitals and higher energy t_2 orbitals adopting the electronic configuration $(e)^p(t_2)^q$ where p and q are integers. Fig. 1.4 shows that the t_2 orbitals are in closer proximity to the ligands which point towards the midpoint of the cube edges than the e orbitals which point towards the center of the cube faces. Similar to the discussion presented for an octahedral crystal field, the greater Coulombic repulsion between the electrons of the t_2 orbitals and ligands leads to their higher energy compared to the e orbitals. In fact, with tetrahedral symmetry no d orbital lobes point directly at a ligand. This is important as it provides insight regarding the energy separation between the t_2 (t_{2g}) and e (e_g) orbitals with tetrahedral (octahedral) symmetry. This separation known as the crystal field splitting (Δ) varies in magnitude for octahedral (Δ_o) and tetrahedral (Δ_t) symmetry. As can be seen in Figure 1.2, $\Delta_t < \Delta_o$ such that calculations have found a Δ_t/Δ_o ratio of 4/9.[6] In tetrahedral symmetry, the d orbitals point in directions where the crystal field is even less than that of the octahedral t_{2g} orbitals leading to a smaller crystal field splitting.

t_{2g}

d_{xy} d_{xz} d_{yz}

e_g

d_{z^2} $d_{x^2-y^2}$
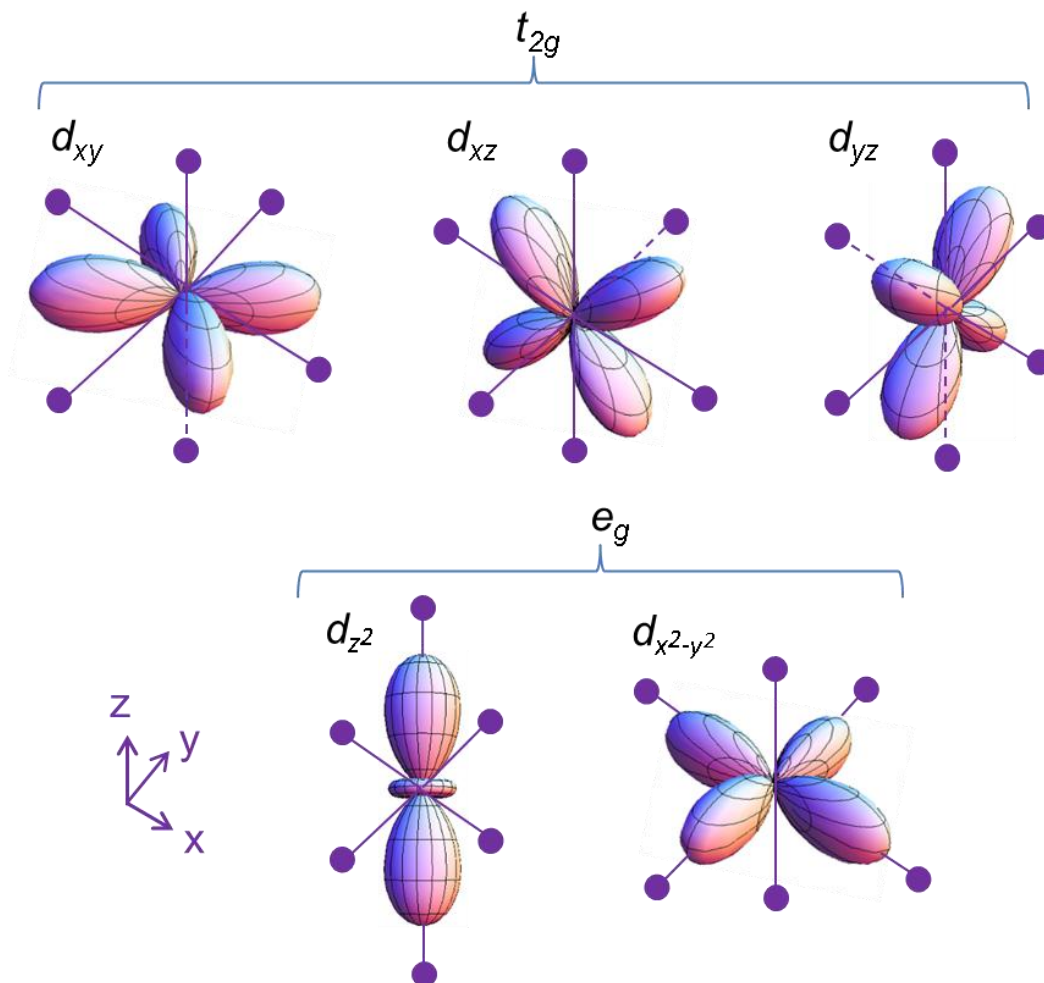
Figure 1.3. Schematic depicting the orientation of the d orbitals in an octahedral crystal field. Oxygen ligands are represented as point charges (purple circles). The x, y, and z axes are orthogonal.

t_2 e

d_{xy} $d_{x^2-y^2}$ d_{z^2}
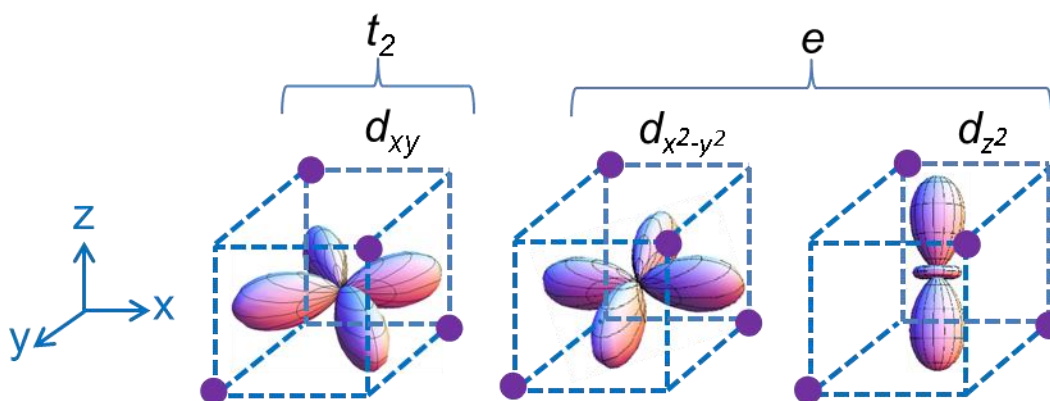
Figure 1.4. Schematic depicting the orientation of selected d orbitals in a tetrahedral crystal field with point charges (purple circles) representing the oxygen ligands.

Until this point I have neglected contributions from covalent bonding in the transition metal cation-oxygen bond. The shortcomings of this assumption affect the crystal field splitting energy and provide an incomplete picture of the bonding. While the bond is mostly ionic, covalent bonding is present. One limitation of crystal field theory is the inaccurate prediction of the energy separation between the two orbital sets often referred to as the crystal field stabilization energy. While crystal field theory provides an estimate, covalent bonding must be considered to provide a more accurate separation energy value. For a cation with octahedral symmetry, its electronic configuration $(t_{2g})^m(e_g)^n$ is used to determine the crystal field stabilization energy from the relation $\Delta(4m-6n)/10$. For a cation with tetrahedral symmetry, its electronic configuration $(e)^p(t_2)^q$ is used to determine the crystal field stabilization energy with $\Delta(6p-4q)/10$. However, corrections to account for covalency find that the Δ_t/Δ_o ratio changes although 4/9 remains a good approximation.
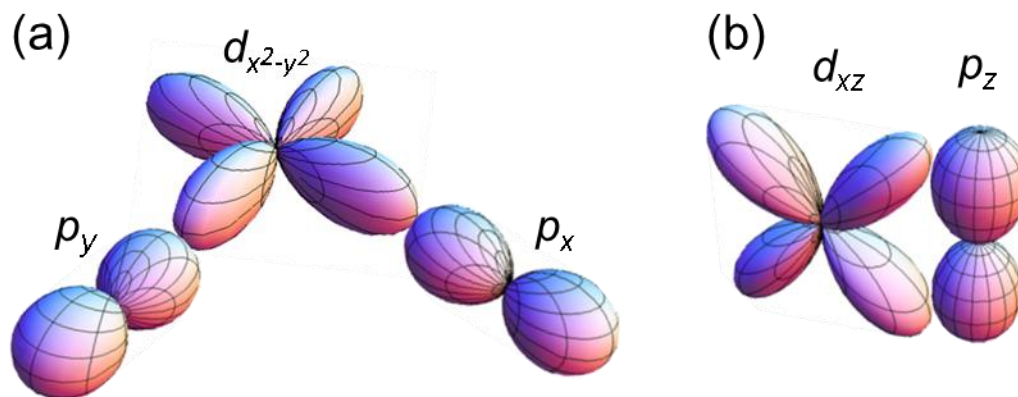
Figure 1.5. (a) Schematic depicting the interaction between an e_g orbital and its ligands represented by the d_{x2-y2} and p_x and p_y orbitals. The direct overlap between these orbitals indicates strong interactions and σ bonding. (b) Schematic depicting the interaction between a t_{2g} orbital and a ligand represented by the d_{xz} and p_z orbitals. The indirect overlap between these orbitals results in weaker interactions and π bonding.

Molecular orbital theory provides a more accurate depiction of the bonding in these transition metal oxides.[7] Using a delocalized electron approach, it treats the bond between the transition metal cation and ligands as being essentially covalent and considers the role of orbital overlap. This modifies the treatment of the ligands as point charges, and instead considers the shape of the ligand bonding orbitals. As an example, I show the octahedral field as its symmetry allows for easy depiction of the overlap. Figure 1.5(a) illustrates the strong overlap between an antibonding e_g orbital and ligands represented by the d_{x2-y2} and the p_x and p_y orbitals. As the lobes point directly at each other, the interaction between them is greatest and indicative of σ bonding. Figure 1.5(b) illustrates indirect overlap between an antibonding t_{2g} orbital and ligand represented by the d_{xz} and p_z orbitals. This type of overlap is indicative of π bonding.

The reduced symmetry of tetrahedral fields makes such an illustration more complicated. The antibonding t_2 orbitals form σ bonds with its ligands. However, bonds between the antibonding e orbitals and their ligands are a mix of σ and π bonding since π bonding is not independent of σ bonding.

The lowest energy spin configuration becomes a competition between the crystal field energy and Hund's energy which act to keep parallel alignment between spins. For an octahedrally-coordinated cation, the order in which orbital filling occurs is unambiguous for d^1 to d^3 systems and for d^8 to d^{10} configurations. For all other systems, there is a potential for ambiguity associated with the order of orbital filling depending on the strength of the crystal field. At the extremes, as illustrated in Figure 1.6 for a d^5 octahedral configuration, a weak field (small crystal field energy) is synonymous with a high spin state in which spin-up electrons half-fill the lower energy orbitals then jump to and begin populating the higher energy orbitals maximizing the number of unpaired electrons. For a strong field (large crystal field energy), the competition between the crystal field and Hund's energies stabilizes a low spin state as an electron would prefer to pair up with the electrons in the lower lying, half-filled energy orbitals rather than incur the energy cost of overcoming the large crystal field energy in order to populate the higher energy orbitals. In between these extremes are systems in which the Hund's coupling and crystal field energy are closely competing and small external perturbations like temperature, pressure, and strain can push a system into high, low, or intermediate spin states. This phenomena lies at the heart of spin state transitions research which have given rise to the discovery of new and exciting properties in complex oxides.
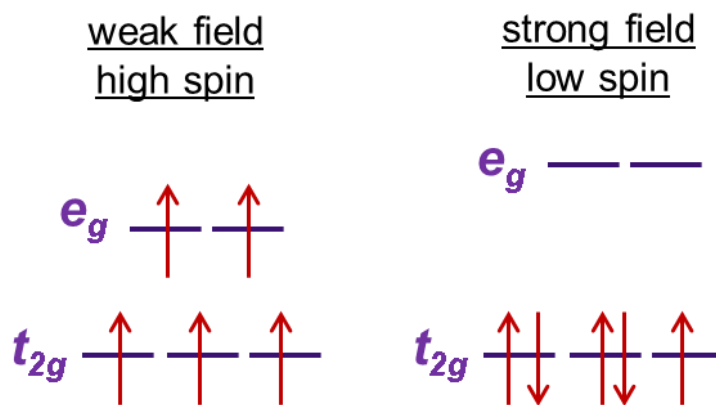
Figure 1.6. Schematic of the d orbital occupancy for a d^5 configuration with octahedral symmetry for the weak field and strong field cases.

Finally, for tetrahedrally-coordinated cations, orbital filling is unambiguous for d^1, d^2 and d^7 to d^{10} configurations. However, as a consequence of the Δ_t / Δ_o ratio of 4/9 it is thought that the small crystal field splitting in tetrahedral complexes makes them exclusively weak field complexes.[4]

§1.4 The Jahn-Teller Theorem

The simple picture described above of the electronic states can be modified by lattice distortions in the form of a Jahn-Teller effect. [Another facet that has given rise to interesting phenomena are structural distortions due to Jahn-Teller effects.] According to the Jahn-Teller theorem, if the electronic state of a non-linear molecule is orbitally degenerate, then there is at least one vibrational coordinate along which the molecule may distort to lower its energy. Physically, this can be understood by through an example with octahedrally-coordinated Jahn-Teller active $3d^9$ Cu^{2+} with a $(t_{2g})^6(e_g)^3$ ground state. If the four ligands in the xy plane move towards the Cu^{2+} ion while the two ligands along the z axis move away from the Cu^{2+} ion, then by electrostatics the d_{z2} orbital becomes stabilized and d_{x2-y2} is destabilized. Splitting of the lower t_{2g} orbitals also occurs accordingly. This distortion reduces the symmetry of the octahedron leaving one electron in the d_{x2-y2} orbital. Simultaneously, the distortion stabilizes the system and distortions proceed until the extra stability gained is balanced by the energy required to stretch and compress the bonds. The magnitude of the Jahn-Teller distortion depends on the bonding or antibonding power of the degenerate electrons.[8] Small splitting of the degenerate nonbonding orbitals leads to small distortions from the existing symmetry. Large distortions are expected from the increased splitting associated with removing the degeneracy of the antibonding orbitals. For octahedral sites, this occurs in the d^4 and d^9 configurations which have unpaired electrons occupying the e_g orbitals. In tetrahedral sites, unpaired electrons in the t_2 orbitals are expected to yield the largest distortions. This includes the d^3, d^4, d^8, and d^9 configurations.

§1.5 The Spinel Crystal

Much of what has been discussed thus far has been aimed at developing the basics of the spinel crystal structure (Figure 1.1). Spinel, the mineral name for $MgAl_2O_4$, has the chemical formula $(MO{\cdot}N_2O_3)$ MN_2O_4. It requires eight formula units and 56 ions to display the full symmetry of the unit cell. Oxygen anions form a face-centered cubic lattice. Within this lattice, cations occupy the octahedral (fuschia) and tetrahedral (periwinkle) interstitial sites. The open nature of the spinel crystal is attributed to the large number of interstitial site vacancies as only eight of the 64 tetrahedral sites and 16 of the 32 octahedral sites are occupied.

The distribution of cations is an important degree of freedom in spinels. Site occupancy is governed by its site preference energy which is derived from cation size, valence, and the strength of the crystal field.[9,10] The octahedral site preference energies reported from different computational and experimental methodologies in Figure 1.7 show that Zn^{2+} has the strongest preference to occupy the tetrahedral interstitial sites, and Cr^{3+} has the strongest affinity to occupy the octahedral interstitial sites. The inversion parameter, υ, represents the fraction of M cations that occupy the octahedral sites, and is based on a continuum ranging from 0 to 1. On one end of the continuum, $\upsilon = 0$ corresponds to a *normal* spinel crystal, $M^{2+}[N^{3+}]_2O_4$, where the square brackets identify the cations that occupy the octahedral sites. For a normal spinel, the M^{2+} cations occupy the tetrahedral sites, and the N^{3+} cations occupy the octahedral sites. At the opposite end of the continuum, spinel crystals with $\upsilon = 1$ are referred to as *inverse* spinels, $N^{3+}[M^{2+}N^{3+}]O_4$. In inverse spinels, M^{2+} cations sit in the octahedral sites and the N^{3+} cations are equally divided between the octahedral and tetrahedral sites. Mixed spinels are those which do

not have a strong tendency for their cations to arrange themselves in a normal or inverse distribution. They are cited with their inversion parameter, υ.
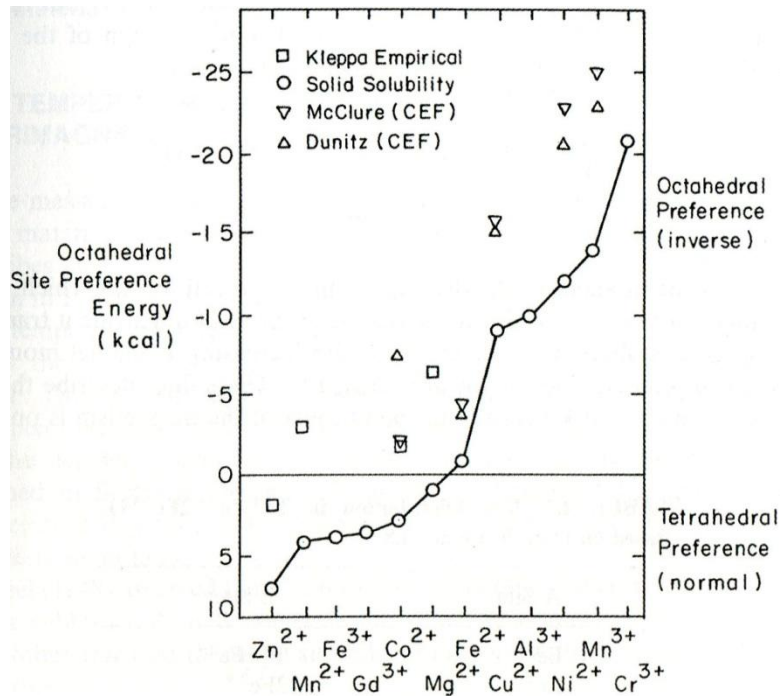
Figure 1.7. The distribution of octahedral site preference energies for cations known to populate the spinel crystal. [Navrotsky and Kleppa, adapted by O'Handley][9,10]

While many spinel crystals are cubic, there are many notable distortions from cubic symmetry. Spinels with tetragonal symmetry have been stabilized in crystals containing Jahn-Teller active cations. Knowing a cation's electronic structure and site occupancy preference allows for the identification of systems that are likely to undergo a Jahn-Teller distortion. For example, based on its electronic structure, it can be predicted that Jahn-Teller active $3d^9$ Cu^{2+} and $3d^4$ Mn^{3+} will lead to distortions when occupying either the octahedral or tetrahedral interstitial sites in a crystal; whereas a distortion is predicted only for tetrahedrally-coordinated $3d^8$ Ni^{2+}. I briefly list spinels which exhibit Jahn-Teller induced distortions due to the presence of these aforementioned Jahn-Teller active cations: $CuFe_2O_4$, $CuCr_2O_4$, $CuMn_2O_4$, $NiCr_2O_4$, Mn_3O_4, and $ZnMn_2O_4$.

§1.6 Ferrimagnetism

When magnetic cations occupy the interstitial sites of the spinel structure, they give rise to a wide array of magnetic properties. For magnetitians, the spinel crystal structure is ubiquitous with the ferrites, AFe_2O_4, and ferrimagnetism. This is not by chance as the ferrites have been the most historically and technologically important class of ferrimagnets.
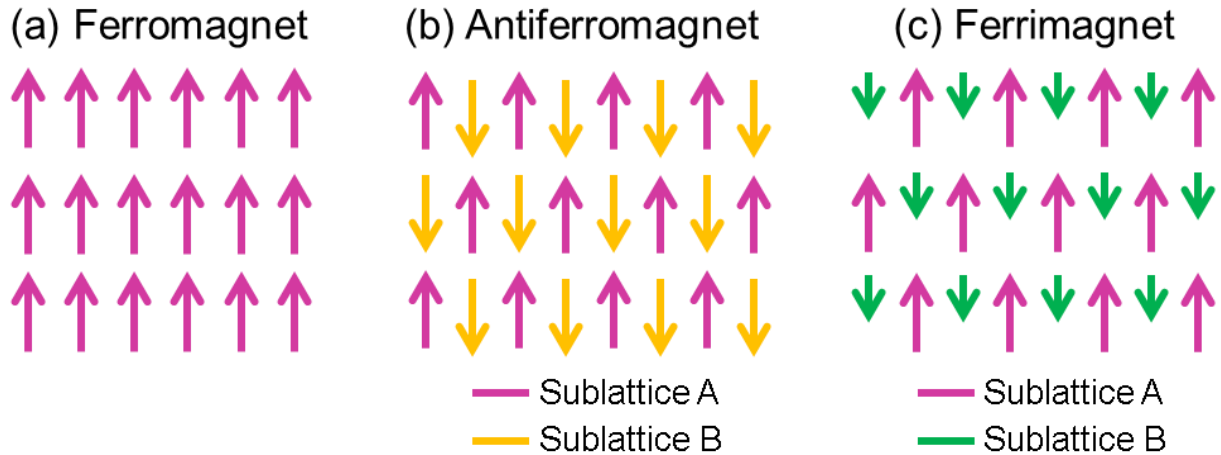
Figure 1.8. Long-range magnetic moment ordering for a (a) ferromagnet, (b) antiferromagnet, and (c) ferrimagnet. These magnetic classes exhibit spontaneous ordering of the moments below a critical temperature.

Ferrimagnetism displays properties of both ferromagnetism and antiferromagnetism. Beneath a critical temperature, Figure 1.8 shows that all three magnetic classes exhibit spontaneous long-range ordering of the magnetic moments. This ordering is the result of strong interactions between the magnetic moments attributed to the existence of a large internal molecular field, H_W. The magnetic moments in a ferromagnet exhibit parallel alignment. For antiferromagnets and ferrimagnets, nearest neighbor magnetic moments exhibit antiparallel alignment. Developed as an extension of Néel's theory of antiferromagnetism, the theory of ferrimagnetism utilizes the concept of two interpenetrating sublattices denoted as sublattice A and sublattice B. Each sublattice has its own magnetization, M_A and M_B, respectively, which is the product of the composition of each sublattice and its average magnetic moment. The total magnetization is the difference calculated by $M = |M_A| - |M_B|$. For an antiferromagnet, sublattice A and B are structurally identical such that $M_A = M_B$. This yields perfect cancellation of the magnetization and zero net moment. For a ferrimagnet, the A and B sublattices are structurally non-identical such that $M_A \neq M_B$. This results in imperfect cancellation of the magnetization and a non-zero net moment.

The molecular field comes from quantum mechanics and is a construct to describe exchange interactions, but is in fact a fictitious field within a mean field approximation. Primarily electrostatic in origin and a direct consequence of the Pauli exclusion principle, it is concerned with the orientation of electron spins and tends to align them parallel to each other. To account for the magnetization of each sublattice requires consideration of two molecular fields as shown in equations 1.1 and 1.2. [1]

The molecular field acting on the A sublattice is

$$H_W^A = \gamma_{AA} M_A - \gamma_{AB} M_B .$$
(1.1)

The molecular field acting on sublattice B is

$$H_W^B = \gamma_{BB} M_B - \gamma_{AB} M_A, \tag{1.2}$$

where γ represents the molecular field constant.

For the molecular field acting on sublattice A described in equation 1.1, there are contributions from interactions between moments within the A sublattice (first term) and interactions between neighboring moments on the opposing sublattice (second term).

For a ferrimagnet, the critical temperature is known as the Curie temperature (T_C). I will limit my background discussion on ferrimagnetism to the magnetic properties below T_C as this is the temperature regime in which my research has been performed. Above T_C, thermal agitation overwhelms the moment alignment resulting in paramagnetism. Below T_C, the magnetization for each sublattice is

$$M_A = Nm_A B(J, \frac{\gamma_{AA} M_A - \gamma_{AB} M_B}{k_B T}) \tag{1.3}$$

$$M_A = Nm_A B(J, \frac{\gamma_{AA} M_A - \gamma_{AB} M_B}{k_B T}), \tag{1.4}$$

where N = number of atoms/unit volume, m = magnetic moment along the field direction, B = the Brillouin function, and J = total angular momentum.

The magnetization of each sublattice has its own characteristic temperature dependence. This is dependent on variables such as the cation distribution and molecular field constants. However, equations 1.3 and 1.4 also indicate that the magnetization of each sublattice is dependent on the other. This mutual dependence requires that the sublattices must have the same Curie point. Different Curie points would mean that once the magnetization of one sublattice reaches zero, it could no longer align the moments on the second sublattice thus preventing it from ordering. This is an important point for the temperature-dependent ordering of magnetic moments in ferrimagnets especially when interpreting temperature-dependent magnetic data from element-specific techniques such as X-ray magnetic circular dichroism.

Finally, as cation distribution creates a large range of structural possibilities in spinel oxide crystals, it simultaneously adds greater complexity to the observed ferrimagnetism. The non-identical lattices require the consideration of at least three different exchange interactions: exchange between moments on sublattice A (A-A), exchange between moments on sublattice B (B-B), and exchange between moments on sublattice A and B (A-B). It is clear from the schematic in Figure 1.8(c) that the A-B exchange is antiferromagnetic. However, there is a subtlety in the nature of the A-A and B-B exchange within each sublattice. While it appears that the exchange within each sublattice is ferromagnetic due to the observed ferromagnetic alignment, the exchange is actually *antiferromagnetic*. The exchange energy comes from the exchange Hamiltonian, $H_{ex} = -\Sigma J_{ij} S_i \cdot S_j$. In particular we focus on the sign and magnitude of the exchange integral, J_{ij}. When $J < 0$, the exchange is antiferromagnetic. When $J > 0$, the exchange is ferromagnetic. For ferrimagnets, $J_{ij} < 0$ for all exchange interactions.

Collinear Néel moment configuration
$|J_{AB}| \gg |J_{BB}|, |J_{AA}|$
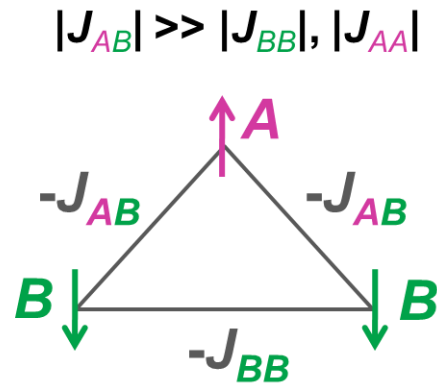
Figure 1.9. Spin arrangement for the three magnetic cations in a spinel formula unit under the exchange interaction conditions for the collinear Néel configuration or conventional ferrimagnet.

For ferrimagnetic spinels, the formula unit MN_2O_4 allows for up to three magnetic cations per formula unit. The triangle-based moment geometry imposed by the crystal structure is represented by Figure 1.9. This depicts the exchange between the three magnetic cations in a collinear Néel configuration more commonly known as the conventional ferrimagnet. To achieve this configuration, the exchange condition required is $|J_{AB}| \gg |J_{BB}|, |J_{AA}|$. Here the magnitude of the A-B exchange interaction is much larger than the A-A and B-B interactions. Note that the triangle-moment geometry depicts the magnetic moments for one formula unit and as a result no A-A interactions are shown. In crystal lattices, the large proximity between the A sites results in weak exchange leading to their negligible contribution to the total exchange energy. For this reason, A-A interactions are neglected in further discussion. The ground state moment configuration is that which minimizes the overall energy of the system. Because J_{AB} is so much larger than J_{BB}, the ground state configuration is achieved by satisfying the antiferromagnetic A-B exchange term and incurring the energy cost of stabilizing parallel alignment of A-A and B-B moments. As a result, the moments between the A and B sublattice exhibit antiparallel, antiferromagnetic alignment, and the moments within the A sublattice and the moments within the B sublattice exhibit parallel, ferromagnetic-like alignment.

§1.7 Frustrated Magnetism

Within the premises of the classical Heisenberg Model, an interesting area of condensed matter physics emerges when the condition for the collinear Néel alignment does not hold, and the antiferromagnetic exchange integrals, J_{AA}, J_{AB}, and $J_{BB,}$ are on the same order of magnitude no longer dominated by J_{AB}.[11] A competition arises between the different exchange interactions, and the three exchange interactions cannot be simultaneously satisfied. This leads to the condition known as frustrated magnetism as the magnetic moments are unable to order and find themselves arranged in a configuration shown in Figure 1.10.

Frustrated moment configuration

$$|J_{AB}| \sim |J_{BB}|$$
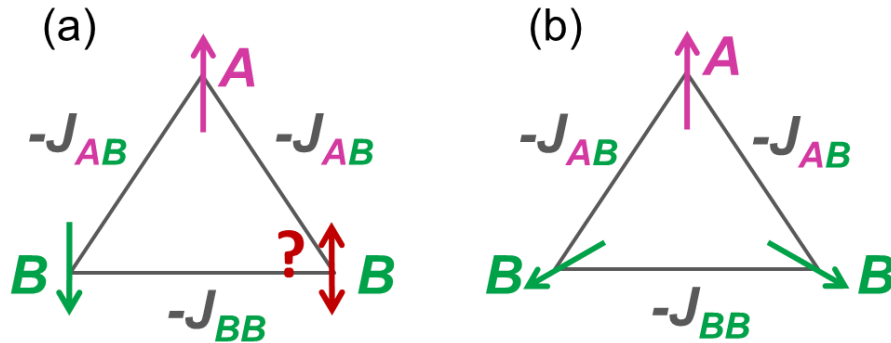
Figure 1.10. Spin arrangement for the three magnetic cations in a spinel formula unit under the exchange interaction conditions for frustrated magnetism. (a) Without a dominant exchange interaction, it is impossible to simultaneously satisfy all three exchange interactions as the third moment cannot order. (b) Instead the moments cant to achieve the lowest energy state possible.

As the frustration is explained with reference to the triangle-based moment geometry, it is clear that the frustration is imposed by the crystal structure.[12] These materials are referred to as geometrically frustrated magnets. In a crystal, geometrically frustrated magnets have a large thermodynamic ground state degeneracy. Lifting this degeneracy has the potential to unlock emergent phenomena and is currently an area of active research.
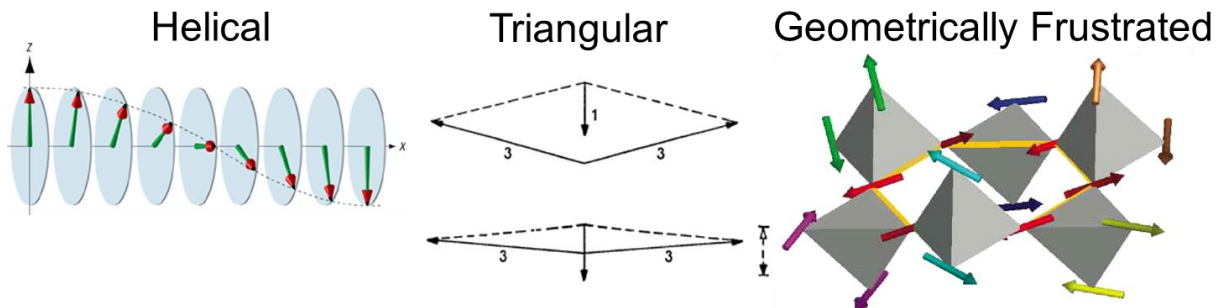
Figure 1.11. Examples of unusual spin configurations that arise from varying degrees of magnetic frustration.[13-15]

To qualify this statement, it is worthwhile mentioning that there are known methods for relieving some of the frustration including chemical tuning of the interstitial sites, further nearest neighbor exchange interactions, and lattice distortions. Often these mechanisms coexist

leading to unusual spin configurations including helical, triangular, and monopole-like arrangements in spin ice as shown in Figure 1.11. The families of spinel ACr_2O_4, chromites, and AV_2O_4 vandates are well known for exhibiting varying degrees of frustrated magnetism.[16]

§1.8 Superexchange
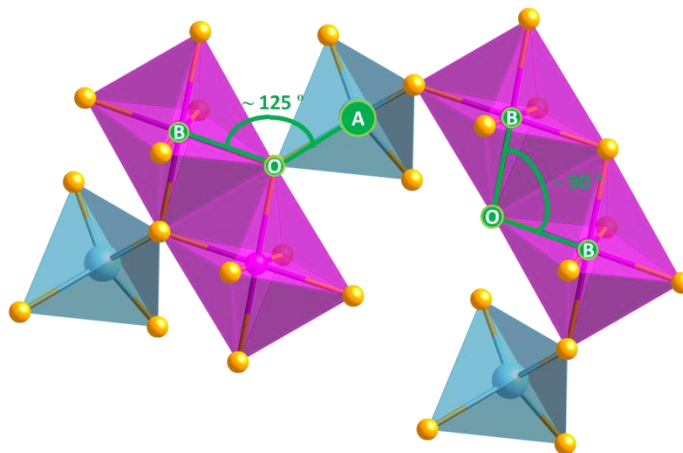
Figure 1.12. Cation bond angles contributing to exchange interactions in cubic spinel oxides. The strongest interaction is due to superexchange from the ~125 ° A-O-B bond angle. The ~90 ° B-O-B bond angle is a secondary superexchange source.

In a spinel oxide crystal, magnetic cations are second nearest neighbors because first nearest neighbors are oxygen anions. The increased proximity between magnetic cations minimizes their orbital overlap effectively weakening their direct exchange. Instead, ferrimagnetism arises from superexchange, an indirect exchange mechanism mediated by the oxygen anion and is a direct consequence of the covalent bonding term.

Superexchange can be explained from the perspective of the oxygen anion.[17] The O^{2-} ion has a filled $2p$ valence shell ($2s^2 2p^6$). However, the presence of neighboring transition metal cations will perturb this closed shell configuration such that a $2p$ electron finds itself belonging to the neighboring transition metal cations for a short period. Perturbations of this nature find that the lowest energy state for oxygen is a superposition of the O^{2-} ground state and excited O^- and neutral O states. Electron transfer occurs via hopping and preserves spin orientation. An electron may only hop into the neighboring orbital if its spin orientation is allowed by the Pauli exclusion principle and favored by Hunds rule. The other $2p$ electron of opposite spin may now interact with the other neighboring transition metal cation assuming the interaction is in accordance with the Pauli exclusion principle and Hunds rule.

Superexchange is strongest for bond angles of 180°, and weakens as the angle becomes smaller.[2] For a spinel, the largest superexchange term originates from the approximately 125 ° angle formed by the A-O-B ions shown in Figure 1.12. There are also contributions from the 90 ° bond angle formed by the B-O-B ions. There are no A-O-A bonds and thus no expected

superexchange. It is also noteworthy that the smaller ionic radius of oxygen leads to the prediction of direct exchange in ionic solids for particular combinations of electronic structure with a 90 ° bond angle.[18]

§1.9 Magnetic Anisotropy

The final magnetism topic I will be discussing is that of magnetic anisotropy. Magnetic anisotropy is important because the direction along which the magnetic moment is measured can give rise to different magnetic behavior. In particular, the magnitude and type of magnetic anisotropy affects the magnetization process and observed magnetic moment. These properties are useful for evaluating the suitability of a material for a desired application.

There are four kinds of magnetic anisotropy: crystal structure, shape, stress, and that induced by magnetic annealing, plastic deformation, or irradiation.[3] I will emphasize magnetocrystalline and shape anisotropy as they are relevant to this dissertation.

Magnetocrystalline anisotropy due to crystal structure is the only intrinsic form of anisotropy. Magnetocrystalline anisotropy is the tendency of the magnetization to align itself along a preferred crystallographic direction. The terms "easy direction" or "hard direction" refer to the crystallographic direction along which it is "easiest" or "hardest" to magnetize an unmagnetized sample to saturation. Field-dependent magnetization measurements of body-centered cubic (BCC) Fe along three high symmetry directions, [001], [110], and [111], find that each direction yields a different curve. From these curves, it can be identified that <100> is the easy direction, <111> is the hard direction, and <110> is an intermediate direction. Along the [100] direction, magnetic saturation is achieved at a much smaller field than the harder [110] and [111] directions.[9] After reaching saturation, the easy direction retains a much greater portion of its magnetization when the applied field, H, is removed. The magnetization value at zero field after saturation has been achieved is the remnant magnetization, M_r. For the intermediate and hard directions, the sloped region of the magnetization curve between zero field and saturation provides insight regarding the process of rotating the magnetization away from the easy direction to a magnetically harder direction.

Furthermore, when the magnetization points along a hard direction as opposed to an easy direction, the crystal exists in a higher energy state. This energy density is represented by the area under the magnetization curve in which $E = \int_0^{M_s} H(M)dM$. The magnetocrystalline anisotropy energy density is the difference in area between two magnetization curves measured along different directions. Finally, there is no simple relation that correlates the easy and hard directions with the arrangement of atoms in a crystal. As a result, while <001> is the easy direction for BCC iron, it cannot simply be inferred that the <001> direction is the easy direction for all magnetic materials with a BCC crystal structure.
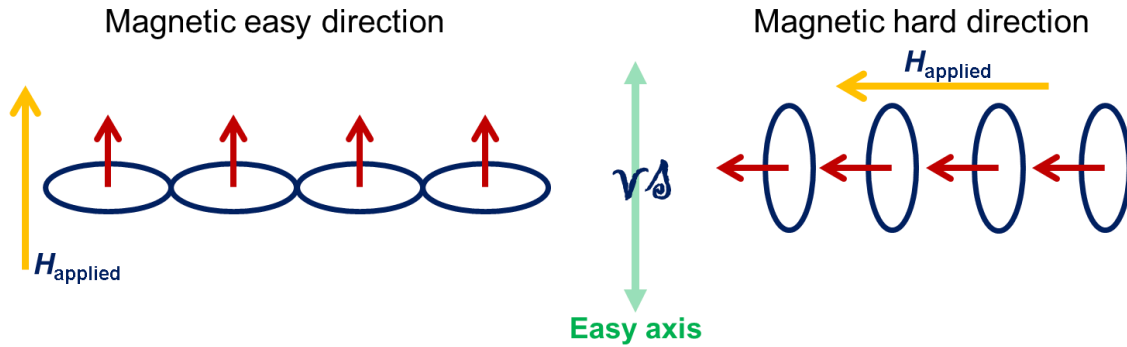
Figure 1.13. Spin and orbital alignment when a magnetic field is applied along easy and hard directions. When the field is applied along the magnetic easy axis, spins are aligned with the field and the orbitals are arranged in a favorable configuration. When a field is applied along a magnetic hard direction, the orbitals will exist in an unfavorable configuration as proposed in the magnetic hard direction. Orbital-lattice coupling makes it difficult to rotate them with the applied field. From Spaldin.[1]

The origin of magnetocrystalline anisotropy is spin-orbit coupling. Figure 1.13 is an illustration from Spaldin which depicts the effects of an applied field on the coupling between the electron spins and orbitals relative to the easy axis of a material. When the applied field is along the easy axis, the electron spins (red arrows) align themselves to point along the direction of the applied field. The electron orbitals (blue ovals) exist in a favorable configuration with overlap representative of bonding. However, when the magnetic field is applied along a hard direction, it reorients the spins to align them with the field by rotating them away from the easy direction. This requires a large field and significant energy to rotate a spin away from a magnetically easy direction. The inherent spin-orbit coupling tries to reorient the orbitals as well. However this results in the orbitals no longer having favorable overlap. Furthermore, because the orbital angular momentum is strongly coupled to the crystal lattice, it resists rotation making it difficult for the orbitals to reorient themselves. Therefore, to saturate a material along a non-easy direction requires a larger field to overcome the spin-orbit coupling in order for the moments to rotate away from the easy axis leading to its higher energy state.
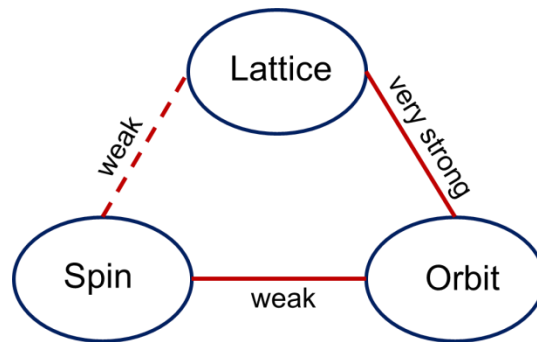
Figure 1.14. Relative coupling strengths between spin, orbit, and lattice. From Cullity.[3]

The relative strengths between the spin-orbit-lattice coupling interactions are summarized in Figure 1.14. Spin-orbit coupling is relatively weak as it can be overcome by only a few 100 Oe. Instead, the orbit-lattice coupling is very strong as the orientations of the orbits are fixed strongly to the lattice and cannot be overcome with the application of a large magnetic field. Because a crystal lattice is made up of atomic nuclei arranged in space, each with a cloud of orbital electrons, we can reason that like spin-orbit coupling, spin-lattice coupling is also weak. Finally, while spin-spin coupling is very strong, its quantum mechanical origin finds that it does not contribute to magnetocrystalline anisotropy as there is no dependence on the spin axis relative to the crystal lattice.

Finally, shape is an important source of anisotropy for thin films.[9] Based on the shape and size of a magnetized sample, a demagnetizing field forms from uncompensated surface poles. A portion of this demagnetizing field passes through the sample opposing the magnetization from which it originated. To correct for this effect, a correction factor of $4\pi M_s$ [CGS] is applied to measurements orthogonal to the film surface.

§1.10 Organization of Dissertation

The theme of this dissertation is to attain new functionality at reduced dimensions and at surfaces and interfaces in spinel-structure oxides. Heteroepitaxy has emerged as a powerful tool for tuning the functionality in correlated oxides. A new area of exploration is non-collinear spin systems as the exchange interactions between magnetic moments make for a plethora of undiscovered phenomena. Accessing new ground states and tailoring new and modified functional properties are possible using small perturbations that disrupt the delicate balance between these interactions. The first part of this dissertation describes the first synthesis of thin films of the magnetically frustrated ferrimagnet, $CuCr_2O_4$, and the subsequent discovery of enhanced magnetization. This is accomplished by lifting the magnetic frustration through the tuning of exchange interactions with heteroepitaxy as a fundamentally new approach for controlling spin order in oxide thin films. The second part of this dissertation incorporates $CuCr_2O_4$ (CCO) as a barrier layer in $La_{0.7}Sr_{0.3}MnO_3$-Fe_3O_4-based magnetic tunnel junctions to investigate its potential as a barrier layer for achieving high junction magnetoresistance at temperatures exceeding that of other spinel barrier materials with lower T_Cs such as $CoCr_2O_4$, $NiMn_2O_4$, and Mg_2TiO_4. It is remarkable to discover that even with interfacial complexities at the two barrier-electrode interfaces, resistive switching is possible. Probes of the isostructural $CuCr_2O_4$/Fe_3O_4 interface also reveal a proximity-induced magnetism in $CuCr_2O_4$ by Fe_3O_4 which is also believed to be the result of the canted moment ordering in CCO. These studies indicate the ability to functionalize the physical properties of non-collinear chromite thin films and serve as the first step towards exploiting new states in canted and strongly frustrated systems leading to further advances in the burgeoning field of correlated oxides. By exploring interaction effects in these frustrated magnets, new avenues for tailoring magnetic order are created and provide insight to stabilizing new magnetic ground states inaccessible in the bulk.

Chapter Two provides an overview of the major experimental techniques used to synthesize and characterize the structure, magnetic properties, and transport properties of the epitaxial complex oxide thin films and multilayers presented in this dissertation.

Chapter Three highlights the use of heteroepitaxial lattice distortions as a method to tune spin functionality and potentially lift ground state degeneracies more broadly in frustrated magnets. It discusses the first synthesis of thin films of the frustrated canted-moment ferrimagnet, $CuCr_2O_4$, and demonstrates the use of heteroepitaxial lattice distortions for modifying the strength of exchange interactions which results in greater collinear spin ordering and enhanced magnetization compared to the bulk. The data presented illustrates the sensitivity of the strong competing exchange interactions suggesting that strain is a promising instrument for perturbing the delicate balance of the exchange interactions in frustrated materials.

Chapter Four discusses the fabrication and properties of oxide-based magnetic junctions. This chapter discusses $CuCr_2O_4$ as it is incorporated as a magnetic tunnel barrier in a $La_{0.7}Sr_{0.3}MnO_3$- Fe_3O_4-based magnetic junction structure. Element-specific magnetic techniques establish independent switching of the magnetic electrodes and uncover evidence of proximity-induced magnetism. Magnetotransport studies show that junctions display resistive switching with junction magnetoresistance (JMR) up to -6%. Furthermore, a JMR minimum at zero bias was observed and attributed to the band structure of the Fe_3O_4 electrode and the spin filtering phenomenon in the magnetic tunnel barrier.

Appendix A presents a detailed description of the fabrication method used to create crossbar arrays of micron-sized magnetic tunnel junction.

Thin film heteroepitaxy has enabled access to new material ground states beyond those thermodynamically found in their bulk counterparts. In complex oxides, stabilizing these new and modified phases requires the selection of an appropriate growth template and the utilization of a growth method that allows for controlled stoichiometric transfer of the target source material to the growth template. This chapter discusses the major experimental techniques used to synthesize and characterize the structure, magnetic properties, and transport properties of the epitaxial complex oxide thin films and multilayers presented in this dissertation.

§2.1 Thin Film Growth Using Pulsed Laser Deposition

Widely popularized for the synthesis of high temperature superconductor thin films like $YBa_2Cu_3O_{7-\delta}$, pulsed laser deposition (PLD) is now vastly utilized for synthesizing epitaxial oxide films and multilayers. PLD is a non-equilibrium, physical vapor deposition (PVD) growth technique capable of achieving stoichiometric transfer to thin films from a multi-elemental target. In PVD techniques, atoms are removed from a source through a transfer of energy. This can occur via thermal means (*e.g.* current, electron beam) in evaporation or by impact with an ionized gas in sputtering. In PLD, ablation occurs when a laser delivers high energy to a small volume of the target.
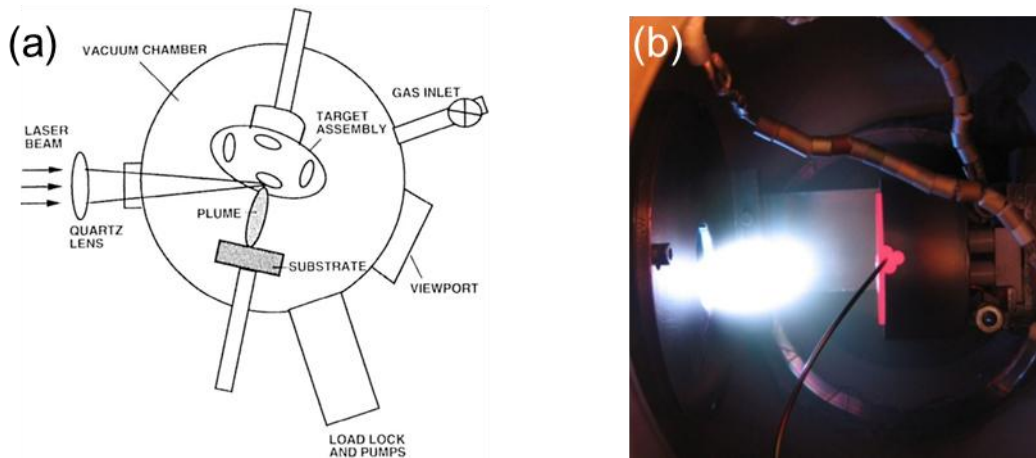
Figure 2.1. (a) Schematic of the PLD setup.[1] (b) A substrate mounted on the ceramic target heater is aligned with the highly directional plasma plume.

The schematic of a PLD setup is shown in Figure 2.1(a). Through a series of optics, an external KrF excimer laser (λ = 248 nm) is directed, attenuated, and focused onto a rotating ceramic target in a high vacuum chamber. Rapid heating occurs as the laser beam strikes a small region of the target known as the heat affected zone and vaporizes the surface species. A plasma, which consists of charged and neutral species, is formed as energy absorption by the vapor increases eventually exceeding that needed for evaporation. Near the target in a region known as the Knudsen layer, collisions between the plasma species expand the vapor plasma

plume to a thickness of a few hundred microns along a pressure gradient from the vacuum resulting in a highly directional plume. Aligned with the plume, a substrate is mounted on a ceramic heater with thermally conductive silver paste at a controlled distance between 2.5 - 3 inches. The plasma contents condense on the substrate to form a film (Figure 2.1(b)). Stoichiometric transfer ensues as PLD is not rate-limited by the equilibrium vapor pressures of the constituent elements.

The ablation process makes PLD well-suited for materials with a high optical absorption coefficient at the wavelength of the laser. This coincides with many ceramics as they exhibit strong absorption and reduced penetration depths in the ultraviolet range (200-400 nm). For these reasons, metals are non-ideal candidates for PLD. Characterized by their high reflectivity and thermal conductivity, metals absorb less and allow the transferred laser energy to penetrate deeper into the target making ablation difficult.

PLD offers significant advantages over other PVD techniques. Its widespread use is due to its primary advantage of achieving stoichiometric transfer of material from a multi-elemental target. By tuning the growth parameters, PLD can also be used to control film growth with near atomic precision. It is fast and depositions consume a minimum volume of often expensive source material. With regard to setup, a target carousel within the growth chamber makes it easy to access multiple targets without breaking vacuum preserving the cleanliness at multilayer interfaces. Finally, the external laser allows for the use of a background gas in the deposition chamber.

The disadvantages of PLD have limited its commercial viability. The highly directional nature of the plume limits the area over which uniformly thick films can be grown. Secondly, the ablation process often causes the ejection of macroparticles due to the rapid expansion of gas trapped beneath the target surface, a rough target surface morphology, and/or the superheating of the subsurface before surface atoms vaporize.[2] The presence of these macroparticles is especially detrimental in multilayer samples subject to lithographic processing. For this reason, the use of highly dense targets is desirable for reducing the number of particulates.

As discussed at the start of this chapter, the allure of PLD is that, combined with the right substrate, it enables the control of structural, electrical, and magnetic properties. Proper stoichiometric transfer and the tailoring of film properties are engineered by optimizing growth parameters that include the laser pulse rate, laser fluence, target-to-substrate distance, substrate temperature, post-deposition treatments, and selection and pressure of background gas.[3,4] These degrees of freedom begin with the often polycrystalline nature of the ceramic target. Assuming low volatility, the only requirement of the target is that the cation stoichiometry needs to be identical or very similar to that of the film.

For target ablation, laser pulses are short in duration, deliver a high energy density, and are highly absorbed by the target. This is essential for crossing the threshold from evaporation to ablation facilitating stoichiometric transfer. The laser pulse frequencies used for thin film and multilayer synthesis ranged between $1 - 10$ Hz. Each pulse typically deposits a submonolayer of material ranging between $0.001 - 1$ Å per pulse.[3] The actual rate depends on the target material, energy density, and substrate-to-heater distance. Typically a higher energy density and/or shorter substrate-to-heater distance leads to a higher deposition rate. With the use of a

low laser pulse repetition rate, a deposition process with submonolayer control emerges. A slower pulse rate allows for greater surface diffusion by newly condensed species as the longer time interval between laser pulses provides an opportunity for these species to find an energetically favorable position. Higher pulse rates minimize the duration for surface diffusion to occur before being covered by new material delivered by subsequent pulses. In general, a slower repetition rate often results in better crystallinity. With greater lattice mismatch between the film and substrate, a slower repetition rate also results in rougher film surfaces. In comparison, holding all other variables constant, higher repetition rates often lead to smoother films and an increased number of defects. Thus, these variables can be used to tailor film smoothness and the nature or quantity of defects.

Substrate temperature and post-deposition treatments are also useful tools for improving film surface smoothness and crystallinity. The use of lower substrate heater temperatures often results in smoother films. Higher temperatures enable surface diffusion often improving crystallinity. However, in multilayers excessive temperatures can lead to interdiffusion at interfaces. Interdiffusion is a well-known problem for open crystal structures like spinels in which cations can diffuse through the large number of interstitial site vacancies. Post-deposition treatments such as annealing are also particularly useful for removing defects by continuously heating a sample post-deposition to facilitate dislocation motion. For materials that are not well lattice matched to a substrate, annealing is typically avoided and an equilibrium cool to room temperature is best to prevent surface roughening.

Finally, the use of a background gas is a key differentiation between PLD and other PVD techniques. Thermal evaporation by heating a wire or pellet boat containing source material or the use of an electron beam requires high vacuum preventing the use of a background gas. The background gas has important implications. First, it can be used to facilitate surface reactions and stoichiometric transfer of highly volatile species. Secondly, the presence of a background gas reduces the kinetic energy of the ablated species. In vacuum, the kinetic energy of the plasma species is on the order of 100 eV. With a background gas present, the plume expansion slows and the plasma species collide with the gas molecules. Through deflections and inelastic collisions, the kinetic energy of the species impinging on the substrate-film surface is reduced to < 1 eV. This reduction in kinetic energy of the impinging species prevents backsputtering of substrate-film surface atoms and prevents other potential damage caused by high energy species. For oxides, oxygen background gas behaves as an oxidizing species facilitating growth. The extent of its presence or absence can stabilize multivalent oxidation states in cations. Oxygen deficiency most commonly results in the formation of point defects referred to as oxygen vacancies. Cooling to ambient temperatures in an oxygen-rich environment can affect cation oxidation states and circumvent oxygen vacancies. Annealing in oxygen may also be desirable for materials with oxygen affinities like the doped manganite $La_{0.7}Sr_{0.3}MnO_3$.

§2.2 Structural and Chemical Characterization Techniques

§2.2.1 Atomic Force Microscopy

Atomic force microscopy (AFM) is a scanning probe imaging technique used for surface analysis. A probe tip rasters across an area of the film surface extracting information that includes surface morphology images, surface roughness, and step feature heights. It offers sub-nanometer-scale vertical resolution and lateral resolution between 1-5 nm. It is also easy to use and relatively fast. Incorporating AFM as the first characterization step after film growth allows for quick evaluation of the effects of deposition conditions on film morphology.

All AFM data presented in this dissertation were obtained in tapping mode. Tapping mode is commonly used as it reduces tip breakage and minimizes damage or other modifications to the sample surface. The sample surface is scanned using a cantilever with a tip (radius ≈ 5–15 nm) at its end. The cantilever oscillates near its resonance frequency. When the tip is brought into close proximity with the surface, the interaction between attractive and repulsive forces changes the deflection of the cantilever according to Hooke's Law, $F = -kx$. The deflection of the cantilever is measured using a laser spot reflected from the top surface of the cantilever into an array of photodiodes. The scanner hardware then adjusts the probe's vertical position with a piezoelectric stack to maintain constant deflection of the cantilever. The changes in the z position of the stack are then recorded as topographic signal.

§2.2.2 X-ray Diffraction

X-ray diffraction (XRD) provides quantitative information about the crystal structure and crystalline quality of thin film and multilayer samples. Measurements are performed by rotating a sample about four axes or circles which are illustrated in Figure 2.2. For a majority of experiments in this dissertation, table top diffractometers with a monochromatic Cu K_α X-ray source ($\lambda = 1.54$ Å) irradiated samples to obtain the out-of-plane lattice parameters of the film and substrate. These experiments utilized coupled 2θ scans. In coupled scans, the condition $\omega = \theta$ must hold over the range 2θ values measured. In practice, substrate miscut and sample mounting often cause small deviations from this condition decreasing the diffracted X-ray beam intensity. To resolve these experimental errors, a small offset, δ, is calculated to re-establish the optimal diffraction condition such that $2\theta = 2(\omega+\delta)$. The optimal diffraction condition is extracted from a geometric construct known as Bragg's Law

$$n\lambda = 2dsin\theta, \tag{2.1}$$

where n is the order of diffraction, λ is the X-ray wavelength, d is the spacing between lattice planes, and θ refers to the Bragg angle. When Bragg's Law is satisfied, diffraction peaks emerge. The angular 2θ peak position is recorded allowing for the calculation of the d spacing and consequent lattice parameters. This was sufficient for the experiments discussed in chapter 4. However, the experiments presented in chapter 3 required knowledge of the film unit cell and necessitated the need to acquire the in-plane lattice parameters. We required the use of the ψ and χ circles in order to access a series of reflections (*e.g.* 400, 040, and 004) many of which

were of low intensity. By accessing different sets of (*hkl*) planes in reciprocal space, each real space lattice parameter (*a, b, c*) could be determined as follows. The position of the diffraction peak was defined by its Q-value obtained during the measurement, where

$$Q = \frac{2\pi}{d}. \tag{2.2}$$

From this relation, the d-spacing of the planes could be calculated. Knowing *d* and the values of (*hkl*) that correspond to Q, the lattice parameters *a*, *b*, and *c* could be calculated from

$$\frac{1}{d^2} = \frac{h^2}{a^2} + \frac{k^2}{b^2} + \frac{l^2}{c^2}. \tag{2.3}$$

Reflections were selected based on intensity and *h*, *k*, and *l* values that would allow for calculating the *a*, *b*, and *c* lattice parameters. More than one set of planes were selected with a non-zero h, k, or l value for improved averaging statistics. These experiments required the high flux and four-circle alignment capabilities of BL 7-2 at the Stanford Synchrotron Radiation Lightsource (SSRL) at the SLAC National Accelerator Laboratory.
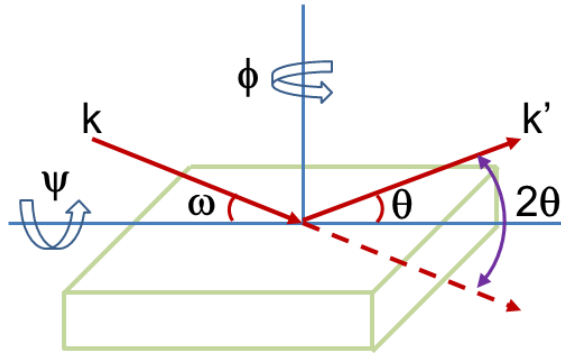
Figure 2.2. Schematic of the four-circles in X-ray diffraction.

§2.2.3 Rutherford Backscattering Spectroscopy

Rutherford Backscattering spectroscopy (RBS) provides quantitative elemental analysis allowing for the verification of layer thickness and composition and detection of interdiffusion in thin films and multilayers. The basis for RBS is the billiard ball collision principle. Samples are bombarded with a ~2.04-3.04 MeV He^{2+} projectile ion beam. As the He^{2+} ions pass through the sample, a few will directly "collide" with the atomic nuclei of the material causing the projectile ions to elastically backscatter. An energy sensitive detector positioned at the backscattering angle measures the energy and quantity of the collected particles. Experiments are performed using the Cornell geometry in which the incident beam, exit beam, and sample rotation axis are in the same plane optimizing the mass and depth resolution up to approximately 1 μm below the sample surface.

The three physical factors governing the RBS technique are the kinematic factor, energy loss, and scattering cross section. They are important for understanding the resultant spectra as they determine the energy of the backscattered particles, the changing energy of the projectile

ions with depth, and the rate at which the projectile ions are scattered. First, the kinematic factor is used to calculate the energy of the backscattered particles, E_m. The kinematic factor is the ratio of the projectile ions energy before and after collision given by the relation

$$K_M = \frac{E_m}{E} = (\frac{\sqrt{M^2 - m^2 \sin^2 \theta} + m \cos \theta}{M + m})^2, \quad (2.4)$$

where M is the target atom mass and m is the He^{2+} ion mass. Energy loss of the projectile ions is the result of their interactions while passing through the sample. Small energy losses frequently occur due to their interactions with the electron clouds of the target atoms and glancing collisions with the nuclei of the target atoms. Backscattering collisions are infrequent and characterized by large energy losses. However, they are the premise for RBS and their rate depends on the differential cross section of a material, $\frac{d\sigma}{d\Omega} \propto \frac{(zZ)^2}{E^2}$, where z = atomic number of the projectile and Z = atomic number of the target.

In RBS data, peak width is correlated to film thickness. A wider peak is associated with a thicker film. For single films, the higher energy peak edge corresponds to the film/vacuum interface, and the low energy edge corresponds to the film/substrate interface. At the higher energy edge, projectile atoms have traveled a shorter distance into the sample incurring smaller energy losses. It follows that for collisions occurring deeper in the film, the pre-collision projectile energy is lower than those occurring near the surface.

Simulations of the data are performed with SIMNRA software.[5] The input parameters begin with the global parameters entered into "Setup:Experiment" including the incident ion beam source and energy, scattering geometry, and the calibration of the channels to energy conversion. Channels come from the multi-channel analyzer in which the signal height is converted into "channels" corresponding to an energy range. Collected events in each channel have a specific energy. For the measurements presented in this dissertation, the calibration is ~2.935 keV channel[-1]. Next, the properties of each sample layer are defined and entered into the "Target" pop-up window with layer 1 representing the topmost layer. These properties include a guess of the film thickness and the concentration of each element assuming uniform composition and thickness. This is followed by selecting the appropriate cross-section data for each element. The default is the Rutherford cross-sections. A simulation of the spectrum is then calculated, and plotted as a function of counts versus channel. Data peaks are identified using the "element spectra" menu option.

A systematic approach to perform simulations of thin film heterostructures begins with a background fit to the substrate. This fit is easily performed with the "Calculate:Fit:Particles*sr" function. It requires selecting the layer representing the substrate and the range of channels over which the fit should be performed. Particles* sr is the number of incident particles multiplied by the solid angle of the detector. Next, if neighboring peaks originate from the same layer, then the composition and thickness of that layer can be fit using the "Calculate:Fit:Layer composition and thickness" function. If neighboring peaks are not from the same layer, then a manual fit is required. Once a satisfactory spectrum is acquired, the real film thickness is calculated by dividing the RBS thickness by the layer density. The RBS thickness is actually a two-dimensional concentration of the atoms in the layer given in units of atoms cm^{-2}. The layer density is converted from the density, D_x (g mol^{-1}), obtained from a powder diffraction file as follows

$$\text{density (atoms cm}^{-3}) = \frac{D_x \times \text{number of atoms per unit cell} \times N_A}{\text{molar weight}}. \tag{2.5}$$

The utility of RBS is limited for light Z elements due to their smaller scattering cross sections. To overcome this, alternative experimental setups can be used. For heavy Z elements, it is difficult to distinguish between elements with neighboring Z values (*e.g.* Ni and Fe) in RBS spectra as peaks often overlap. However, in combination with a supplementary technique like particle induced X-ray emission (PIXE) a qualitative composition ratio can be established from the integrated intensities at elemental K_α energy peaks in relation to the elemental scattering cross sections given by Equation 2.6. PIXE measures the characteristic energies of X-rays emitted when an electron lowers its energy to fill a *K* shell hole. RBS and PIXE measurements were performed at the Ion Beam Analysis Facility at Lawrence Berkeley National Laboratory (LBNL).

$$\text{Composition ratio: } \frac{[A]}{[B]} \sim \frac{\text{\# counts at } K_\alpha(A)}{\text{\# counts at } K_\alpha(B)} \times \frac{\sigma_B}{\sigma_A}, \tag{2.6}$$

where σ is the scattering cross section.

§2.2.4 X-ray Absorption Spectroscopy

X-ray absorption (XA) spectroscopy is a synchrotron-based technique used to obtain valence and site symmetry information about the chemical constituents in a sample. By tuning the X-ray energy to a characteristic element absorption edge, core electrons are excited into empty states above the Fermi energy effectively probing the unoccupied density of states. Allowed transitions are governed by the dipole selection rules. The energy range of soft X-rays is well-suited for $2p$ to $3d$ transitions or *L* edge absorption studies of $3d$ transition metals. Measurements were performed using total electron yield (TEY) detection as depicted by the schematic in Figure 2.3. In TEY, the core holes created by XA process are filled by emitting Auger electrons. As these Auger electrons try to escape the sample, it creates a cascade effect of low energy, inelastic scattering processes thereby generating secondary electrons. The resulting photocurrent is measured with a picoammeter that measures the electrons flowing back into the sample from ground. Auger processes are limited to the surface region of a sample making TEY a surface-sensitive technique with a probing depth of 2-5 nm.

In oxides, $3d$ transition metal spectra typically exhibit two broad peaks which arise from spin-orbit interactions that split the $2p$ core states into $2p_{3/2}$ and $2p_{1/2}$ states. This gives rise to the L_3 and L_2 edges, respectively, as they are based on the initial state of the excited electron. These spectra exhibit fine structure as the empty states are more localized than that of a metal and are affected by crystal field and multiplet effects. Multiplet effects arise from the spin and orbital momentum coupling of different $3d$ valence holes (or electrons) in the electronic ground state, and from coupled states formed after XA between the $3d$ valence holes and the $2p$ core hole.[6] An understanding of the fine structure can be gathered from simulations using multiplet-based software. However, it is often sufficient to perform a qualitative fingerprint analysis against published spectra to identify the valence and site symmetry of an element. XA experiments were performed on beamlines 4.0.2 and 6.3.1 at the Advanced Light Source (ALS) at LBNL.
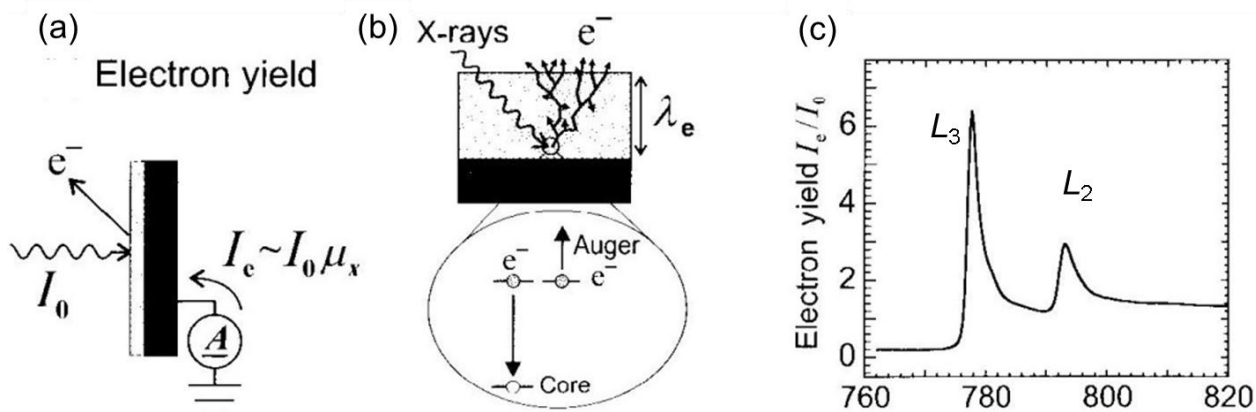
Figure 2.3. (a) XA measurements by the total electron yield detection method. (b) Core holes created by the XA process are filled by emitting Auger electrons. (c) The Co spectra is an example of a $3d$ transition metal spectra that exhibits two broad peaks that correspond to the L_3 and L_2 edges. From Stohr.[6]

§2.2.5 Resonant X-ray Scattering

Resonant X-ray scattering (RXS) is a synchrotron-based technique used for determining the elemental site occupancies of crystallographic planes. This combines the structural technique of XRD with the chemical technique of XA. For spinels, advanced structure factor calculations are used to identify crystallographic planes which diffract solely from either the tetrahedral or octahedral sites. After aligning the diffractometer to a reflection, the beamline energy is tuned to the K edge energy for XA. If an element is present in a given set of planes, absorption will occur decreasing the diffracted intensity. Alternatively, if an element is absent there will be no absorption and the diffracted intensity remains unaffected. If absorption occurs, the decreased intensity can be compared to reference simulations or simulated using a nonlinear least squares fit to extract a site occupancy ratio. This work was performed on beamlines 2-1 and 7-2 at SSRL. Nelson-Cheeseman presents an extensive description of this technique and simulation methodology.[7]

§2.3 Magnetic Characterization

§2.3.1 SQUID Magnetometry

Superconducting quantum interference device (SQUID) magnetometry is a bulk magnetic characterization technique used to identify the magnetic properties of a material including saturation magnetization, remnant magnetization, and critical transition temperatures. The magnetometer uses a SQUID that is composed of two Josephson junctions in parallel; SQUIDs can measure magnetic flux down to a flux quantum. SQUID measurements were performed on a Quantum Design MPMS 5XL magnetometer with the ability to probe magnetic moments as small as 10^{-6} emu with magnetic fields up to 5 Tesla and at temperatures between 5

– 380 K. To extract the magnetic moment of single films, the high field diamagnetic background is subtracted from the raw data in order to remove the diamagnetic contribution from the substrate. The magnetic moment of the film is then normalized by its volume to determine its magnetization. The film volume is established from lateral dimensions obtained with calipers and film thicknesses calculated from RBS in conjunction with growth calibration standards.

§2.3.2 X-ray Magnetic Circular Dichroism

X-ray magnetic circular dichroism (XMCD) is an element-specific magnetic characterization technique which elucidates the size and direction of the magnetic moments by probing the spin-dependent density of states. It utilizes the polarization dependence of absorption to create a spin-dependent absorption process. This is accomplished using X-rays of opposite angular momenta, *i.e.* left- and right-circularly polarized X-rays, which are transferred to the excited photoelectron. XMCD is the difference in intensity of XA spectra when measured at alternating polarizations in the presence of a magnetic field. Equivalently, an XMCD measurement can be performed by selecting one polarization and alternating the direction of the magnetic field. With a sufficient pre- and post-edge, XMCD can be used to calculate the spin and orbital moment. The temperature-dependence of XMCD provides insight regarding the changing magnitude of the magnetic moment. For ferrimagnets, it can also be used to determine the magnetic moment alignment of different magnetic species with respect to the applied field direction. As an extension, field dependent magnetization loops can be obtained providing valuable information regarding phenomena like anisotropy, element-specific ferromagnetism, exchange biasing, and interfacial coupling. XMCD experiments were performed on beamlines 4.0.2 and 6.3.1 at the ALS.

§2.3.3 Neutron Reflectivity
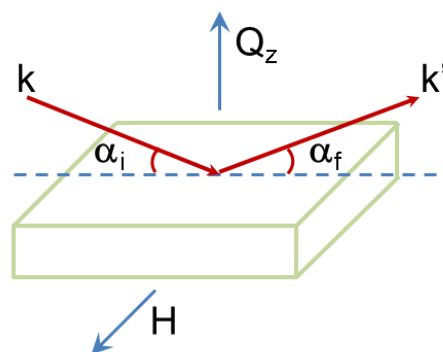
Figure 2.4. Specular reflectivity geometry used for neutron reflectivity measurements.

Polarized neutron reflectivity is a quantitative technique used for magnetic depth profiling of thin films and multilayers. A reflectometry technique, the intensity of the reflected

beam is measured as it is sensitive to changes in the refractive index, n, across interfaces. A neutron source provides magnetic sensitivity due to the intrinsic spin and small magnetic moment of the neutron. Together they affect the measured scattering length density normal to the surface as a function of depth. Scattering length density (SLD) is

$$\rho(z) = \frac{(1-n^2)Q_z{}^2}{\pi} = \rho_{\text{nuclear}}(z) + \rho_{\text{magnet}}(z), \tag{2.7}$$

where Q_z is the scattering vector

$$Q_z = \frac{4\,\pi\,\sin\theta}{\lambda}. \tag{2.8}$$

The SLD is the sum of the nuclear SLD

$$\rho_{\text{nuclear}}(z) = \sum_i N_i b_i, \tag{2.9}$$

where N = the number density and b = scattering length; and the magnetic SLD

$$\rho_{\text{magnet}}(z) = 2.853 \times 10^{-9} M, \tag{2.10}$$

where M is the magnetization. For values of Q greater than the critical angle for total internal reflection, fringes appear in the reflectivity data. The amplitude of these fringes represents nuclear contrast across an interface. The periodicity of these fringes is inversely related to the layer thicknesses to within 3% uncertainty. The reflectivity data is then fit to obtain a real-space profile of $\rho_{\text{nuclear}}(z)$ and $\rho_{\text{magnet}}(z)$. The magnetic SLD can be further converted into magnetization verifying values obtained with other magnetometry techniques.

Neutron reflectivity experiments were performed on the NG-1 reflectometer at the NIST Center for Neutron Research. Measurements were performed at temperatures as low as 5 K using both polarized neutrons with a maximum field of 660 mTesla and unpolarized neutrons with a maximum field of 7 Tesla. These experiments were performed using specular reflectivity in which the incident and exit angles of neutrons impinging upon the sample surface incident are equal, $\alpha_i = \alpha_f$ (Figure 2.4).

§2.4 Electrical Transport

Electrical transport measurements determine the resistance and magnetoresistance of single films and junction heterostructures. Measurements were performed on a Quantum Design Physical Property Measurement System with magnetic fields up to 9 Tesla and over a temperature range of 5 – 380 K.   For single films, the four point method is used with the van der Pauw and 4-inline bar geometries depicted in Figure 2.5 to determine the current-in-plane (CIP) properties.

$$R_A = \frac{V_{12}}{I_{34}}, \quad R_B = \frac{V_{13}}{I_{24}}$$
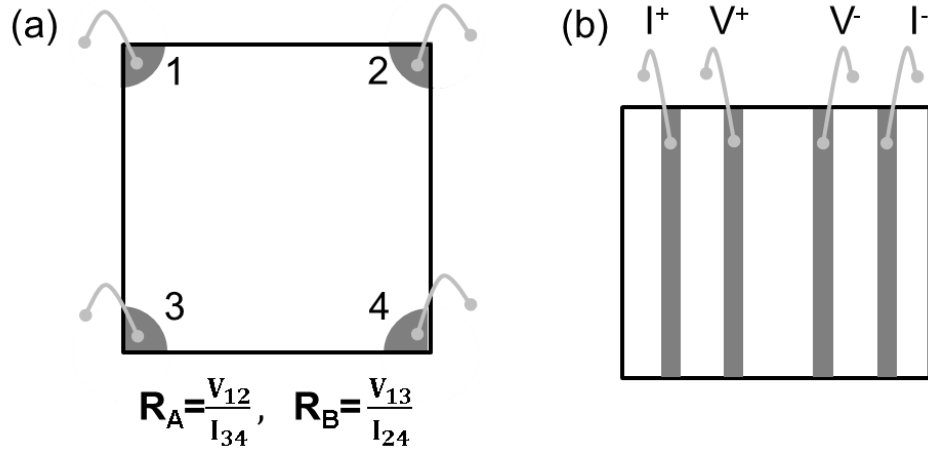
Figure 2.5. Schematics of the (a) van der Pauw and (b) 4-inline bar geometries.

For the van der Pauw geometry, AuPd contacts are sputter deposited on the four corners of the sample using a foil shadow mask. Metal contacts minimize contact resistance at the bond interface between the sample and the leads ensuring ohmic contact. Current is injected along one sample edge (*e.g.* contacts 1-2) while the voltage is measured along the opposing edge (*e.g.* contacts 3-4). This measurement is repeated along the perpendicular edge directions (*e.g.* contacts 1-3 and 2-4). Measuring along the perpendicular edges results in two resistance values denoted as R_A and R_B. Using these resistances, the van der Pauw equation (Equation 2.11) is solved for the sheet resistance, R_s.

$$e^{\frac{-\pi R_A}{R_S}} + e^{\frac{-\pi R_B}{R_S}} = 1 \tag{2.11}$$

The van der Pauw measurement assumes film uniformity and is independent of sample size. Therefore, the film resistivity is the product of R_S and film thickness, t, given by Equation 2.12.

$$\rho = R_s \text{ x } t \tag{2.12}$$

The 4-inline bar geometry is used an alternative to the van der Pauw geometry for exploring the effects of anisotropy on the magnetoresistance of single films. Four parallel AuPd bars are sputter deposited using a shadow mask (Figure 2.5(b)). Current is passed through the outer bars, I^+ and I^-, inducing a voltage between the inner bars, V^+ and V^-. Resistance is calculated using Ohm's Law

$$R = \frac{V}{I} \tag{2.11}$$

and magnetoresistance (MR) is defined as

$$MR = \frac{R(H) - R(H=0)}{R(H=0)} \times 100. \tag{2.12}$$

Using this geometry, the orientation between the direction of current flow and the applied magnetic field is unambiguous.

For junction interfaces, the two-point current-perpendicular-to-plane (CPP) method is used to measure the resistance of heterostructures patterned into arrays of crossbar junction structures. A detailed description of the patterning method can be found in Appendix A. With the use of a source-measure unit, a bias voltage is sourced across a junction and the resultant current is measured. This is the preferred method to simultaneously extract bias dependence characteristics with field- and temperature-dependent measurements. To ensure that the resistance accurately reflects that of the junction, the magnitude of the electrode resistance must be orders of magnitude less than the junction.

Competing exchange interactions can give rise to varying degrees of frustration that manifest itself in non-collinear magnetic moment ordering or canonical geometric frustration in magnets with large ground state degeneracies. Relieving this frustration has the potential to stabilize ground states inaccessible in the bulk. This chapter highlights the use of heteroepitaxial lattice distortions as a method to tune spin functionality and potentially lift ground state degeneracies more broadly in frustrated magnets. It discusses the first synthesis of thin films of the frustrated canted-moment ferrimagnet, CuCr$_2$O$_4$, and demonstrates the use of heteroepitaxial lattice distortions for modifying the strength of exchange interactions which results in greater collinear spin ordering and enhanced magnetization compared to the bulk.[1,2] The data presented illustrates the sensitivity of the strong competing exchange interactions suggesting that strain is a promising instrument for perturbing the delicate balance of the exchange interactions in frustrated materials.

§3.1 Frustration in Spinels

In the spinel crystal, the A-sublattice forms a diamond lattice and the B-sublattice forms a pyrochlore lattice. The pyrochlore lattice, referencing the pyrochlore structure, $A_2B_2O_7$, is formed by the network of edge-shared octahedral cages illustrated in Figure 3.1(a). Peeling away the oxygen anions finds that the cations which comprise the B-sublattice form a network of corner-sharing tetrahedron (Figure 3.1(b)). When the coupling between the magnetic moments on the pyrochlore lattice is antiferromagnetic, strong frustration is expected because of the triangle-based geometry. Viewing the crystal along the <111> direction reveals alternately stacked planes of triangular and kagome lattices. An extension of the two-dimensional case presented in Chapter 1, the geometry of the three-dimensional lattice makes it impossible to satisfy all antiferromagnetic exchange interactions with Ising spins leading to a large macroscopic ground state degeneracy in the presence of structural order.[3]
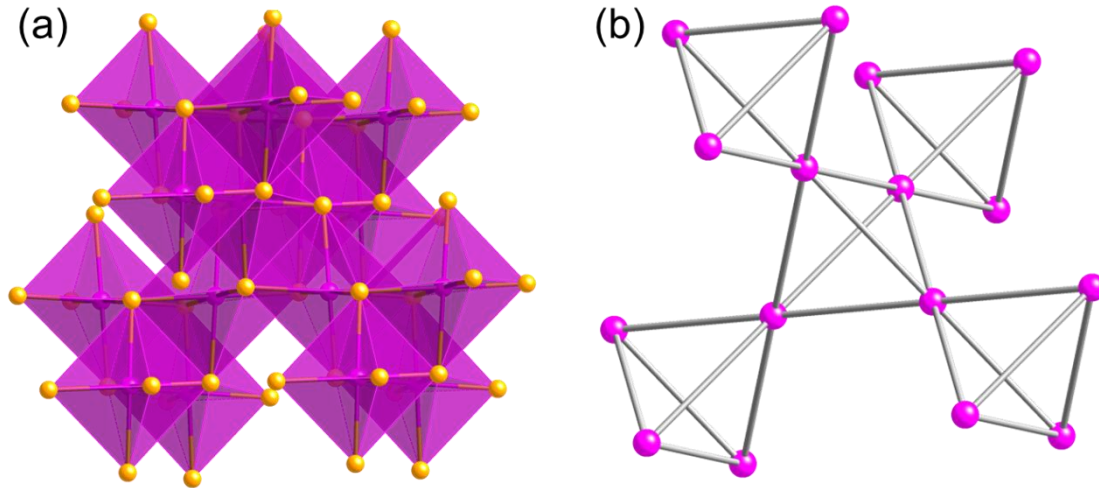
Figure 3.1. (a) The pyrochlore lattice in the spinel crystal is comprised of a network of edge-shared octahedral cages. (b) The octahedrally-coordinated cations form a network of corner-sharing tetrahedra illustrating its three-dimensional triangle-based geometry. (Gray connector lines are used to distinguish the tetrahedron, and do not represent bonds.)

This is especially true for the chromite spinels, ACr_2O_4, which display magnetic ground states that range from highly frustrated systems like canonical geometrically frustrated magnets [3] to those with reduced frustation such as non-collinear spin systems that exhibit helicoidal [4-6] and triangular, canted [7,8] order. Antiferromagnetically-coupled, half-filled t_{2g} Cr^{3+} cations have a strong tendency to occupy the octahedral interstitial sites.[9] When a non-magnetic cation occupies the tetrahedral interstitial sites (e.g. Cd, Zn, Mg), the Cr^{3+} containing pyrochlore lattice with no orbital degrees of freedom, results in some of the strongest geometric frustration known. When a magnetic cation occupies the tetrahedral sites (e.g. Mn, Fe, Co, Ni, Cu), the frustration is reduced by varying degrees giving rise to unusual, non-collinear ordered spin configurations. Theoretical studies have focused on their spin ordering stability,[10] and experimental studies have uncovered spin-lattice coupling,[11] multiferroicity,[12-14] and magnetism-induced anisotropic lattice dynamics.[15] In heterostructures, the chromites have revealed large junction magnetoresistance and spin filtering demonstrating their potential for oxide-based spintronics.[16-18] The ability to modify the physical properties of spinel chromites through the tuning of their spin configurations allows access to new ground states in non-collinear ordered and strongly geometrically frustrated magnetic oxides.

The properties of these frustrated systems are particularly susceptible to small perturbations such as electric and magnetic fields, chemical modification, and strain. With advances in thin film deposition techniques, heteroepitaxy can be used to explore new spin phase space regions in these frustrated magnets. There have been numerous studies for which heteroepitaxial strain has given rise to emergent phenomena or tuned functionality in complex oxides.[19,20] In many of these studies, heteroepitaxial strain induces lattice distortions that, in turn, modify the electronic structure and magnetic ordering.[21] However epitaxial strain may lift the degeneracy of the ground states of frustrated magnets through the modification of exchange interactions, thus providing a different approach for controlling spin order in oxide

32

thin films. A model system for the study of such effects is the tetragonal, canted ferrimagnet, $CuCr_2O_4$ (CCO). $CuCr_2O_4$ exhibits non-collinear moment ordering due to the presence of closely competing exchange interactions between magnetic moments of the tetrahedrally and octahedrally coordinated cations.

In particular, for CCO films grown on isostructural $MgAl_2O_4$ (MAO) substrates, by decreasing the tetragonality of the CCO unit cell yielding greater collinear alignment between the Cr^{3+} moments, we heal the frustration of the magnetic moments in CCO thin films and significantly enhance the magnetization compared to that of bulk. XRD indicates that epitaxial strain stabilizes a more cubic unit cell compared to the bulk. Bulk magnetometry measurements performed with a SQUID magnetometer demonstrate enhanced magnetization. Neutron reflectivity (NR) shows magnetic uniformity in the films, thus eliminating surface or interface effects as the source of enhancement. Element-specific XMCD studies suggest that the increased net moment of Cr^{3+} is responsible for the enhanced magnetization.
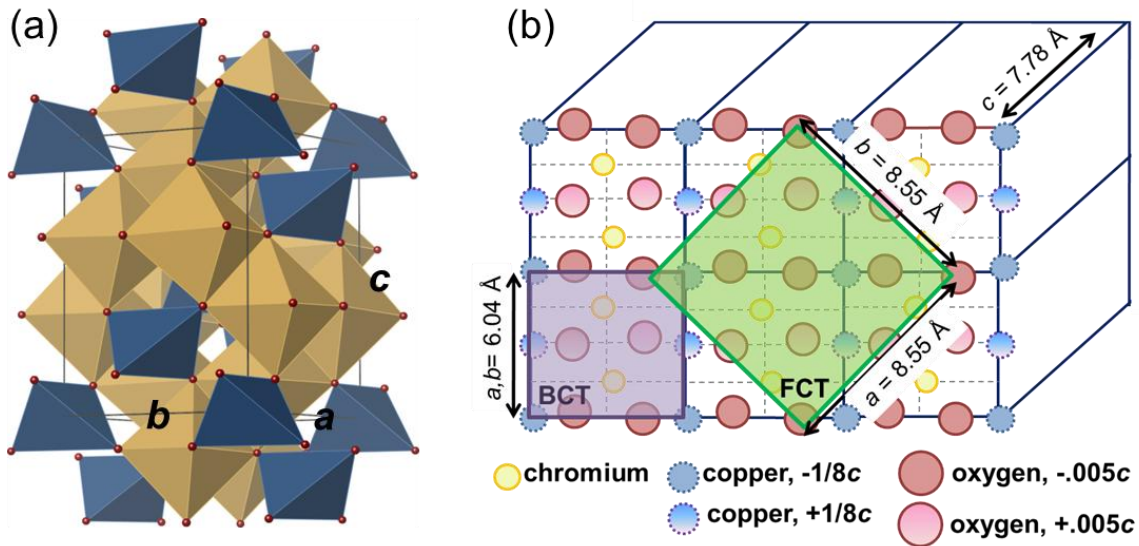
Figure 3.2. (a) The body-centered tetragonal $CuCr_2O_4$ spinel structure showing the edge-sharing Cr^{3+} octahedra (yellow) formed by oxygen anions (red, size reduced for clarity). The Cr^{3+} octahedra are corner-shared with the Cu^{2+} tetrahedra (blue). (b) The (004) projection of the CCO unit cell highlights the BCT (purple square) and FCT (green square) unit cells.

Bulk $CuCr_2O_4$ is an insulating ferrimagnetic spinel oxide with a tetragonal unit cell (a_{BCT} = 6.04 Å, a_{FCT} = 8.55 Å, c = 7.78 Å) and c/a_{BCT} ratio of 1.29 or c/a_{FCT} ratio = 0.91. The body-centered tetragonal (BCT) unit cell (Figure 3.2(a)) is formed by Cu^{2+} (1 μ_B) cations which occupy the tetrahedral sites because the Cr^{3+} (3 μ_B) cations have a strong preference for the octahedral sites.[7,22] The projection along the [004] direction shown in Figure 3.2(b) identifies the conventional BCT and face-centered tetragonal (FCT) crystallographic unit cells which are rotated approximately 45° relative to each other. (Note: Face-centered is the crystallographic unit cell most commonly used with regard to spinel crystals. Body-centered was used by Prince

in accordance with crystallographic convention. In this work, crystallographic directions of the CCO film will use BCT indices unless otherwise specified.)

The BO_6 octahedra in spinels are often distorted by either compression or elongation along the <111> direction. In CCO, the Cr^{3+} tetrahedra depicted in Fig. 3.1(b) are compressed along and slightly twisted about one cube axis. This leads to small displacements of the Cr^{3+} cations effectively removing their centrosymmetric environment and resulting in a compression (elongation) of the c axis with respect to a FCT (BCT) unit cell.[7] However, the tetragonal distortion induced by the presence of magnetic, Jahn-Teller active $3d^9$ Cu^{2+} in the tetrahedral sites removes this degeneracy favoring an ordered state with strong competing exchange interactions in which the exchange energy between Cu^{2+} and Cr^{3+}, $H_{Cu2+-Cr3+}$, is on the order of $H_{Cr3+-Cr3+}$ using the classical Heisenberg model.[23] Here the electronic structure of $3d^9$ Cu^{2+} finds that the degeneracy of the doubly degenerate t_2 levels is removed as shown in Figure 3.3(a). Compared to other spinel-structure chromites, this results in a compressed c axis, and triangular, canted Yafet-Kittel magnetic ordering.[7,23,24] As discussed in Figure 3.3(b), moments within the (004) planes exhibit long-range, parallel alignment; however, the Cr^{3+} moments between adjacent (004) planes are canted relative to each other by the angle $\varphi_{bulk} = 151°$ (Figure 3.3(c)).[7] This results in a low magnetic moment of 0.51 μ_B f.u.$^{-1}$ which is an order of magnitude smaller than 5 μ_B f.u.$^{-1}$ of the Néel configuration.[7]
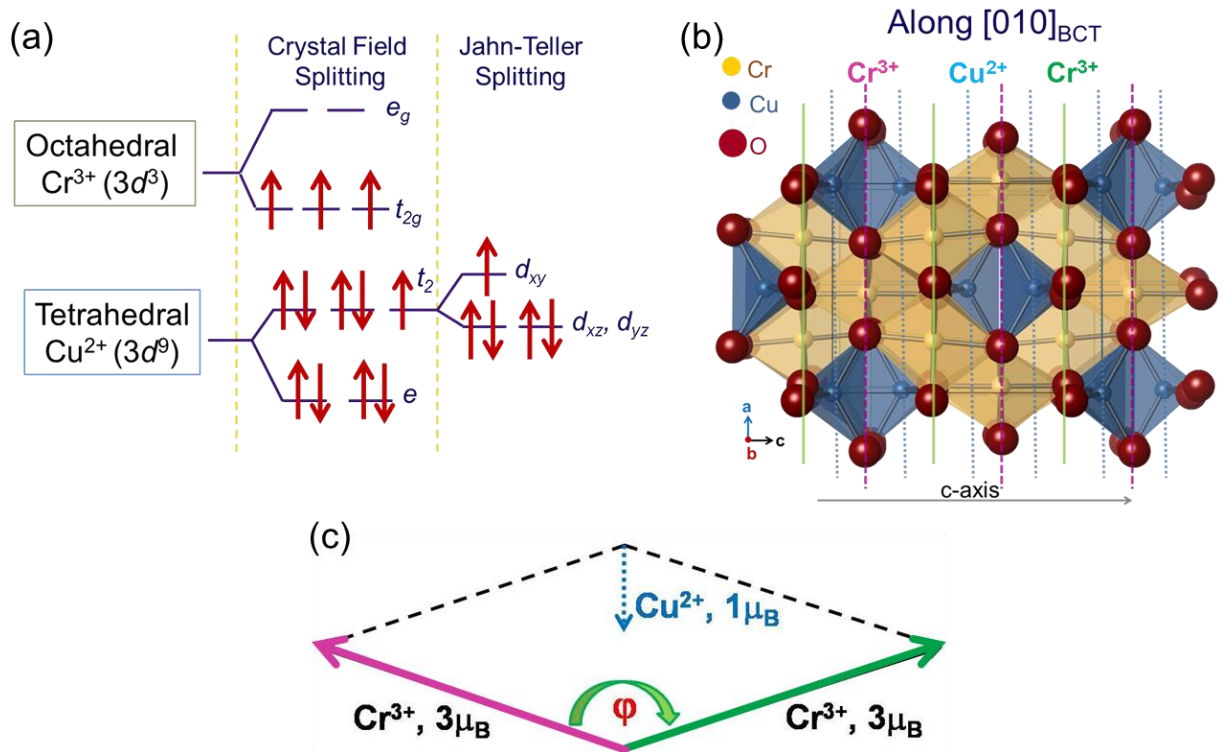
Figure 3.3. (a) The electronic structure of the valence electrons of the Cr^{3+} and Cu^{2+} cations with pertinent modifications due to crystal field and Jahn-Teller effects. (b) The CCO crystal structure viewed from the [010] BCT direction. Solid (lime) and dashed (magenta) lines highlight alternating (004) planes containing Cr and dotted (blue) lines represent (008) Cu planes. Within each (008) plane, the moments of the intraplanar cations are aligned parallel to each other in the *ab* plane; however, between nearest neighbor (004) Cr^{3+} planes, the moments

are canted with respect to each other. The Cu^{2+} moments are aligned antiparallel to the net Cr^{3+} moment. In CCO thin films, heteroepitaxy increases the distance between these planes along the c axis with respect to the FCT unit cell. (c) Canted moment configuration for one formula unit of $CuCr_2O_4$.

§3.2 Experimental Methods

$CuCr_2O_4$ thin films were grown by pulsed laser deposition on cubic (110)-oriented spinel-structure MAO (a = 8.08 Å) and (110)-oriented perovskite-structure $SrTiO_3$ (STO) (a = 3.905 Å) substrates. The films were grown at 500 °C in 15 mTorr of O_2. The KrF laser (λ = 248 nm) operated at a pulse rate of 10 Hz and fluence of ~1 J cm^{-2}. At the completion of the deposition, the films were cooled to ambient temperatures in 100 Torr of O_2. The surface topology of the films was characterized using a Digital Instruments Dimension 3100 atomic force microscope in tapping-mode to obtain the root-mean-square (RMS) roughness. The structure of the films were characterized with four-circle XRD at 8000 eV on beamline 7-2 at SSRL and by cross-sectional high-resolution transmission electron microscopy (HRTEM) using a Philips CM300FEG microscope at the National Center for Electron Microscopy at LBNL. Element-specific cation valence information was obtained from L-edge XA spectroscopy on beamlines 6.3.1 and 4.0.2 of the ALS. Site-specific elemental information was obtained from resonant X-ray scattering (RXS) measurements on beamlines 7-2 and 2-1 at SSRL. Film thicknesses were determined by RBS at the Ion Beam Analysis Facility at LBNL and confirmed by X-ray reflectivity (XRR) on a Philips Analytical X'pert MRD diffractometer.

The bulk magnetization of the CCO films was measured in a Quantum Design MPMS 5XL SQUID magnetometer. The magnetic depth profile was extracted from NR measurements performed at the NIST Center for Neutron Research on the NG-1 reflectometer. For polarized neutron reflectivity (PNR), CCO samples were field cooled at 1.5 T to 5 K and measured at 660 mT. Unpolarized NR was performed at 7 T. Both PNR and NR used the specular reflectivity geometry. Element-specific magnetic XMCD measurents were performed at 25 K in total electron yield mode at normal incidence on beamlines 6.3.1 and 4.0.2 of the ALS.

§3.3 Structural and Chemical Properties

A series of CCO thin films were grown ranging in thickness from 7 to 148 nm. To facilitate epitaxial growth, (110)-oriented substrates were used to provide a rectangular surface unit cell to tetragonal CCO as shown in Figure 3.4. For MAO substrates, the lattice mismatch along substrate edge directions were +3.8% along [001]CCO‖[001]MAO, and -5.8 % along [010]CCO‖[1$\bar{1}$0]MAO. For STO substrates, the lattice mismatch along substrate edge directions were +0.39 % along [001]CCO‖[001]STO, and -8.72 % along [010]CCO‖[1$\bar{1}$0]STO. While the mismatch along the [001] direction was significantly smaller for samples on STO compared to MAO, the mismatch along the [010]CCO direction was substantially larger for samples on STO. This arrangement placed the [001]CCO direction under tension and [010] CCO direction under compression.
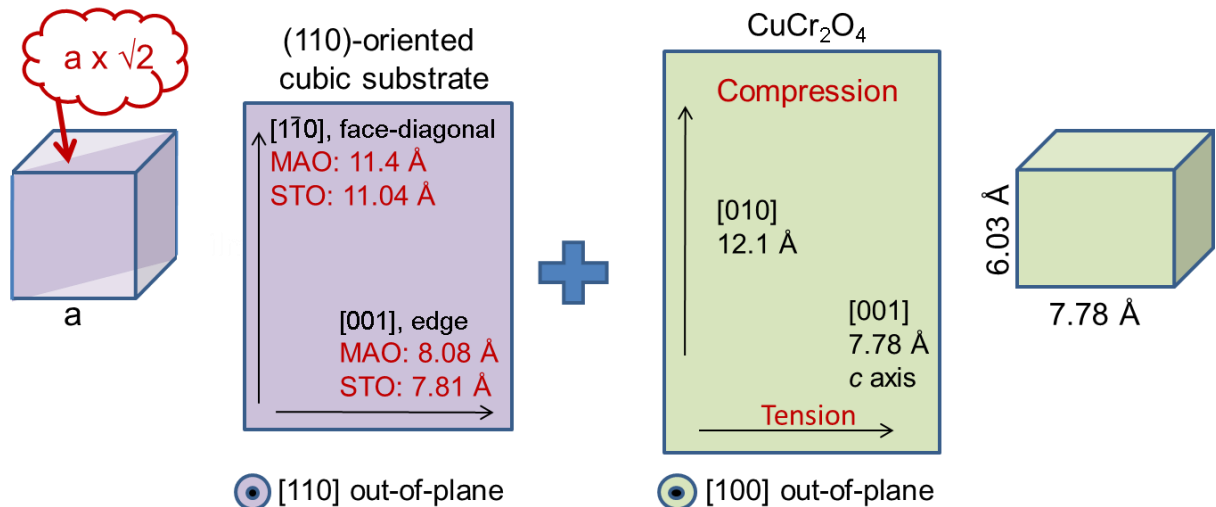
Figure 3.4. The use of (110)-oriented substrates provides a rectangular surface unit cell to facilitate epitaxial growth of tetragonal CCO.

Structural characterization revealed that CCO thin films synthesized on isostructural cubic (110) MAO substrates were smooth and highly crystalline. An AFM micrograph of a 100 nm film shown in Figure 3.5(a) exhibited a RMS roughness on the order of a unit cell (0.8 nm). Whereas, CCO films synthesized on non-isostructural, perovskite (110) STO substrates were relaxed with a rough surface topology. For a 100 nm film grown, AFM reported a RMS roughness of approximately 9 nm, an order of magnitude larger than CCO on MAO.
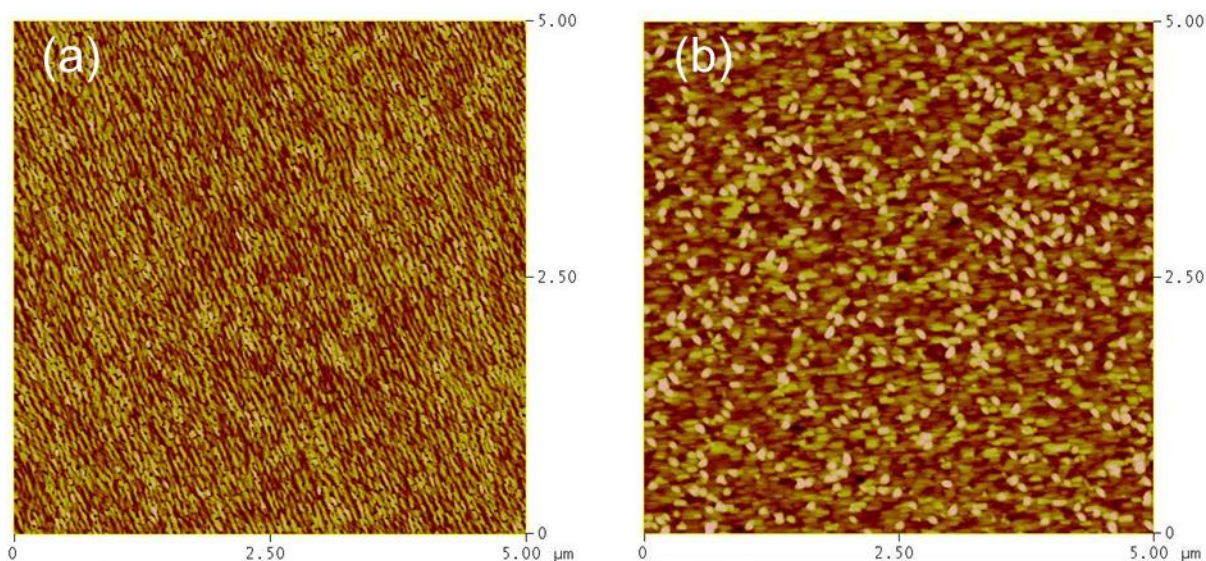
Figure 3.5. Comparison of AFM micrographs of CCO films grown simultaneously on (a) (110) MAO (RMS = 0.7925 nm) and (b) (110) STO substrates (RMS = 9.3165 nm).

HRTEM and its Fourier transform of CCO films on MAO and STO are shown in Fig. 3.6. CCO films on MAO exhibited isostructural growth; whereas CCO films on STO exhibited regions with defective stacking of the {111} planes with respect to the substrate crystal. XRD of CCO films on STO displayed similar film diffraction peak positions regardless of thickness, thus suggesting that all CCO films on STO were more or less relaxed. CCO on MAO grew epitaxially with rocking curve full-width half maxima ranging between 0.07° to 0.27°. By probing the 400, 040, 220, and 202 reflections, systematic shifts of the CCO diffraction peaks towards bulk with increasing film thickness were observed. These reflections also determined both the in-plane and the out-of-plane lattice parameters of the CCO films. Table 3.1 shows that the lattice parameters became more bulk-like for thicker films. The c/a ratio indicated reduced tetragonality for thinner films as the c/a ratio moved towards the cubic value of $\sqrt{2}$.[2] Strain calculations showed that the tensile strain along [001]CCO ranged from 0.8% to 5.3% with decreasing film thickness, and was greater than the compressive strain along [010]CCO which ranged from about -0.8% to -2.6%.
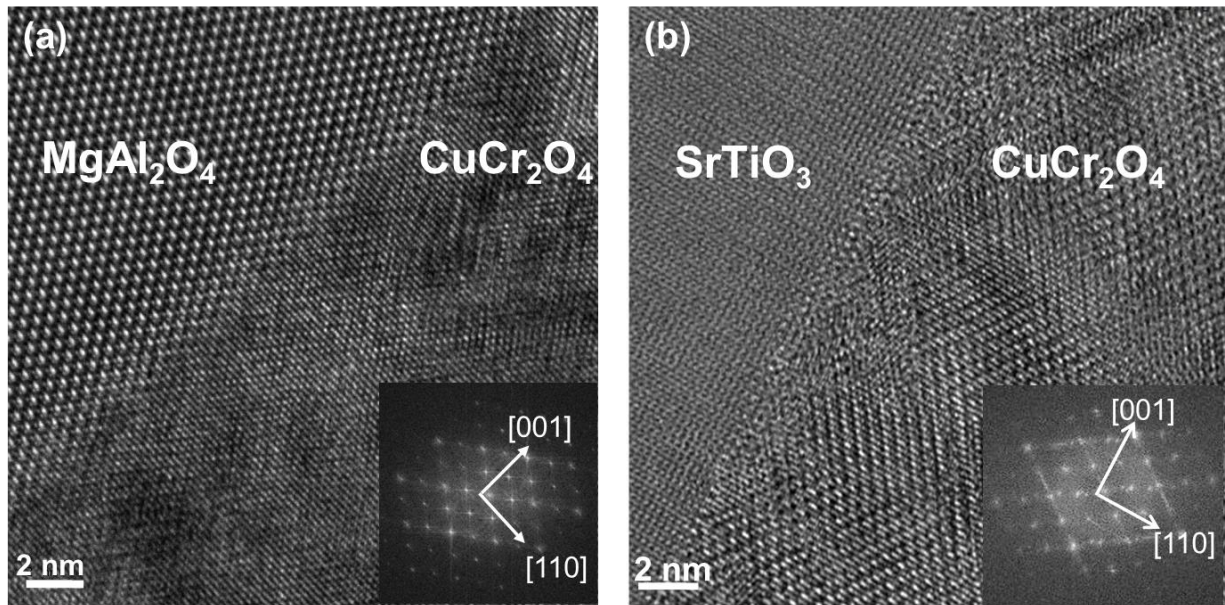
Figure 3.6. Cross-sectional HRTEM image and Fourier transform (substrate directions are shown) recorded along the [010]CCO∥[1$\overline{1}$0] substrate zone axis for (a) MAO and (b) STO. CCO films on MAO substrates show isostructural growth; whereas CCO films on STO substrates exhibit regions with defective stacking of the {111} planes with respect to the substrate crystal.
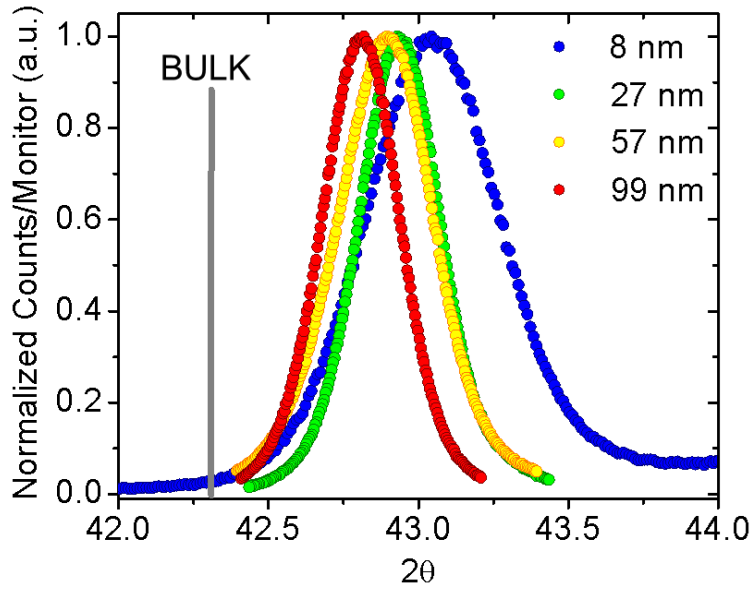
Figure 3.7. 220 BCT reflection shows shifting of peak as a function of thickness.

Table 3.1. Lattice parameters of CCO films on MAO of varying thickness as determined by XRD.

Film Thickness (nm)	a (Å)	b (Å)	c (Å)	c/a
7	5.93	5.87	8.19	1.38
27	5.93	5.94	7.95	1.34
57	5.95	5.96	7.915	1.33
71	5.95	5.96	7.89	1.325
99	5.95	5.98	7.84	1.32
BULK	6.03	6.03	7.78	1.29
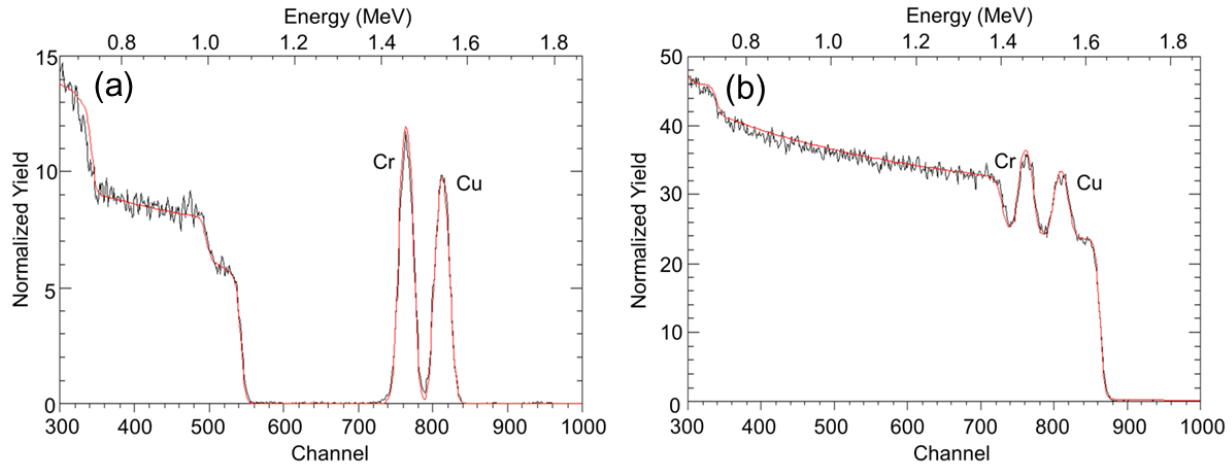
Figure 3.8. RBS spectrum (black line) and the fit to the data (red line) of a 40 nm CCO film grown on a (a) (110) MAO substrate and (b) (110) STO substrate.

RBS confirmed the thickness and 1:2 stoichiometric ratio of Cu to Cr cations, to within 5% standard error of the measurement, for the CCO films. Examples of the spectra are shown in Fig. 3.8 for films grown on (110) MAO and (110) STO, respectively. XA data in Fig. 3.9 showed that the Cr L-edge XA spectra were consistent with octahedrally-coordinated Cr^{3+} for all samples measured irrespective of substrate type.[25] However, the Cu L-edge XA spectra displayed valence charge variations. Films grown on MAO exhibited a single peak identified as Cu^{2+} whereas films on STO exhibited double peaks consistent with Cu^{2+} (L_3: 935.3 eV) and a higher energy peak (L_3: 939 eV) indicative of $3d^{10}$ Cu^{1+}.[26] The absence of XMCD at 939 eV verified non-magnetic Cu^{1+} as expected due to its full d-shell. It was initially hypothesized that sputtering a thin conductive coat of AuPd on the sample surface to prevent low temperature charging could be modifying the Cu valence states. However, this was unlikely as CCO on MAO did not have a Cu^{1+} peak. As an alternative, CCO films were grown on conductive Nb-doped (110) STO. With an identical lattice parameter to (110) STO, the conductive properties allowed for the extraction of chemical information at identical strain states eliminating the need for a AuPd cap preserving its as-grown surface properties. However, as shown in Figure 3.9(d), the presence of the Cu^{1+} peak persisted.

As enhanced magnetization was discovered in samples grown on MAO substrates, RXS was used to identify the coordination of Cu.[27] In general, for a cubic spinel, the structure factor of the 220 reflection was dependent only on the tetrahedral sites. For the 220 FCT reflection of CCO (Fig. 3.10), there was a strong decrease in the diffracted peak intensity due to absorption at the Cu K-edge. This indicated that the 220 planes were occupied by Cu with tetrahedral coordination. A nominal decrease in the 220 diffracted peak intensity at the Cr K-edge suggested a small amount, if any, of tetrahedral Cr consistent with bulk studies.[22] These studies indicated that the bulk valence states and site occupancies were robust and preserved in the thin films grown on MAO, thereby eliminating cation inversion and changing valence states as sources of the enhanced magnetization.
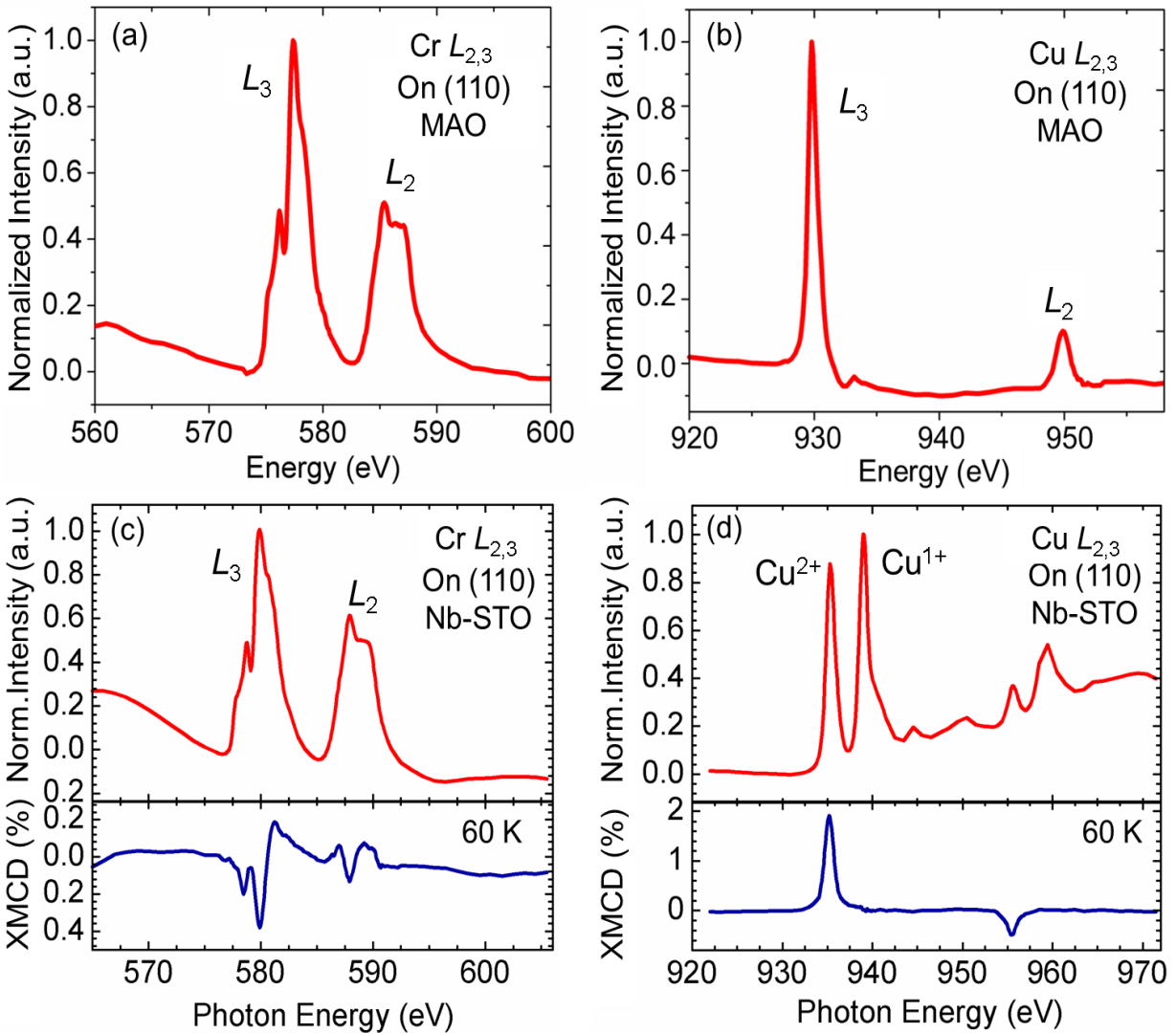
Figure 3.9. X-ray absorption at the (a) Cr and (b) Cu *L*-edges for CCO on (110) MAO. In comparison, the XA data for the (c) Cr and (d) Cu *L*-edges for CCO on (110) Nb-STO displayed identical spectra for Cr, but different spectra for Cu. XMCD data at the Cu edge determined that the extraneous peak for films grown on STO was non-magnetic in agreement with the $3d^{10}$ shell of Cu^{1+}.
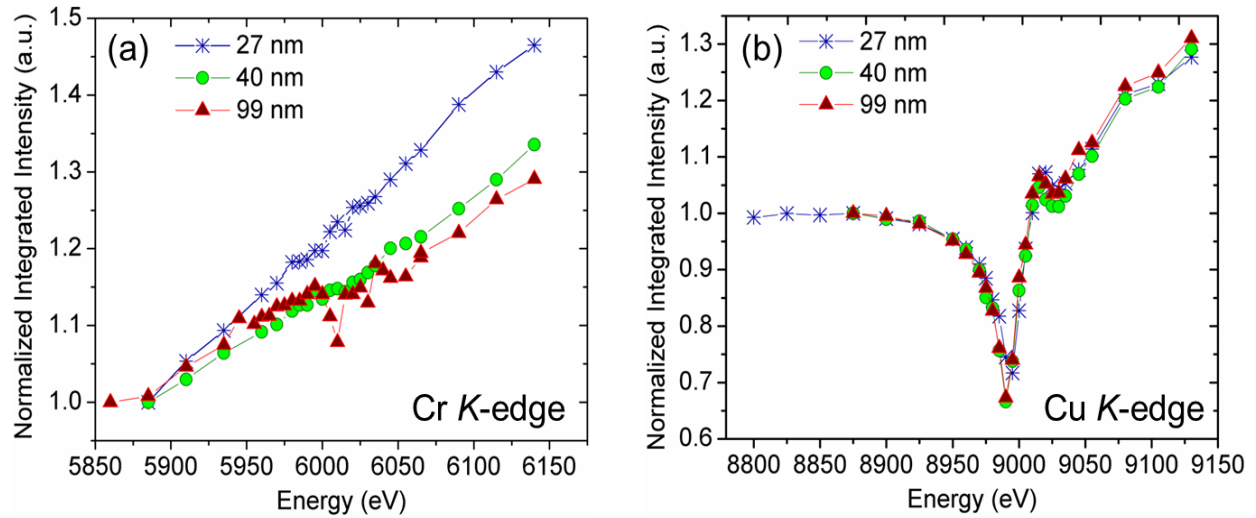
Figure 3.10. RXS of the 220 FCT reflection of CCO films with varying thickness at the (a) Cr and (b) Cu *K*-edge.

§3.4 Magnetic Properties

The more cubic unit cell of CCO thin films had strong implications on their magnetic properties due to the strong coupling between structure and magnetism. Using RBS to determine the thickness of two 99 nm CCO films grown simultaneously on STO and MAO, the hysteresis loops of these films at 5 K in Fig. 3.11(a) demonstrated differences in saturation magnetization M_s when measured with SQUID magnetometry along the out-of-plane [100]CCO. CCO on STO had a nearly bulk-like magnetization and little variation with thickness; whereas CCO on MAO exhibited a dramatically enhanced M_s exceeding that of bulk. Fig. 3.11(b) shows a general trend of higher magnetization in thinner films of CCO on MAO in which M_s values up to 1.7 μ_B f.u.$^{-1}$ were obtained when measured along the [010]CCO direction.

Furthermore, while CCO films on STO did not exhibit a definitive magnetically easy axis, CCO films on MAO displayed uniaxial magnetic anisotropy in the plane of the film. Fig. 3.12 shows that both the out-of-plane [100]CCO direction and in-plane [010]CCO direction were easy axes while the in-plane [001] direction was magnetically hard. This indicated the presence of a (001)CCO magnetically easy plane. The strong in-plane uniaxial magnetic anisotropy observed in all CCO films on MAO suggested that the origin of the anisotropy was associated with magnetocrystalline anisotropy. The uniaxial anisotropy also suggested in-plane alignment of the film crystal axes that was consistent with the description of the film-substrate lattice registry.
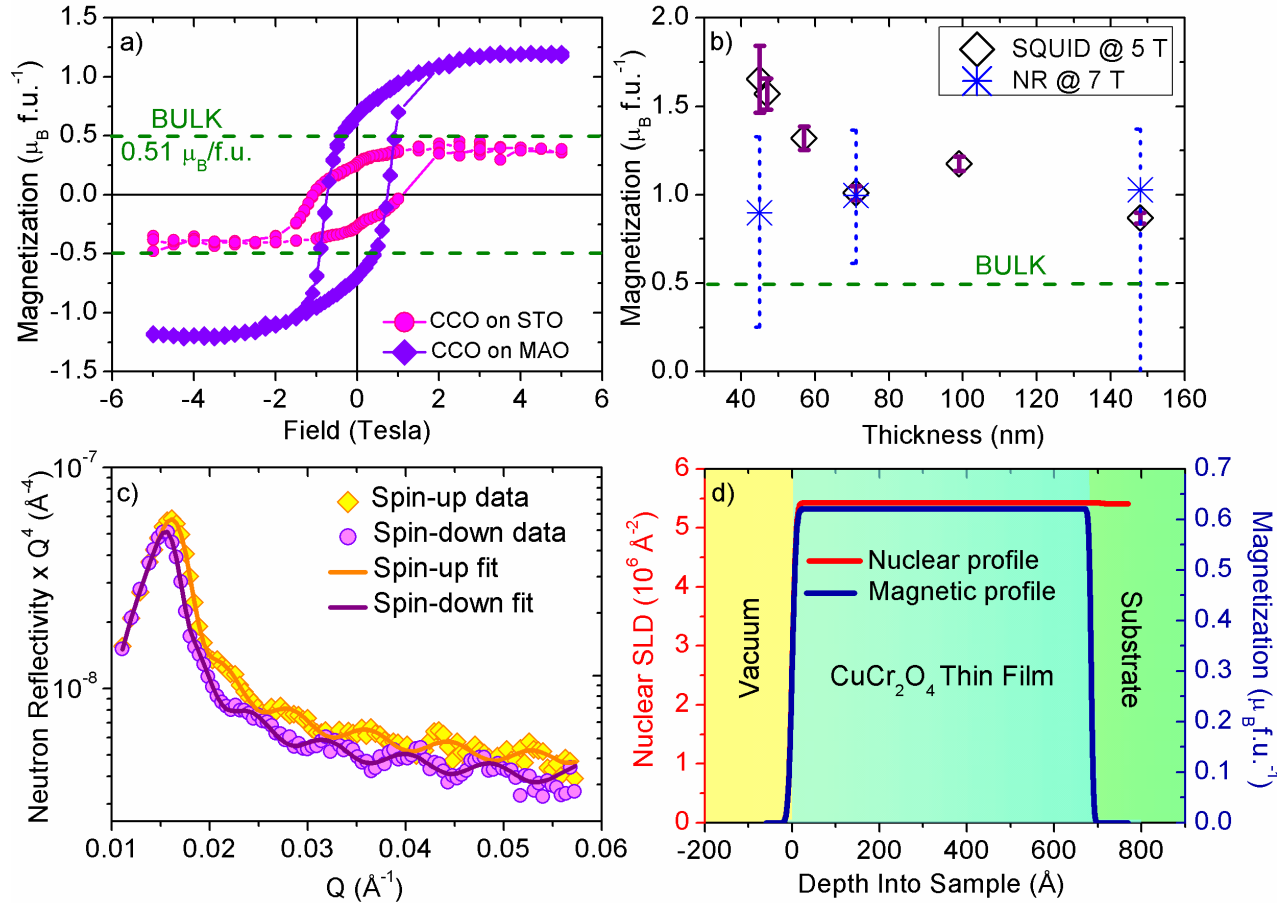
Figure 3.11. (a) Hysteresis loops for 99 nm CCO films grown on STO and MAO substrates obtained by SQUID magnetometry with an applied field along the out-of-plane [100]CCO direction. (b) M_s values for CCO films on MAO substrates of varying thickness at 5 K obtained from SQUID magnetometry and NR when measured along the in-plane [010]CCO direction. (c) PNR spectra of the spin-up and spin-down channels for a 71 nm film fitted to model the magnetic and nuclear profiles of the sample at 660 mT (unsaturated). (d) Model created to fit PNR spectra gives the depth profiles of the nuclear SLD (red line) and magnetization (blue line). The magnetic depth profile indicated uniform magnetization throughout the depth of the film.

In addition, the temperature dependence of magnetization was measured in a 1 Tesla field as shown in Fig. 3.12(c&d). The data indicated that the Curie temperature, T_C, of the films on MAO was approximately 125 K which was in close agreement with the bulk value of 135 K.[7] However, CCO films on STO exhibited a slightly smaller T_C closer to 110 K.

From these structural and magnetic measurements, the bulk-like magnetization for CCO films grown on STO was primarily attributed to lattice relaxation due to the severe mismatch along the [010]CCO direction. This mismatch could result in the combination of anti-phase boundaries and other planar defects along the <111> FCT direction. It was also possible that the presence of non-magnetic Cu^{1+} affected the existing exchange mechanisms. Of greater interest

was the origin of the observed enhanced magnetization for CCO films grown on MAO, thus the remainder of this chapter is dedicated to further exploring this topic.
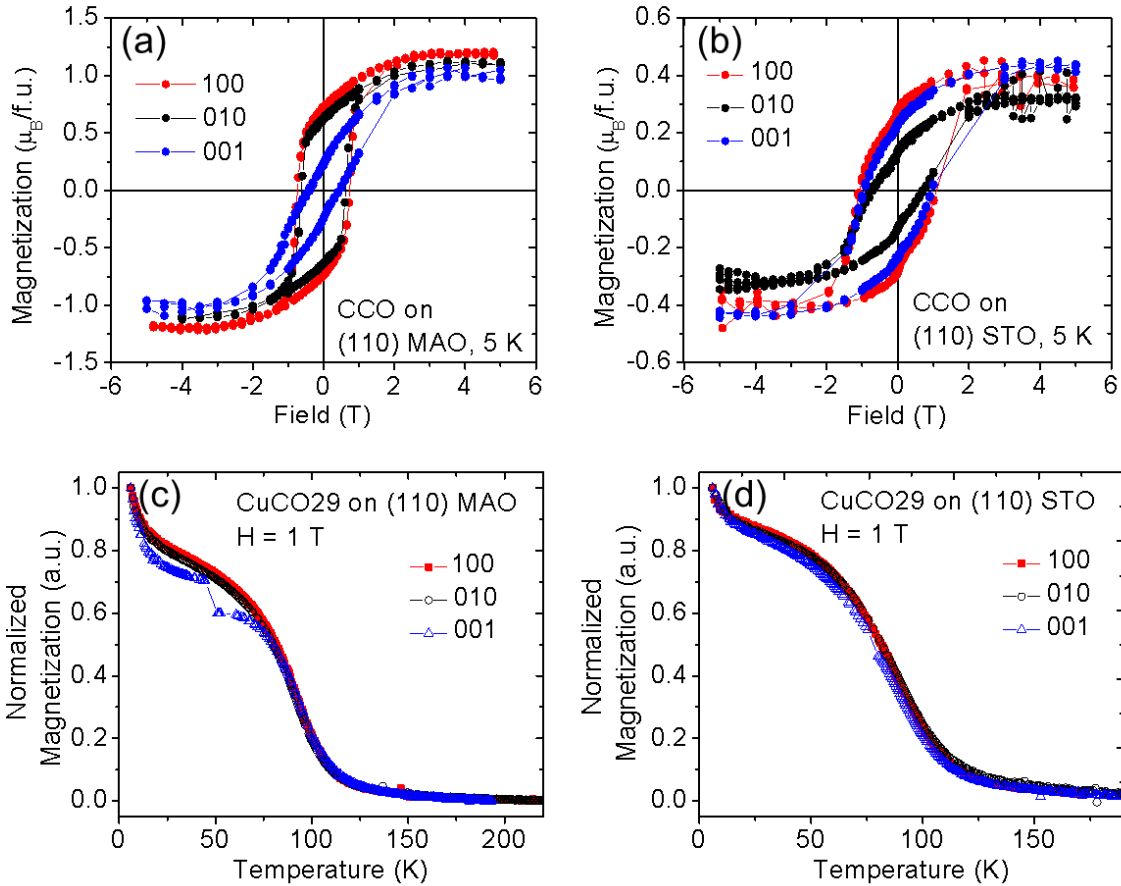
Figure 3.12. SQUID magnetometry measurements were used to obtain hysteresis loops along three orthogonal high symmetry directions to identify the presence of magnetic anisotropy in 99 nm films grown on (a) MAO and (b) STO substrates. The temperature dependence of magnetization (normalized) for CCO films was also evaluated on (c) MAO and (d) STO substrates.

To investigate the origin of the enhanced magnetization, PNR was used to probe the depth profile of CCO films as it was directly sensitive to the layer magnetization and nuclear composition.[28-30] In Fig. 3.11(c), the spin-up and spin-down non-spin flip scattering for a 71 nm film was measured with a 660 mT field applied along [010]CCO at 5 K. These spectra were sensitive only to the in-plane component of magnetization. The structure and the distinct oscillations were indicative of characteristic scattering lengths. From known isotopic scattering lengths[31] that predicted the absence of nuclear contrast and experimental verification that revealed a damped signal, it was concluded that the oscillations were due to magnetic contrast. Spin-flip scattering, which originated from a net in-plane magnetization perpendicular to the field, was absent, thus indicating a (001) magnetically easy plane. Using exact dynamical formalism,[29] the PNR data was modeled to obtain the nuclear scattering length density (SLD) and magnetization profiles of the CCO samples. Fig. 3.11(d) shows that the PNR data was

consistent with a uniform magnetization throughout the depth of the film.[32] The absence of any inhomogeneity in the magnetic profile indicated that the enhancement was due to neither interfacial nor surface effects.

To extract M_s, scattering measurements were performed at 5 K in higher fields with an unpolarized neutron beam to avoid difficulties in maintaining neutron spin orientation at high fields. As in the PNR data, any oscillation observed with unpolarized neutron reflectometry (NR) was purely magnetic in origin, thus allowing for the calculation of M_s when measured in a 7 T field. A direct comparison (Fig. 3.11(b)) of the M_s values extracted from NR and SQUID magnetometry showed that the magnetization was enhanced compared to that of bulk. For the 71 and 148 nm films, PNR corroborated the approximately twofold increase in M_s observed by SQUID. However, for the thinner 45 nm film, SQUID magnetometry indicated that the magnetization increased to nearly 1.7 μ_B f.u.$^{-1}$ while NR showed that the magnetization decreased to 0.90 μ_B f.u.$^{-1}$. This discrepancy was attributed to error associated with extracting the magnetization of the film in SQUID magnetometry; in particular, removal of the diamagnetic contribution from the MAO substrates and imperfect sample shapes.
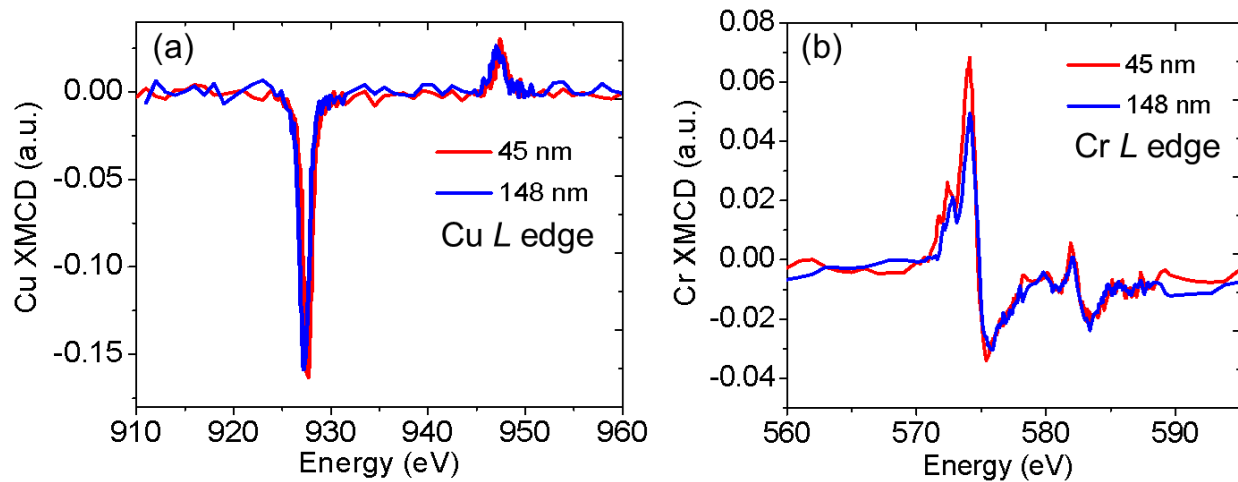
Figure 3.13. (a) Cu and (b) Cr L-edge XMCD at 25 K measured along [100]CCO.

Finally, XMCD studies were performed to investigate element-specific magnetization. Fig. 3.13 shows the Cu and Cr L-edge XMCD spectra, normalized to the incoming photon flux, for 45 and 148 nm thick CCO samples in an applied field of ±1.8 T. The anti-parallel orientation of the Cu and Cr XMCD spectra was consistent with ferrimagnetic alignment in which the net Cr moment was parallel to the applied field. The XMCD peak intensities for the Cu^{2+} and Cr^{3+} edges of the two films provide information about the origin of the changing magnetization observed in bulk measurements. According to SQUID magnetometry, the magnetization of the 45 nm film was 80-90% higher than the 148 nm film. In Fig. 3.13(a), the Cu XMCD signal of the 45 and 148 nm films were essentially the same. However, in Fig. 3.13(b) the peak Cr^{3+} dichroism signal changed approximately 30%. The discrepancy in the magnitude of the

increased magnetization between the two techniques was attributed to the low 1.8 T field that was inadequate for magnetic saturation in the XMCD measurements. Thus, the increased signal from the Cr^{3+} cations and the net Cr moment aligned parallel to the field indicated that increased magnetization of the thinner films could be attributed to more collinear moment alignment of Cr^{3+} between adjacent (004) planes.

§3.5 Discussion

In bulk CCO, the tetragonal structure and triangular ground state moment configuration were the result of competition between the exchange and Jahn-Teller energies. The reduced symmetry resulted in longer intraplanar Cr-O bonds on the (004) planes and shorter interplanar Cr-O bonds orthogonal to the plane along the c axis. This modification introduced two new exchange terms, $J'_{Cu2+-Cr3+}$ and $J'_{Cr3+-Cr3+}$ to account for the distorted c axis. Kaplan et al. used four dominant exchange interaction terms ($J_{Cu2+-Cu2+}$ is small due to proximity and thus neglected), $J_{Cu2+-Cr3+}$, $J'_{Cu2+-Cr3+}$, $J_{Cr3+-Cr3+}$, and $J'_{Cr3+-Cr3+}$, rather than two to express the magnetic coupling between the cations because $J_{Cu2+-Cr3+} \neq J'_{Cu2+-Cr3+}$ and $J_{Cr3+-Cr3+} \neq J'_{Cr3+-Cr3+}$.[10] Here $J_{Cr3+-Cr3+}$ represented the exchange coupling between Cr^{3+} cations within the same ab plane, and $J'_{Cr3+-Cr3+}$ described the Cr^{3+}- Cr^{3+} coupling between Cr^{3+} cations on different ab planes along the c axis. $J_{Cu2+-Cr3+}$ represented Cu-O-Cr superexchange coupling via Cr-O bonds within an ab plane, and $J'_{Cu2+-Cr3+}$ represented Cu-O-Cr superexchange coupling via Cr-O bonds between the ab planes. In CCO films, lattice distortions induced by substrate strain modified the strength of these exchange interactions which led to enhanced magnetization. The exchange interactions were governed by nearest neighbor interactions which included an approximately 125º antiferromagnetic superexchange between Cu^{2+} - Cr^{3+}, 90º ferromagnetic superexchange between Cr^{3+} - Cr^{3+}, and antiferromagnetic direct exchange between the Cr^{3+}- Cr^{3+}.[33] The largest induced lattice distortion arising from epitaxy was the elongation of the c axis with respect to a BCT unit cell, as shown in Table 3.1, which increased the symmetry of CCO by stabilizing a more cubic unit cell and reduced the degree of direct overlap between Cr^{3+} orbitals on (220) and ($2\bar{2}0$) planes.

These results demonstrated a route for using heteroepitaxy to stabilize greater magnetic ordering in canted magnetic systems. To account for the magnetic enhancement in epitaxial CCO films, lattice distortions induced by epitaxial strain reduced the frustration thereby allowing for the rotation of the Cr^{3+} moments towards a more collinear alignment. The degree of moment rotation for Cr^{3+}, represented by φ, could be estimated from SQUID magnetometry data assuming negligible out-of-plane moment rotations. While octahedra rotations were possible, their effects were difficult to quantify with the characterization techniques used. (PNR could not rule out the presence of tilting of the magnetization away from the field direction). The magnetization values in Fig. 3.13(b) were consistent with ferrimagnetic alignment between Cr^{3+} and Cu^{2+} with φ ranging between 121º - 142º compared to the bulk value of 151º. For tetragonal CCO, Kaplan showed that the angle of canting was related to the ratio of three exchange terms in which $\cos(\varphi/2)=(2J_{Cu2+-Cr3+} + J'_{Cu2+-Cr3+})/(4 J'_{Cr3+-Cr3+})$.[34] As φ was lower in thin films than in bulk, the strength of the exchange interactions in CCO was affected by lattice distortions induced by heteroepitaxy. The reduction in interaction strength between interplanar Cr^{3+} predominantly affected the associated exchange terms, $J'_{Cu2+-Cr3+}$ and $J'_{Cr3+-Cr3+}$.

Concomitant with the modified orbital overlap, it was believed that the decreased $J'_{Cr3+-Cr3+}$ has a greater effect than the decreased $J'_{Cu2+-Cr3+}$, thus resulting in a decrease in φ and moment canting and an increase in enhanced magnetization.

Finally, the nature of magnetism in CCO precluded the stabilization of alternative spin configurations. The magnetization in the films was too low for a Néel configuration. Long-range, coherent spiral ordering or uniform canting in one direction away from the field was also unlikely as PNR measurements found the absence of spin-flip scattering, thus indicating that there was no net [001] magnetization. Furthermore, despite lattice strains, the CCO films remained non-cubic which made the Yafet-Kittel canted spin configuration likely as predicted by theoretical studies.[34]

§3.6 Conclusion

In conclusion, the experimental results presented in this chapter demonstrated the ability to induce greater spin alignment in canted, magnetically-frustrated CCO thin films via heteroepitaxy. By stabilizing a more cubic unit cell, the observed enhanced magnetization of the CCO films could be understood in terms of reducing the frustration of the magnetic lattice of CCO and modifying the strength of competing exchange interactions.

Oxide-based magnetic tunnel junctions (MTJs) display unusual properties distinctly different from conventional ferromagnetic/nonmagnetic insulator/ferromagnetic MTJs. This chapter highlights the remarkable observation of magnetic and resistive switching with junction magnetoresistance (JMR) values up to -6% in magnetic tunnel junctions comprised entirely of magnetic oxides. Ferrimagnetic $CuCr_2O_4$ is incorporated as a tunnel barrier in magnetic tunnel junctions with ferromagnetic $La_{0.7}Sr_{0.3}MnO_3$ and Fe_3O_4 electrodes. XMCD studies reveal a proximity-induced magnetism at the $CuCr_2O_4$ barrier-Fe_3O_4 electrode interface which is thought to arise from the modulation of the Cr moments by the Fe_3O_4. Magnetotransport data demonstrates that JMR has a local minimum at zero bias and a maximum at a finite applied bias. This origin of this anomaly known as the bimodal bias dependence is attributed to contributions from the Fe_3O_4 electrode and the magnetic tunnel barrier.

§4.1 Introduction to Oxide Magnetic Tunnel Junctions
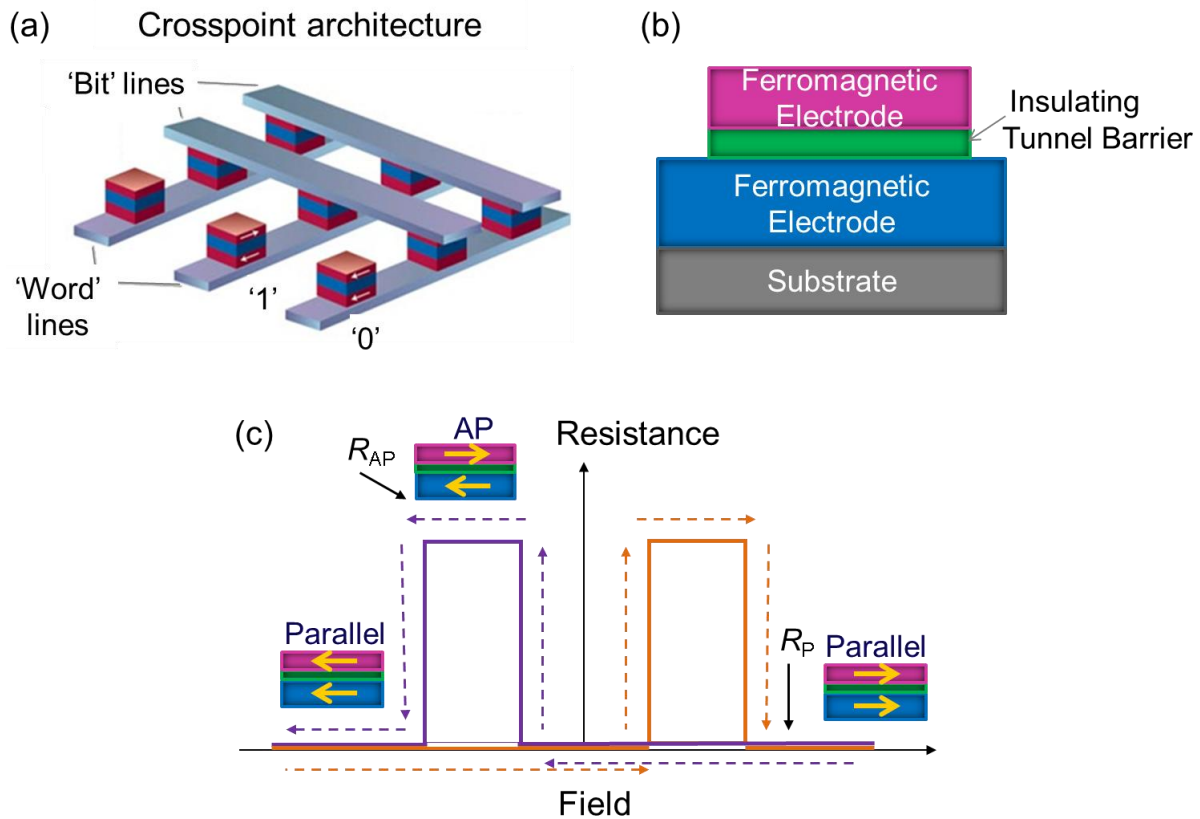
Figure 4.1. (a) Crosspoint architecture used to create arrays of magnetic junction devices.[1] (b) Schematic of a magnetic tunnel junction. (c) Field-dependent resistance of a conventional

magnetic tunnel junction. Corresponding MTJ stacks illustrate the magnetic orientation of the electrodes with applied field.

Magnetic tunnel junctions are the building blocks that enable magnetic recording devices such as magnetic random access memory and magnetic sensors. Easily integrated into a crosspoint array shown in Figure 4.1(a),[1] a magnetic tunnel junction consists of two ferromagnetic electrodes separated by an insulating tunnel barrier (Figure 4.1(b)). When current is passed through a junction, the relative orientation of the electrode magnetization determines the resistance. Jullière developed a simple model relating the JMR of a MTJ to the spin polarization of its ferromagnetic electrodes.[2] In a ferromagnet, exchange splitting separates the conduction band into spin-up and spin-down sub-bands. Spin polarization describes the imbalance of spins at the Fermi level that participate in conduction.

In tunneling, the orientation of the electron spin is conserved. Considering the density of states near the Fermi level for each electrode, parallel magnetization of the electrodes corresponds to a low resistance state as spin-up electrons in one electrode have available spin-up states in the other electrode to tunnel into. This results in a high tunneling probability. In an anti-parallel configuration, there are fewer spin-up states available for spin-up electrons to tunnel into resulting in a low tunneling probability and a high resistance state. To achieve distinct resistance states, electrode materials with different coercivities are selected. To control the magnetic orientation of the electrodes, a sweeping magnet field is applied as shown in Figure 4.1(c).

JMR is the key figure of merit for evaluating MTJ performance. It is defined as

$$JMR = \frac{R_{AP} - R_P}{R_{AP}} \times 100,$$

(4.1)

where R_{AP} is the resistance when the magnetization of the electrodes are anti-parallel and R_P is the resistance when they are parallel. Using Jullière model, JMR is defined as

$$JMR = \frac{2P_1 P_2}{1 - P_1 P_2} \times 100,$$

(4.2)

where the spin polarization, P, resulting from the imbalance of spin at the Fermi level and is expressed as

$$P = \frac{N^{\uparrow} - N^{\downarrow}}{N^{\uparrow} + N^{\downarrow}},$$

(4.3)

where $N^{\uparrow}$ is the density of states of spin-up electrons at the Fermi level and $N^{\downarrow}$ is the density of states of spin-down electrons at the Fermi level. P_1 and P_2 represent the spin polarizations of each electrode. With these definitions, Jullière assumed that the junction conductance is a sum of the conduction in each spin channel; there is no spin flip scattering during tunneling; and conduction from each spin channel is proportional to the product of the density of states at the Fermi level for that spin orientation for both electrodes. From the definitions presented in equations 4.3 and 4.4, Jullière's model depends on the spin polarization of the two

ferromagnetic electrodes thereby emphasizing the importance of selecting electrodes with high spin polarization in order to maximize JMR. One approach is the use of half-metallic electrodes. By definition, a half-metal is one in which the electrons at the Fermi level are of only one spin orientation yielding a spin polarization of 100%. While there are several classes of oxides which demonstrate half-metallicity, the half-metals selected for electrodes in the magnetic junctions presented in this chapter are the doped-manganite, $La_{0.7}Sr_{0.3}MnO_3$ (LSMO) and spinel-structure magnetite, Fe_3O_4. LSMO is a ferromagnetic perovskite with a $T_C \sim 355$ K. Fe_3O_4 is a ferrimagnetic inverse spinel with a $T_C \sim 858$ K. Fe_3O_4 has been studied extensively as it undergoes a charge-ordering phase transition which gives rise to a metal-insulator transition known as the Verwey transition. [3,4] The temperature at which this transition occurs is known as the Verwey temperature, T_V. At the bulk Fe_3O_4 $T_V \sim 120$ K, ordering of the Fe^{2+} and Fe^{3+} cations is observed on the octahedral sites. This ordering is coincident with a decline in resistivity and the opening up a charge gap in the conduction band. However, Fe_3O_4 thin films do not exhibit a distinct metal-insulator transition and will be discussed later in this chapter. Together, the LSMO-Fe_3O_4 electrode combination has demonstrated JMR as large as -25% and has given rise to properties different from conventional ferromagnet/insulator/ferromagnet (F/I/F) MTJs.[5-7]

The Jullière model is often cited as an oversimplified model as it neglects the importance of the tunnel barrier and interfacial properties. More recently, MTJs with MgO tunnel barriers have exhibited tunneling magnetoresistance (TMR) values using the definition $TMR = \frac{R_{AP} - R_P}{R_P} \times 100$ as high as 600% and has drawn attention to the role of the tunnel barrier in the tunneling process.[8] Magnetism in the barrier was also thought to cause spin memory loss and spin scattering. [9] However, the large JMR values in LSMO-Fe_3O_4-based junctions with both nonmagnetic and ferrimagnetic barriers have demonstrated the importance of spin filtering role of the barrier as well as the interfaces.

Additionally, there have been reports of a puzzling zero bias anomaly often observed in MTJs with a Fe_3O_4 electrode. More recently, this anomaly has also been observed in MTJs with a magnetic barrier. Rather than a maximum JMR at zero bias, the JMR exhibits a local minimum at zero bias and a maximum JMR at a finite applied bias. This anomaly is referred to as a bimodal bias dependence and its origin has been debated. Is the origin associated with the Fe_3O_4 electrode or is it a signature of the spin filtering phenomenon in the tunnel barrier? Panchula reported the bimodal bias dependence in MTJs with polycrystalline Fe_3O_4 attributing it to small amounts of local positive spin polarization sources intrinsic to the octahedral sites.[10] Some point to the opening up of the 100-150 meV charge gap in Fe_3O_4.[11,12] Alldredge *et al.* showed that Fe_3O_4-based junctions with nonmagnetic and paramagnetic tunnel barriers both exhibit a thickness-dependent bimodal bias dependence; barriers approximately 5 nm thick exhibit this behavior but 8 nm thick barriers do not.[13] Others presented evidence that the origin of the zero bias anomaly resided with the tunnel barrier. Saffarzadeh predicted that a bimodal dependence is a signature of spin filtering, and this prediction has been experimentally verified in magnetic tunnel junctions with Co and Al or Pt electrodes.[14-16] Finally, Hu *et al.* and Chopdekar *et al.* presented evidence of a temperature dependence of the bimodal bias dependence using an Fe_3O_4 electrode and a ferrimagnetic barrier.[17-18]

In this work, magnetotransport measurements demonstrate another instance of the bimodal bias dependence in LSMO/CuCr$_2$O$_4$/Fe$_3$O$_4$ magnetic tunnel junctions. Using the LSMO-Fe$_3$O$_4$-electrode combination, the tetragonal spinel CuCr$_2$O$_4$ is examined as a tunnel barrier in lieu of other chromites for its higher T_C of 125 -135 K which could stabilize large JMR values at higher temperatures.[19] These junctions exhibit distinct magnetic switching of the electrodes and surprising resistive switching with JMR values near -6%. Element-specific XMCD further probe the switching characteristics and identify decoupling at the LSMO electrode-CCO barrier interface while uncovering evidence of a Fe$_3$O$_4$ proximity-induced magnetism in the Cr at the exchange coupled CCO barrier-Fe$_3$O$_4$ electrode interface. Furthermore, magnetotransport properties are investigated with regard to temperature and barrier thickness. In particular, the bimodal bias dependence exists over an intermediate temperature regime. Its origin is affected by the exchange splitting of the magnetic barrier and the band structure of the Fe$_3$O$_4$ electrode. Conductance studies indicate a power law dependence that can be fit to inelastic hopping at low temperatures and low biases with deviation at high biases.

§4.2 Experimental Methods

Magnetic junction heterostructures of LSMO/CCO/Fe$_3$O$_4$ (perovskite/spinel/spinel), non-isostructural bilayers of LSMO/CCO, isostructural bilayers of CCO/Fe$_3$O$_4$, and single films of CCO are synthesized by pulsed laser deposition using a KrF laser ($\lambda = 248$ nm) on (110) SrTiO$_3$ (STO) (a= 3.905 Å). Deposition parameters for the heterostructure layers are as follows: LSMO at 700 ºC in 320 mTorr of O$_2$, CCO in 15 mTorr of O$_2$ at 500 ºC, and Fe$_3$O$_4$ in vacuum better than 4 x 10^{-6} Torr at 400 ºC. Layer thicknesses are determined by RBS at the Ion Beam Analysis Facility at LBNL. Junctions ranging in size from 4 x 4 μm^2 up to 40 x 40 μm^2 are fabricated using conventional photolithography and Ar ion beam milling described in Appendix A.

Characterization studies of the magnetic junction heterostructures included structural, chemical, magnetic, and transport measurements. XRD is performed on a Philips Analytical X'pert MRD diffractometer. Bulk magnetization measurements are performed in a Quantum Design MPMS 5XL SQUID magnetometer. Transport measurements are performed with a Quantum Design Physical Property Measurement System using the current perpendicular to plane (CPP) geometry with the magnetic field applied in-plane along the [001] direction. Element-specific XA spectroscopy and XMCD are performed in total electron yield mode in grazing 60º incidence at beamlines 6.3.1 and 4.0.2 of the ALS at LBNL. XMCD measurements use an applied field of up to ±1.5 Tesla from 60-300 K along the [001] direction.

§4.3 Structural Properties

XRD shows that the trilayer heterostructures are single phase and grow epitaxially on (110) STO substrates. AFM images depict smooth multilayers that exhibit RMS values between 0.8 -1.5 nm (Fig. 4.2). The thickness of the LSMO bottom electrode is between 80 – 90 nm, the Fe$_3$O$_4$ top electrode is between 15 – 20 nm, and the CCO tunnel barrier ranges in thickness

between 2.8 – 8 nm to within 5% standard error of the measurement as determined by RBS. XA spectra of the Cr $L_{2,3}$-edge is consistent with octahedrally-coordinated Cr^{3+}.[20] Cu XA spectra is predominantly Cu^{2+} although non-magnetic $3d^{10}$ Cu^{1+} is observed.[21] The presence of Cu^{1+} is consistent with single films of CCO grown on (110) STO substrates.
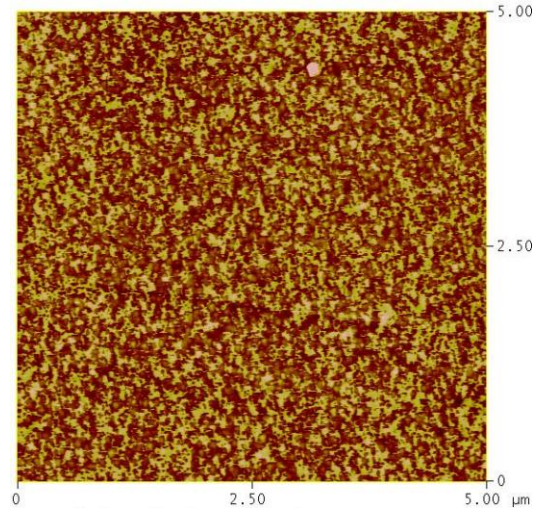
Figure 4.2. AFM micrograph of a $LSMO/CCO/Fe_3O_4$ heterostructure grown on (110)-oriented STO (RMS = 1.245 nm).
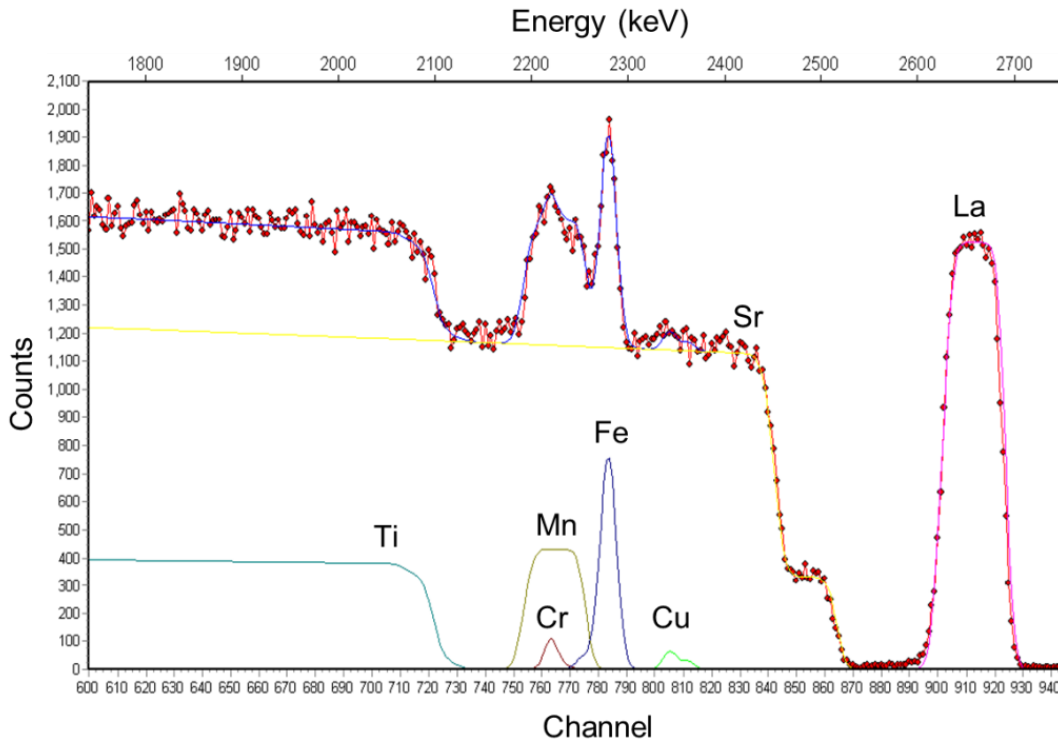
Figure 4.3. RBS spectrum (red circles + red line) and the fit to the data (blue line) of a 86 nm LSMO/ 4.25 nm CCO/ 23 nm Fe_3O_4 heterostructure grown on a STO substrate. Elemental edges are noted.

§4.4 Magnetic Properties

Magnetic hysteresis loops in Figure 4.4(a) clearly show distinct switching of the ferromagnetic electrodes with well-defined parallel and anti-parallel magnetization states. Switching of the LSMO electrode corresponds to a coercive field of approximately -100 Oe; and switching of the Fe_3O_4 electrode corresponds to a coercive field that lies near -1000 Oe. Single films of LSMO and Fe_3O_4 as well as LSMO/CCO/Fe_3O_4 trilayers show uniaxial anisotropy with an easy axis along the in-plane [001] direction. However, 40 nm single films of $CuCr_2O_4$ exhibit a T_C of ~110 K with bulk-like magnetization and the absence of a distinct magnetic easy direction. However, the significantly greater volume of the electrodes compared to the ultrathin CCO barrier, in addition to the larger bulk moment of the electrodes (LSMO: 3.67 μ_B/Mn, Fe_3O_4: 4 μ_B/formula unit (f.u.)) compared to that of CCO (0.51 μ_B/f.u.), make it difficult to resolve the magnetic contribution from and switching properties of $CuCr_2O_4$ as the total magnetic moment of the trilayers is overwhelmed by signal from the electrodes.
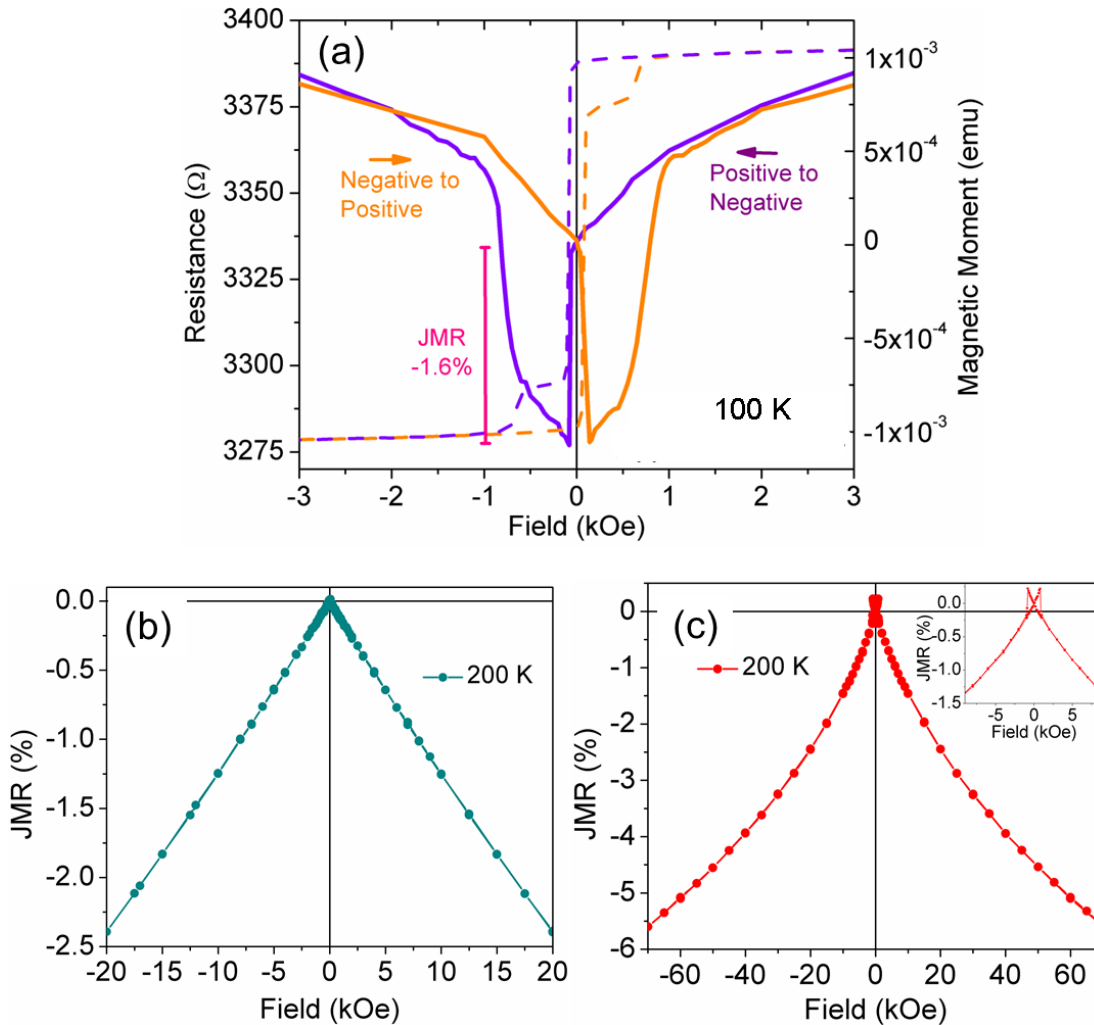
Figure 4.4. (a) Switching characteristics of LSMO/CCO/Fe$_3$O$_4$ junctions at 100 K. The solid line represents the resistance as a function of applied field. The dashed line represents the magnetic moment as a function of applied field. (b) JMR of LSMO electrode at 200 K. (c) JMR of Fe$_3$O$_4$ electrode at 200 K.

To probe the switching properties of the CuCr$_2$O$_4$ tunnel barrier and coupling at its electrode interfaces, element-specific XMCD hysteresis loops are employed. These experiments utilize two bilayer samples: 81 nm of LSMO capped with 5 nm of CuCr$_2$O$_4$ and 23 nm CuCr$_2$O$_4$ capped with 5 nm of Fe$_3$O$_4$ and extract information from the magnetic elements present at each interface from 60 to 200 K. Significant sample charging occurs at temperatures below 60 K. This temperature range includes temperatures below and above the bulk T_C of CCO at which CCO exhibits paramagnetic and ferrimagnetic behavior, respectively. At the isostructural interface of the CCO/Fe$_3$O$_4$ bilayer (Fig. 4.5(a)), coincident Fe and Cr hysteresis loops are observed at 60 K and persist until 150 K, thus indicating they are strongly magnetically coupled in this temperature range. However, compared to the hysteresis loops of Cr and Fe, Fig. 4.5(a) shows the Cu hysteresis loop exhibits slight deviations. These deviations are partially attributed

to linear drift during the measurement, but also indicate that Cu is not as strongly coupled to the Cr and Fe moments. At 200 K (Fig. 4.5(c)), the Cr-Fe coupling weakens as each element begins to exhibit slightly different magnetization processes.

At the non-isostructural interface of the LSMO/CCO bilayer, Fig. 4.5(b) displays the hysteresis loops of Mn, Cr, and Cu at 60 K. A maximum applied field of ±1.7 T is insufficient for saturating the Cu and Cr moments. However, the Mn in the LSMO electrode has a soft hysteresis loop saturating at a small field of approximately 300 Oe which is close to bulk SQUID magnetometry values of the same samples. Variations in coercivity of electrode material is attributed to variations in thickness. In any case, the LSMO and magnetically harder CCO are very weakly exchange coupled, if at all, allowing for independent switching.

The observation of decoupling at the non-isostructural LSMO-spinel interface and strong coupling at the isostructural spinel-Fe_3O_4 interface has been reported previously.[7,22] As an example, strong exchange coupling was observed at the interface of Fe_3O_4 and $CoCr_2O_4$. Similar behavior is observed in LSMO/CCO and CCO/Fe_3O_4 bilayers except that $CuCr_2O_4$ is not as strongly coupled to the Fe_3O_4 electrode as indicated by the elemental hysteresis loops of Cu, Cr, and Fe. The bulk T_C of $CoCr_2O_4$ (T_C = 95 K) is lower than the bulk T_C of CCO (T_C =125-135 K), yet Cr-Fe coupling was observed until 500 K. This is not the same for the Cr-Fe coupling at the CCO-Fe_3O_4 interface as it diminished by 200 K. Compared to $CoCr_2O_4$ (a=8.33 Å), the suppressed coupling at the CCO-Fe_3O_4 interface can be explained by the severe tetragonality of CCO (a=8.55 Å, c/a = 0.91) which results in greater lattice mismatch with Fe_3O_4 (a= 8.396 Å) and lattice distortions that weaken the interfacial exchange coupling.[23]
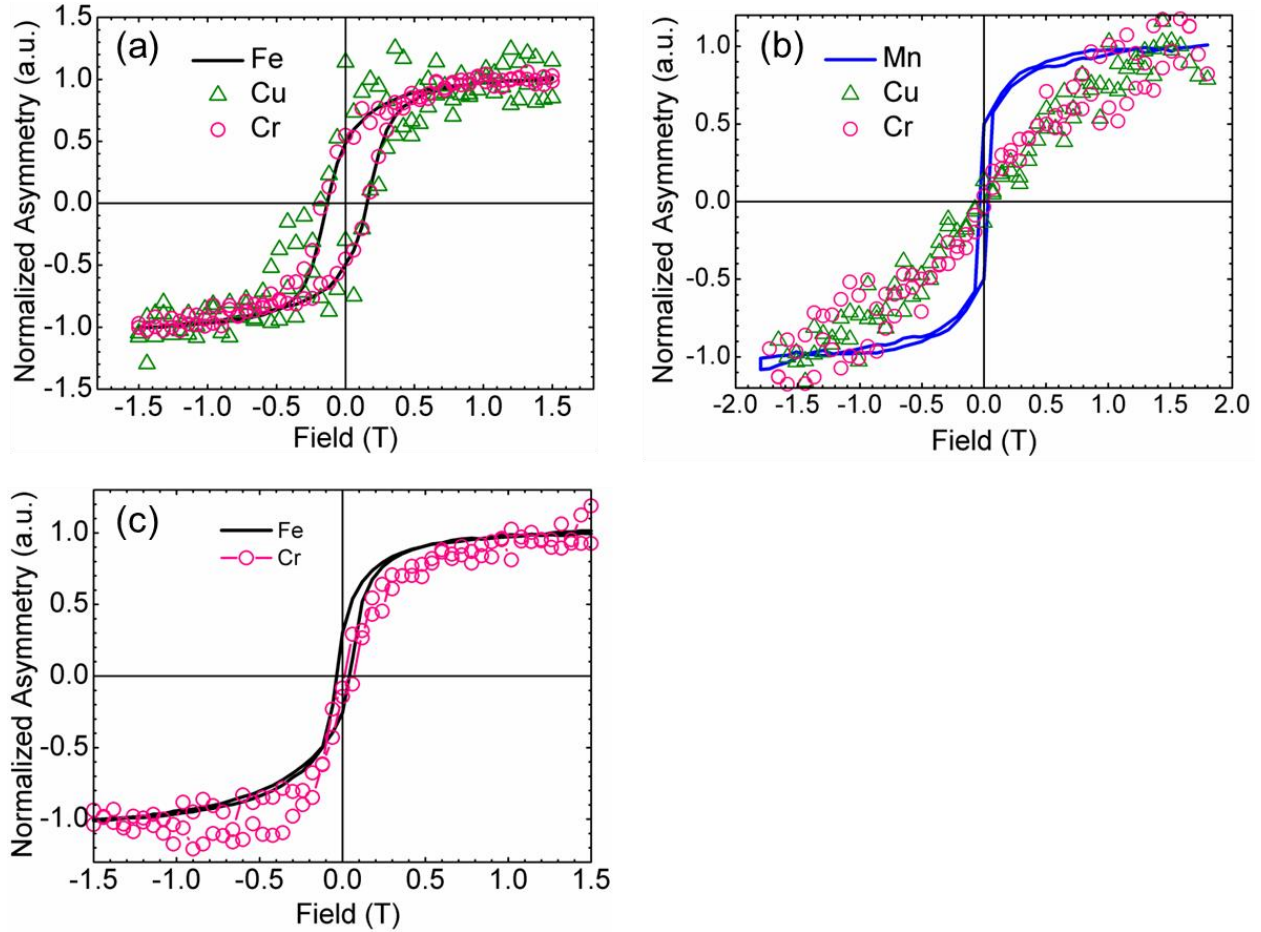
Figure 4.5. (a) Element-specific hysteresis loops of a CCO/Fe$_3$O$_4$ bilayer measured at 60 K find strong interfacial coupling between the Fe (electrode) and Cr (barrier), and to a lesser extent Cu (barrier). (b) Element-specific hysteresis loops at the interface of a LSMO/CCO bilayer reveal the absence of coupling between the Mn (electrode) and the Cr and Cu (barrier) at 60 K. (c) At 200 K, the coupling between the Cr and Fe at the CCO/Fe$_3$O$_4$ interface appears weakened.

 While there is weakened coupling between the Cr and Fe at the CCO/Fe$_3$O$_4$ interface, coupling is observed above the CCO T_C. The temperature dependence of the element-specific magnetism is examined with XMCD at the Cu, Cr, and Fe $L_{2,3}$ edges. Figure 4.6(c) of the Cu L-edge exhibits clear XMCD at 60 K. With increasing temperature, the XMCD rapidly decreases disappearing by 125 K. In comparison, from 60 - 300 K, XMCD is observed at the Fe and Cr L-edges as shown in Figure 4.6(a,b). This is expected for Fe as Fe$_3$O$_4$ has a T_C of 860 K which is well above room temperature. However, CCO is a ferrimagnet. As discussed in §1.6, ferrimagnets are composed of two magnetic sublattices. The magnetization of each sublattice has its own temperature dependence but must share the same Curie point in order to ferrimagnetically order. As a consequence, it is expected that the magnetization of the Cu and Cr sublattices will go to zero at the same temperature. Therefore, it is surprising that the Cu dichroism disappears by 125 K, yet the Cr dichroism continues to 300 K, the highest temperature measured.

To investigate the persistent Cr XMCD at the CCO/Fe$_3$O$_4$ interface, single films of CCO are grown on conductive Nb-doped (110) STO which shares an identical lattice parameter to (110) STO. While present at 60 K, Cr XMCD is not observed above the T_C of CCO at 200 K as shown in Figure 4.6(d). The magnetism induced at the spinel-Fe$_3$O$_4$ bilayer interface at elevated temperatures has been observed in other isostructural spinel- Fe$_3$O$_4$ interface systems.[22,24] In each case, the formation of an alternative spinel phase in an interdiffused region of the interface was present. Nelson-Cheeseman *et al.* reported strong coupling at the NiMn$_2$O$_4$/Fe$_3$O$_4$ interface attributed to the presence of ferrimagnetic NiFe$_2$O$_4$- and MnFe$_2$O$_4$-like spinel phases which are readily formed in bulk. A more specific study of chromite spinel (ACr$_2$O$_4$)/Fe$_3$O$_4$ interfaces by Chopdekar *et al*. has ascertained that Cr diffusion into the Fe$_3$O$_4$ induces proximity-based ferromagnetic order that extends beyond the experimentally-determined 4 nm diffusion region. At the CuCr$_2$O$_4$/Fe$_3$O$_4$ interface, the spinel phases achievable in bulk are FeCr$_2$O$_4$ and CuFe$_2$O$_4$. However, since Cr and Cu XMCD are present at 100 K, FeCr$_2$O$_4$ with a bulk T_C of 74 K is unlikely.[25] Alternatively, because there is no Cu XMCD above 125 K, the formation of CuFe$_2$O$_4$ with a bulk T_C of 725-775 K is also unlikely. Furthermore, CuFe$_2$O$_4$ is an inverse spinel and CuCr$_2$O$_4$ is a normal spinel. This means that Cu^{2+} should occupy the octahedral sites in CuFe$_2$O$_4$, and the tetrahedral sites in CuCr$_2$O$_4$. A comparison of the Cu XA and XMCD spectra for CuCr$_2$O$_4$ single films and the CuCr$_2$O$_4$/Fe$_3$O$_4$ bilayer shows no difference in the absorption energy peak position suggesting that the Cu remains tetrahedrally-coordinated.[26]. However, the Cu $L_{2,3}$, edge also lacks fine features. Chemical fingerprinting relies on fine features and their energy positions to identify coordination. Therefore, it is difficult to make a definitive conclusion regarding the coordination of the Cu^{2+} cation as it is unclear how the Cu XA and XMCD spectra would be affected with different coordination. Finally, there is no expected difference in the Cr coordination as CuCr$_2$O$_4$ and FeCr$_2$O$_4$ are both normal spinels with octahedrally-coordinated Cr. However the formation of either FeCr$_2$O$_4$ or CuFe$_2$O$_4$ seems unlikely.

While it is plausible that Cr diffusion could be the source of the interfacial magnetism in CCO, it does not explain the temperature dependence of the diminishing Cu XMCD signal shown in Figure 4.6(a). For CCO thin films, epitaxial strain has been reported to enhance the alignment of the canted Cr moments with little effect on the Cu moments.[26] Canting in CCO, a manifestation of magnetic frustration among the Cr^{3+} moments, is characterized by a delicate balance of the exchange interactions between the magnetic cations. Small external perturbations such as strain or magnetic fields can easily affect this balance effectively tuning the configuration of the magnetic moments. Therefore, it is believed that the close proximity between ferrimagnetic Fe$_3$O$_4$ and the ultrathin CCO allows the magnetism of the Fe$_3$O$_4$ to modulate the alignment of the frustrated Cr moments above T_C in the absence of an ordered Cu lattice. Finally, because the Cu cations occupy the tetrahedral sites of the spinel crystal, the large proximity between the Cu cations and the absence of Cu-O-Cu bonds result in weak interactions. Additionally, because the magnetic Cu lattice is not frustrated and there is a small presence of non-magnetic $3d^{10}$ Cu^{1+}, Fe$_3$O$_4$ has little effect on the Cu alignment.
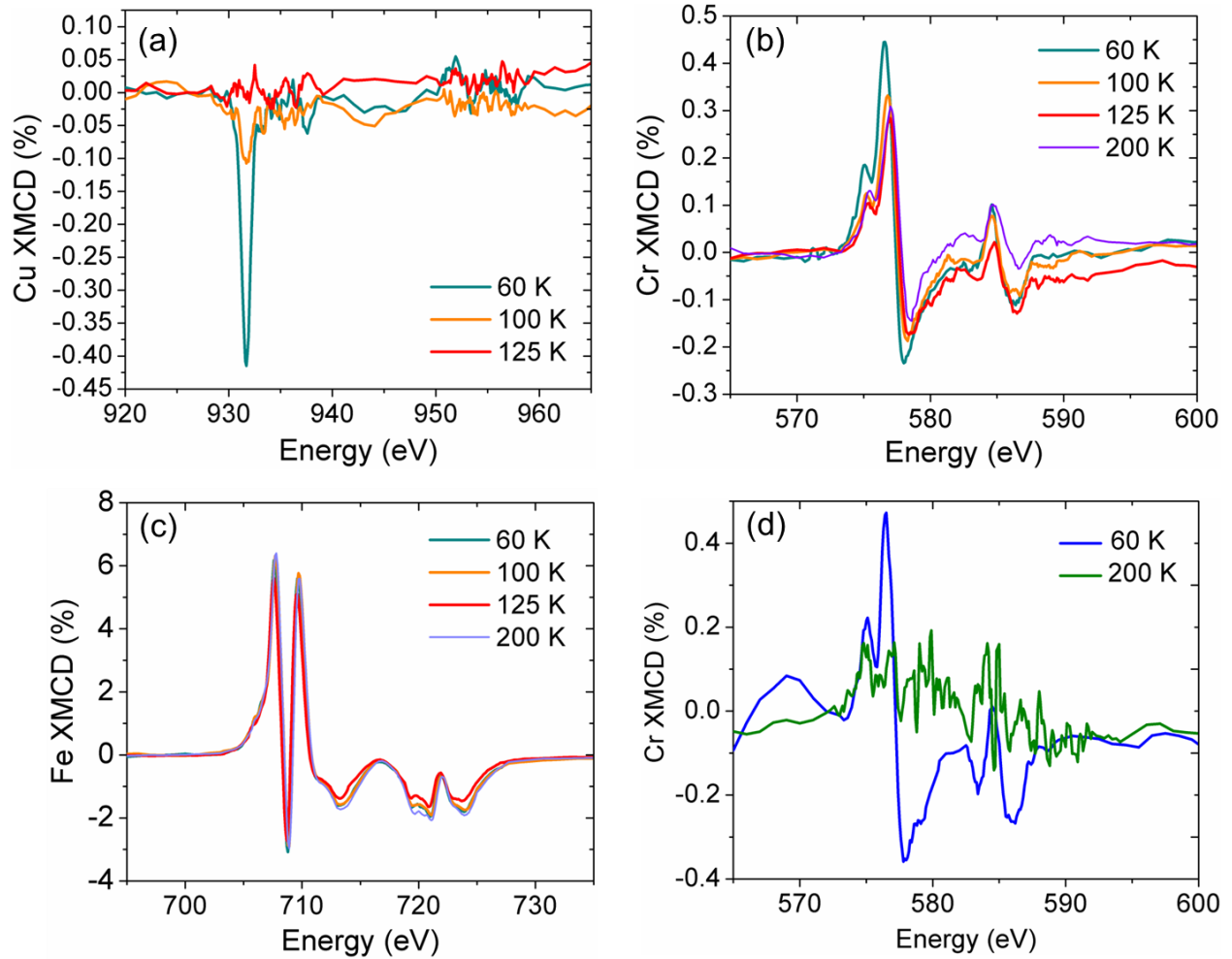
Figure 4.6. XMCD from a CCO/Fe$_3$O$_4$ bilayer at the $L_{2,3}$ edges of (a) Cu, (b) Cr, and (c) Fe. (d) Cr XMCD from a single CCO film. XMCD is measured with an applied field of ±1.5 T and defined as $\frac{RCP-LCP}{RCP+LCP} \times 100$, where RCP is the XA intensity with right circularly polarized light and LCP is the XA intensity with left circularly polarized light.

§4.5 Transport Studies

Having established independent switching, magnetotransport studies are performed to investigate the tunnel junction characteristics and the role of barrier thickness and temperature on junction behavior. The barrier thicknesses reported are 2.8-3.5 nm, 4.25 nm, and 6-8 nm. Nonlinear current-voltage (IV) curves indicative of tunneling are observed. Previous spin polarization experiments have shown that the conduction electrons in LSMO are positively spin polarized as the Fermi level passes through the majority spin band, whereas Fe$_3$O$_4$ is negatively spin polarized as its Fermi level passes through the minority spin band. [5] Thus, the negative JMR displayed by LSMO/CCO/Fe$_3$O$_4$ junctions in Figure 4.4(a) is due to the opposite spin polarization of the LSMO and Fe$_3$O$_4$ electrodes. In determining high and low resistance states,

the opposite spin polarization of the electrodes represents an anti-parallel electrode orientation which corresponds to a low resistance state, and a parallel electrode orientation which corresponds to a high resistance state. Therefore, the reported JMR values in this chapter are defined as $\frac{R_{AP}(H) - R_P(H=0)}{R_P(H=0)} \times 100$.

Despite the use of a tetragonal barrier and the challenges presented by the interfacial properties of an all-magnetic junction stack, it is remarkable that LSMO/CCO/Fe_3O_4 junctions exhibit the resistive switching shown in Figure 4.4(a). Here, the resistance data shows characteristic switching behavior that coincides with the magnetic switching of the electrodes. Junction resistance abruptly decreases with the magnetic switching of the LSMO electrode. Between -100 Oe to -500 Oe, the junction resistance gradually increases with minimal change in the magnetic moment. The increase in resistance reflects the sensitivity of transport measurements over bulk magnetometry and is thought to signal the magnetic switching of the CCO barrier. Near -1000 Oe, the simultaneous switching of the Fe_3O_4 electrode magnetization and distinct increase in junction resistance are observed. These switching characteristics disappear by 200 K, and the background JMR resembles that of the LSMO electrode (Fig. 4.4(b)).
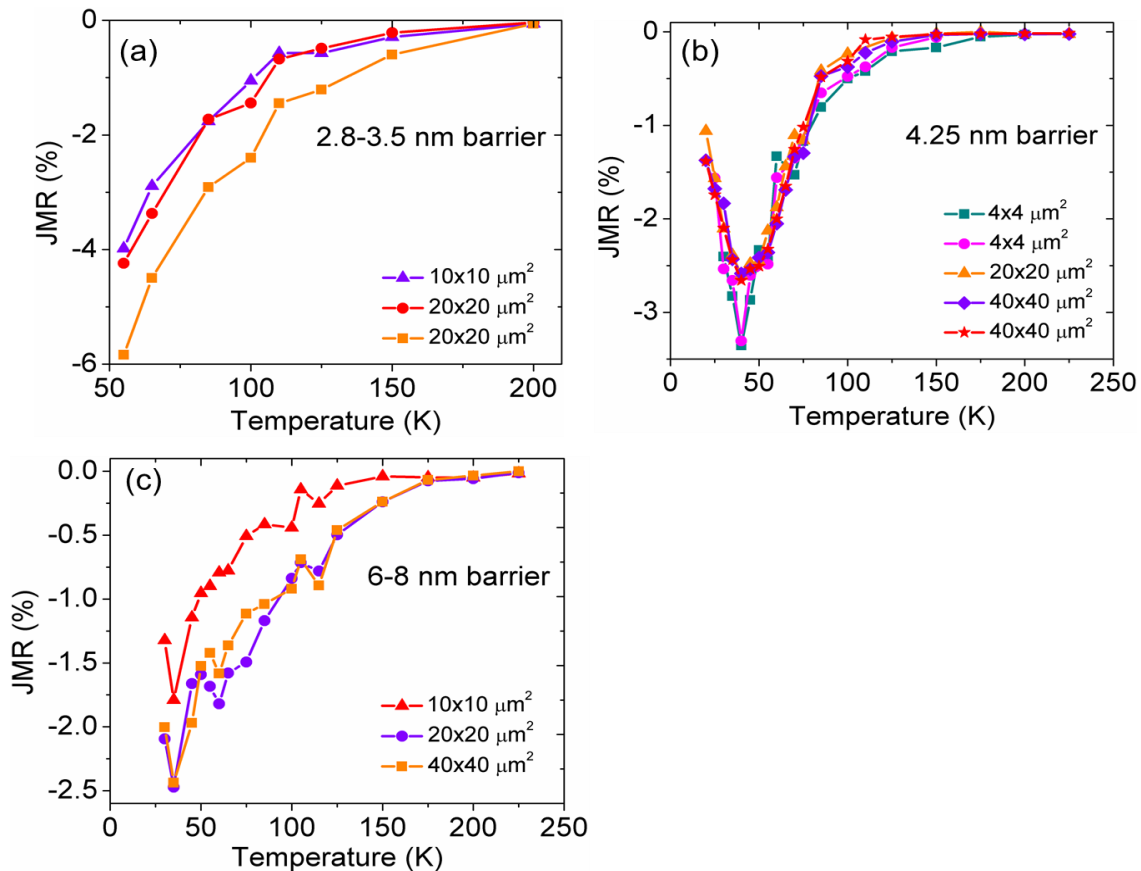
Figure 4.7. Temperature dependence of JMR for junctions with barrier thicknesses of (a) 2.8-3.5 nm, (b) 4.25 nm, and (c) 6-8 nm.

The temperature dependence of the JMR is examined to establish the resistance properties of the MTJ and each electrode. Figure 4.7 shows that for all junctions, there is negligible JMR at temperatures above 200 K. The diminished JMR is due to a decrease in spin polarization of the LSMO electrode and weakened coupling at the CCO/ Fe_3O_4 interface shown with XMCD.[9,27] In LSMO, the metal-insulator transition occurs near T_C. Therefore as the temperature approaches the T_C of LSMO, spin polarization decreases as it is proportional to magnetization.[9] Upon cooling, the JMR steadily increases until reaching a maximum in the vicinity of 50-60 K. With a subsequent cooling, the JMR decreases and junction resistance rapidly rises by two to three orders of magnitude over a small 30º change in temperature yielding resistances on the order of 1E7 Ω at 20 K as shown in Fig. 4.8. This increase is attributed to the suppressed Verwey transition of the Fe_3O_4 electrode which exhibits a similar low temperature behavior to the junction as shown in Figure 4.8(b).

The thickness of the CCO tunnel barrier affects the magnitude of the JMR. The thinnest barrier (2.8-3.5 nm) displays the largest JMR of -5.8%. The JMR decreases for a 4.25 nm barrier with a maximum JMR of -3.4%. Finally, the maximum JMR for the thickest barrier (6-8 nm) is about -2% with junction resistance an order of magnitude larger than junctions with thinner barriers for a significant portion of the temperature range measured. The dependence of JMR on barrier thickness is due to the exponential decay of the tunneling electron's wavefunction as it traverses the barrier. For barriers in which direct tunneling is unlikely or barriers in which conduction is due to inelastic processes, the dependence of JMR on barrier thickness is possibly due to the greater probability of spin information being lost due to increases in the hopping frequency and encounters with scattering centers in the barrier as electrons must travel a greater distance.
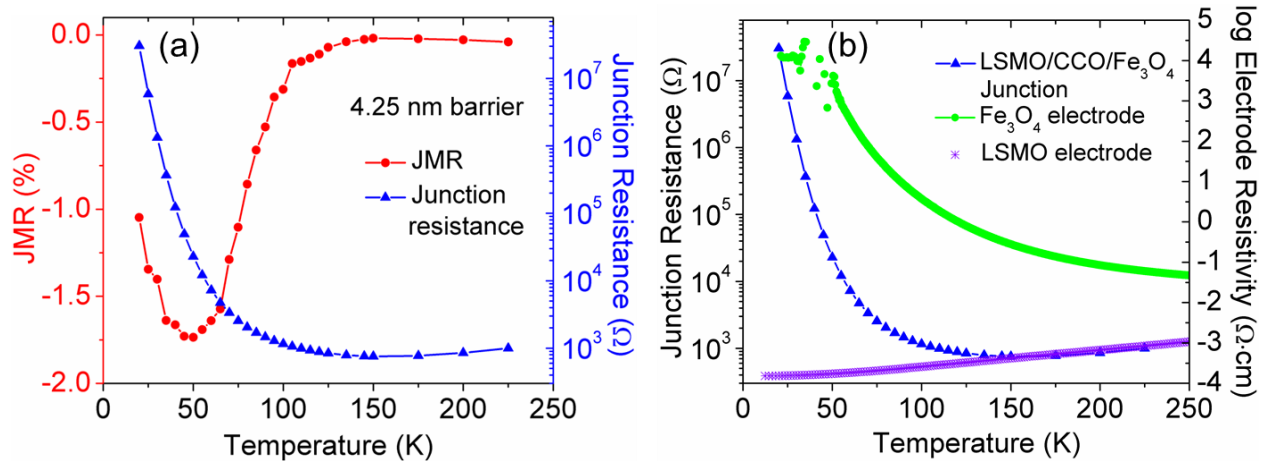
Figure 4.8. (a) Temperature dependence of JMR and junction resistance. (b) Comparison of resistance contributions from the Fe_3O_4 and LSMO electrodes to the total junction resistance.

Of particular interest is the bias dependence of JMR as oxide-based junctions and MTJs with magnetic barriers have revealed atypical properties compared to those of conventional F/I/F junctions. LSMO/CCO/Fe_3O_4 junctions are no different. In magnetotransport measurements, asymmetries arise from the use of dissimilar electrode materials resulting in

different barrier heights at the two CCO barrier interfaces.[28] As a result, electrons do not tunnel with the same probability from the LSMO electrode into the Fe_3O_4 electrode as they do from the Fe_3O_4 electrode into the LSMO electrode. Figure 4.9 highlights these asymmetries in bias dependence of the JMR for junctions with varying barrier thicknesses.

An open-ended question exists regarding the presence of the non-monotonic bimodal bias dependence of JMR that exists over a range of temperatures. For LSMO/CCO/Fe_3O_4 junctions, the maximum JMR occurs at a small finite, negative bias voltage. For these measurements, a positive bias voltage is taken with respect to the LSMO electrode. Therefore, the JMR maximum corresponds to positively biased Fe_3O_4 in which the electrons are tunneling into the LSMO electrode. For junctions with a 4.25 nm thick barrier, the onset of the bimodal bias dependence begins at temperatures ranging between 100 - 125 K. As temperature decreases, the bimodal dependence becomes increasingly sharp and persists until 40 K. For junctions with a thinner 2.8-3.5 nm barrier, the bimodal dependence is first observed at 125 K and becomes increasingly sharp at lower temperatures. With a thick 6-8 nm barrier, a majority of the junctions exhibit the onset of the bimodal dependence near 125 K which also becomes increasingly sharp at decreasing temperatures. However, large junction resistance increases noise in the IV curves making it difficult to resolve the bias dependence thereby limiting low temperature analysis.

The bias dependence of the conductance and the corresponding IV curves are used to identify the conduction mechanisms. Figure 4.10 displays these data sets for junctions of different barrier thicknesses and temperature. The conductance and IV characteristics for junctions with thinner barriers are similar and represented by data for a 4.25 nm thick barrier. For the temperature range in which the IV characteristics are nonlinear, barrier thickness exhibits its most notable effects. First, nonlinear IV curves for junctions with thick 6-8 nm barriers persist to temperatures higher than that of its thinner barrier counterparts. Rather than disappearing by 200 K as observed for junctions with thinner barriers, nonlinear IV curves in thick barrier junctions disappear by 250 K. In addition, current in junctions with thick barriers increases more significantly with increasing temperature suggesting a greater contribution from thermally-activated processes.

The total conductance, G, of the junctions can be described as the sum of direct tunneling, resonant tunneling, and inelastic hopping processes and is expressed as:

$$G(V) = G_0 + \sum_N G_{hop}^N \left(\frac{V}{T}\right)^{N - \frac{2}{N+1}}, \tag{4.4}$$

where N is the number of localized states, G_0 is the sum of elastic processes that include direct and resonant tunneling, and $\sum_N G_{hop}^N \left(\frac{V}{T}\right)^{N - \frac{2}{N+1}}$ is the sum of inelastic hopping through one or more localized states.[29] Of these terms, inelastic hopping is the only term dependent on the bias voltage. Conductance exhibits a power law dependence of the form $y = a + bV^c$ shown in Figure 4.11(a,b). Fits of the conductance data are used to extract the voltage exponent, $N - \frac{2}{N+1}$, represented by c, the hopping coefficient, G_{hop}^N, represented by b, and the sum of the elastic tunneling processes represented by the conductance in the limit of zero bias, $G_0 = a$.
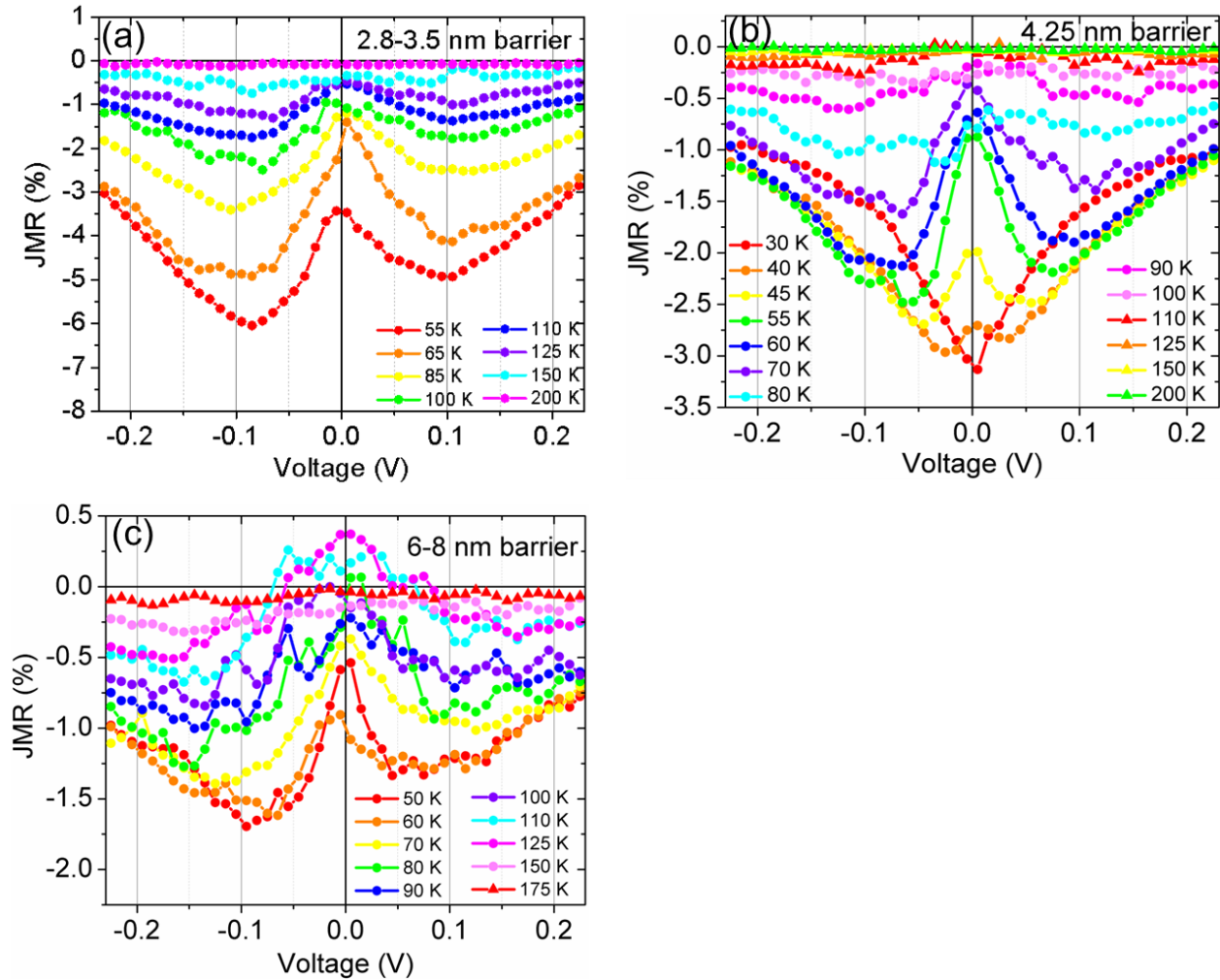
Figure 4.9. JMR bias dependence for junctions with barrier thicknesses of (a) 2.8-3.5 nm, (b) 4.25 nm, and (c) 6-8 nm. Positive bias is taken with respect to the LSMO electrode.

For the temperature region in which the IV curves are nonlinear, the voltage exponent, c, increases with decreasing temperature for all barrier thicknesses (Figure 4.11(c)). The voltage exponent is also larger for junctions with the 6-8 nm barrier. A larger voltage exponent indicates that an electron must make a larger number of hops to traverse the CCO tunnel barrier. In an inelastic process, the spin information is not preserved as an electron interacts with a localized moment site in the barrier and flips its spin. Therefore, with the increasing the number of hops it is surprising that JMR switching behavior is still observed.

The conductance of junctions with thinner barriers fits well to hopping through $N=2$ and $N=3$ localized states for all biases at temperatures below 75 K. However, at 75 K and above with biases greater than 0.15 V, the conductance slope is reduced as shown in Figure 4.10(a). For low biases, the conductance fits well to hopping through $N=2$ and $N=3$ localized states. For high biases, the conductance becomes linear and no longer fits well to a hopping model. For thicker barriers, the conductance fits well to hopping through $N=2$ and $N=3$ localized states for

all biases and temperatures up to 175 K. Above 175 K, a less pronounced reduction in the conductance slope occurs at high biases as shown in Figure 4.10(c).

To extract the individual contributions from each hopping channel, the fits of the data are revised to the form $G=G_o+bV^{4/3}+cV^{5/2}$. Using this form, the voltage coefficients are identified for the $N=2$ and $N=3$ inelastic hopping channels expressed by b and c, respectively. Furthermore, the changes in conductance at high bias limits the revised fit analysis to low bias regions where the dominant conduction mechanism is inelastic hopping. Figure 4.11(e&f) reveals that $N=3$ is the dominant hopping channel. Hopping also appears to be activated at 50 K as the contributions to the conductance from either hopping channel are very small at lower temperatures. Thinner barriers show that hopping through $N=2, 3$ localized states ascends to a peak between 80-110 K whereas the thickest barrier continues to gradually increase.

Next, the zero bias conductance probes the elastic contributions to total conductance. As can be seen in Fig. 4.10(a&c), the zero bias conductance increased with temperature. In this limit, the increase is most rapid at higher temperatures starting near 70 K for thinner barriers, and continues until a maximum is reached near 150 K. For thicker barriers, the increase begins near 125 K and a maximum is not attained in the temperature range measured. This signaled an increasing contribution from thermally-activated tunneling. Together the flattening of the conductance at high bias and the increased zero bias conductance indicate that when these characteristic conductance properties appear, the hopping channel is not as strong as bias-independent elastic tunneling.

At even higher temperatures, the conductance becomes flat and is no longer dependent on bias. The flattening of the conductance curves is concomitant with the appearance of linear IV curves and negligible JMR. At these temperatures, the CCO layer no longer provides a barrier for electron conduction. As a result, more current can pass through the barrier resulting in the loss of spin information. As temperatures continue to increase, the conductance begins to decrease as LSMO approaches its T_C.
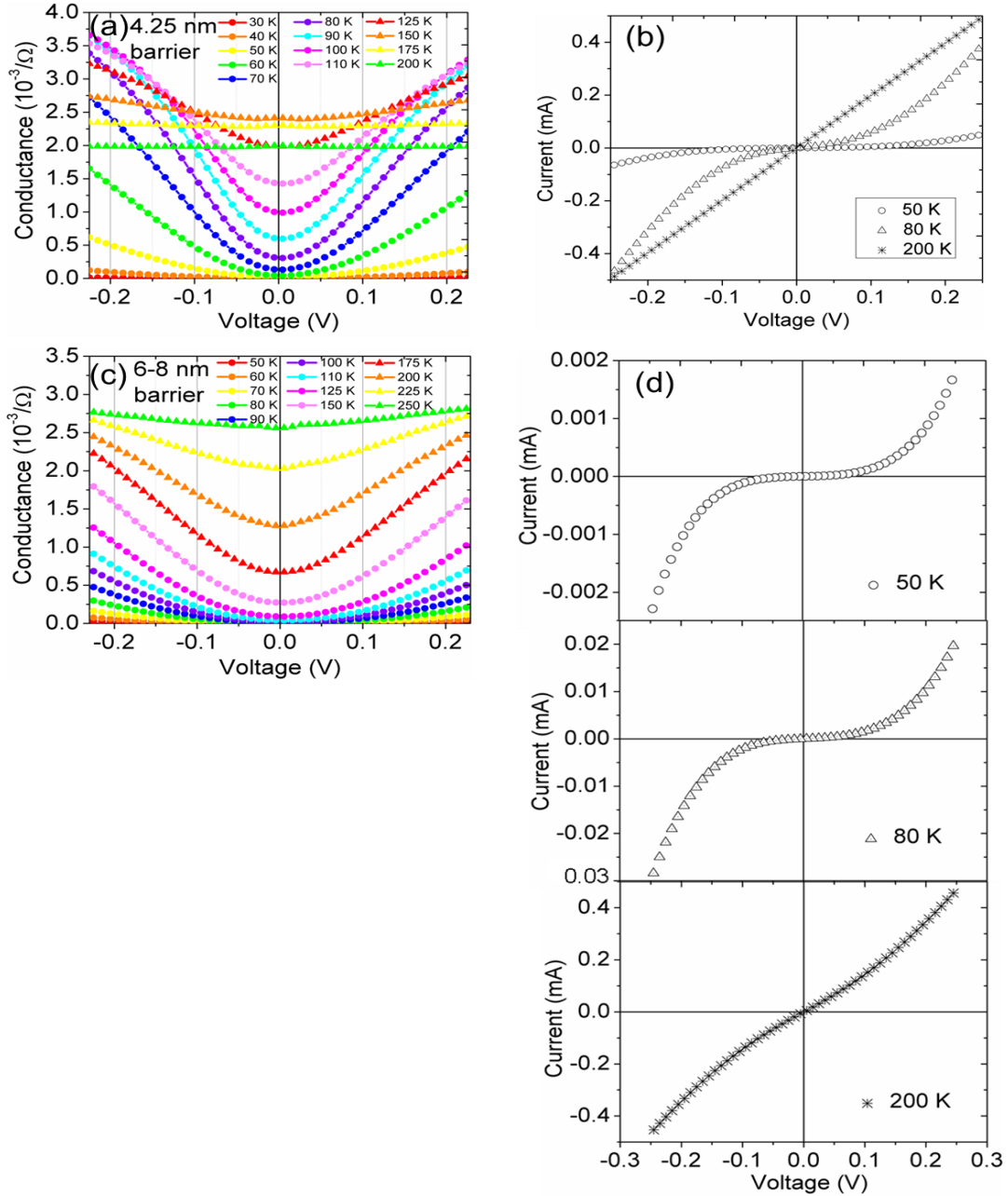
Figure 4.10. (a) Conductance dependence on bias voltage for junctions with a thinner barrier and (b) its corresponding IV curves as a function of temperature for a 4.25 nm thick barrier. The conductance and IV characteristics are similar for junctions with a 2.8-3.5 nm barrier and a 4.25 nm barrier. (c) Conductance dependence on bias voltage for junctions with a thick 6-8 nm barrier and (d) its corresponding IV curves as a function of temperature. Larger current increases in the IV characteristics for junctions with a thick barrier indicate a greater effect from temperature suggesting a larger contribution from thermally-activated transport processes.
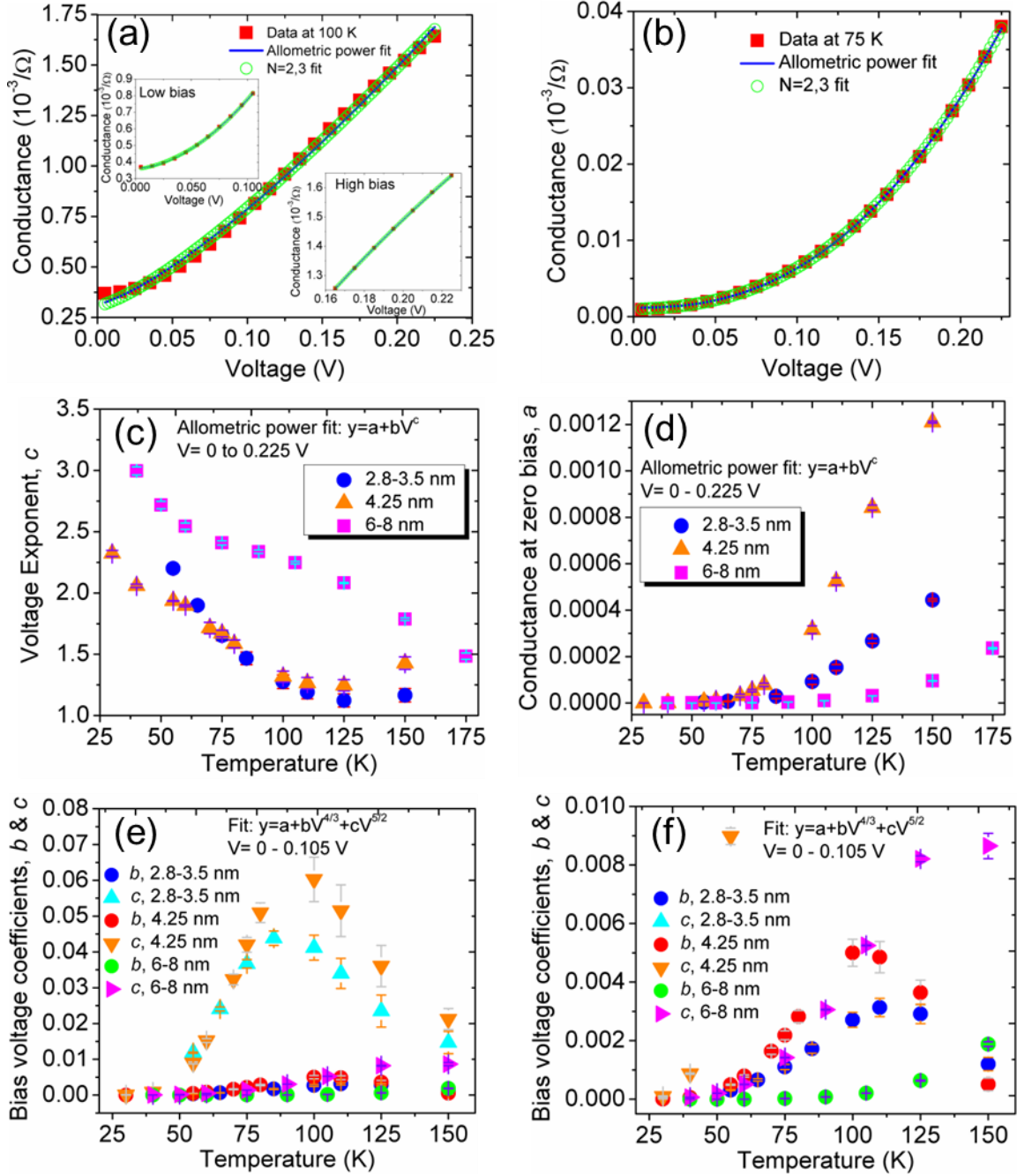
Figure 4.11. Conductance ($dG=dI/dV$) with fits as a function of bias voltage from 0 to 225 mV for junctions with a (a) 4.25 nm barrier with insets highlighting fits at low and high biases and (b) 6-8 nm barrier. The blue solid line is the best fit to the form $G=a+bV^c$. The open green circles are the best fit for the N=2,3 inelastic hopping channels expressed by the form $G=a+bV^{4/3}+cV^{5/2}$. (c) Voltage exponents determined by conductance fits are shown as a function of temperature for all barrier thicknesses. (d) Zero bias conductance as a function of temperature. (e) The detailed conductance fit $G=G_o+bV^{4/3}+cV^{5/2}$ is used to identify individual contributions from the N=2 and N=3 hopping channels represented by the voltage coefficients for each channel. The changes in conductance with bias indicate that N=2,3 inelastic hopping

64

fits better at low bias. As a result, the conductance fit range was lowered to 0 to 0.105 V. (f) Zoomed in to resolve the bias voltage coefficients for hopping terms with smaller coefficients.

§4.6 Discussion

The junction data indicates that the bimodal bias dependence of JMR typically exists between 50 - 125 K. In measurements with exceptionally low noise, the bimodal dependence is seen as low as 40 K. There are two active theories explaining the origin of the bimodal bias dependence of JMR. One attributes the bias dependence to the increased resistivity of the Fe_3O_4 electrode operating below its Verwey transition, and the other attributes it to the exchange splitting of the magnetic tunnel barrier.

The first theory is associated with the emergence of the 100-150 meV charge gap in Fe_3O_4 below its T_V.[11,12] The model proposed by Hu utilizes bias dependence studies to probe the size of the charge gap of the Fe_3O_4 electrode.[17] Assuming that the Fermi level of the Fe_3O_4, E_F^{Fe3O4}, lies in the middle of the charge gap, the application of a bias will shift the electrode conduction bands relative to one another. A peak in the JMR will occur when the Fermi level of LSMO, E_F^{LSMO}, is shifted out of the charge gap and into a spin polarized band with electronic states available for occupation. For the LSMO/CCO/Fe_3O_4 junctions, the maximum JMR occurs for positively biased Fe_3O_4. Under this condition, electrons are injected from the LSMO, through the CCO barrier, and into empty states in the minority spin band of Fe_3O_4. With regard to the relative orientation of the electrode Fermi levels, this is most likely to occur when $E_F^{LSMO} \sim E_F^{Fe3O4} + eV$ and E_F^{LSMO} sits above the Fe_3O_4 charge gap in an empty minority spin band. JMR also rises because of the higher degree of spin polarization expected from hopping into electronic states in a spin polarized band rather than unpolarized localized states in the charge gap. As JMR peaks occur at voltages under positive and negative bias, the width of the charge gap is on the order of 0.1 V which is consistent with studies of bulk Fe_3O_4.

This model is most applicable at the lowest temperatures in which the bimodal dependence is observed. At these temperatures, the spin polarization of LSMO is highest and CCO is ferrimagnetic capable of spin filtering. However at these temperatures, the junction resistance is overwhelmed by the resistance of the Fe_3O_4 electrode, and the decrease in JMR serves as an indicator of the increasingly insulating properties of Fe_3O_4 rather than the transport characteristics of the magnetic junction. Overall the total junction conductance is low and inelastic hopping not only occurs in the barrier but also in the Fe_3O_4 electrode. The increased resistivity is the result of the suppressed Verwey transition in Fe_3O_4 that creates a charge gap in the conduction band. As JMR peaks are present at positive and negative bias near ±0.05 V, the width of the charge gap is on the order of 0.1 V consistent with bulk studies of Fe_3O_4. For biases less than 0.05 V, the increased JMR is attributed to hopping through localized states near the Fermi level of Fe_3O_4. As the bias is increased, it opens up access to more electronic states for conduction. At biases above 0.05 V, the decreased JMR is attributed to the excitation of magnons with increasing bias which randomize and scatter tunneling electron spins.[9]

At temperatures above 50 K, the total junction resistance more accurately reflects the magnetic junction rather than its electrodes, and the JMR maximum shifts to a higher bias near

±0.1 V. Between 50 – 120 K, there is a small but gradual increase in the Fe_3O_4 resistivity. While the Verwey transition is suppressed, the gradual increase could be evidence of the heavily debated pseudogap above T_V. In the pseudogap, the electronic states are nearly localized with polaronic conduction.[30,31] Therefore, the small increase in resistivity represents the gradual localization of the pseudogap states. However, because the resistance of Fe_3O_4 no longer dominates the total junction resistance, the bimodal dependence cannot be explained entirely by the electronic band structure of Fe_3O_4. Furthermore, it also cannot explain the shifting of the JMR maxima to higher bias since the size of the charge gap should not increase at higher temperatures.

Another possible explanation for the bimodal bias dependence is the spin filtering behavior of the CCO barrier. Spin filtering relies on the spin-split conduction band in the magnetic tunnel barrier which produces spin-up and spin-down sublevels with different barrier heights. Spin-up electrons see a lower barrier height than spin-down electrons. When the applied bias is sufficient for spin-up electrons to overcome the barrier height of the spin-up sublevel, spin-up electrons are preferentially transmitted through the barrier. Thus, at low bias, conduction occurs by hopping through localized states resulting in increasing JMR. Once the bias is large enough to overcome the barrier height of the spin-up sublevel, spin polarized conduction is preserved, and manifested in JMR maxima occurring at higher biases. As the bias is increased further, JMR begins to decrease due to the excitation of magnons. At a certain bias voltage, the bias is also large enough to overcome the barrier height of the spin-down electrons reducing the overall spin filtering efficiency of the barrier contributing to decreasing JMR.

However, spin filtering cannot account for the bimodal dependence observed in LSMO-Fe_3O_4-based junctions with a nominally nonmagnetic Mg_2TiO_4 (MTO) insulating barrier.[13] The cations in MTO have full valence shell configurations making it difficult to induce ferrimagnetism through proximity effects at the Fe_3O_4 interface. It is possible that interdiffusion at the MTO/Fe_3O_4 interface could form an alternative magnetic phase capable of spin filtering, but further exploration is required. For the reasons presented in this section, the origin of the bimodal dependence cannot be adequately explained from the perspective of one model. Instead, the findings presented in this chapter suggest possible contributions from both the low temperature charge gap in Fe_3O_4 and spin filtering of the barrier.

§4.7 Conclusions

In summary, the JMR up to -6% is reported for LSMO/CCO/Fe_3O_4 magnetic tunnel junctions. These junctions demonstrate distinct switching of the electrodes and a bimodal bias dependence of JMR. In probing the switching properties, XMCD identifies evidence of a Fe_3O_4 proximity-induced magnetism in the Cr at the exchange coupled CCO barrier-Fe_3O_4 electrode interface. In performing the bias dependence studies and reviews of the bimodal dependence of JMR, the origin of the bimodal bias dependence of JMR is thought to have contributions from both the charge gap of the Fe_3O_4 and spin filtering from the magnetic CCO barrier.

This work is comprised of experiments of differing themes that demonstrate the range of properties and phenomena possible in spinel-structure oxides. This work begins by examining the enhanced magnetization discovered in the first synthesis of $CuCr_2O_4$ thin films. $CuCr_2O_4$ is a canted ferrimagnet with strong competition between its exchange interactions. This results in a delicate balance that can be manipulated with a small external perturbation. One form of an external perturbation is heteroepitaxy. In single $CuCr_2O_4$ films, it is believed that the use of substrate-induced heteroepitaxy is sufficient for inducing greater collinear order among the canted Cr moments. When $CuCr_2O_4$ is used as a tunnel barrier in LSMO-Fe_3O_4-based magnetic tunnel junctions, the Cr moments display ferromagnetic alignment to temperatures well above their bulk T_C. In this case, the proximity of Fe_3O_4 represents another external perturbation capable of modifying the balance of exchange interactions.

Transport studies of heterostructures with a spinel oxide component reveal unconventional transport properties. With a $CuCr_2O_4$ tunnel barrier, the remarkable observation of magnetic and resistive switching with JMR up to -6% is noted. Furthermore, JMR exhibits a bimodal bias dependence which is attributed to contributions from the Fe_3O_4 electrode and the magnetic $CuCr_2O_4$ tunnel barrier. The high T_Cs of spinel ferrites also make them viable candidates for use in junction architectures with room temperature functionality. Preliminary structural and magnetic studies provide a foundation for the expansion of future work in this area.

Fabrication of Fe_3O_4/$CuCr_2O_4$/$La_{0.67}Sr_{0.33}MnO_3$ Trilayer Junctions

This appendix describes the processing techniques used for fabricating arrays of micron-sized magnetic junction devices in the Marvell Nanofabrication Laboratory at the University of California, Berkeley. An overview of the process presented in Figure A.1 depicts the sample appearance at the completion of each major process step. The final structure is shown in step 14. A pre-fabrication background on photoresist selection and sample preparation is presented followed by an in-depth description of each process step including detailed schematics, recommendations, and tips to remedy commonly encountered issues.

The fabrication process utilizes photolithography with four different mask patterns, two metal depositions, a SiO_2 deposition, and two liftoffs. A chrome mask contains all four mask patterns. Masks 1 and 2 are designed to be negative masks and incorporate an image reversal step. Masks 3 and 4 are designed to be positive masks. The first mask defines the bottom electrodes. The second mask defines the junctions ranging in size from 40 x 40 μm^2 to 4 x 4 μm^2. The third mask creates a window in the SiO_2 to open up the bottom electrode for subsequent contact pad patterning. The fourth and final mask defines all contact pads.

Photoresist Selection

Clariant AZ5214-E photoresist is used. AZ5214-E is a positive resist with image reversal capabilities that allow it to be used in both positive and negative tones. For positive resists, only the portions of resist exposed to light are soluble in developer. For negative resists, the portions of resist exposed to light are *in*soluble in developer. Positive resists are typically capable of generating smaller features with higher resolution which is important to the scaling of junction size. However, negative resists produce negative sidewalls which are better suited for liftoff. With image reversal, the properties of exposed photoresist are reversed such that soluble regions become insoluble in developer, and insoluble regions become soluble in developer. Thus, the use of a positive resist with image reversal combines higher resolution and negative side walls conducive to liftoff.

Sample Mounting and Removal

The experimental setup for each process step varies based on machine specifications.

For each photolithography step, 6 x 6 mm^2 samples are mounted on approximately 1 inch^2 Si handle wafers. Handle wafers are placed on a hot plate heated to 125 ℃ which is just above the melting temperature of the adhesion material Crystalbond 509 (T_m = 121 ℃). Crystalbond is uniformly applied to the handle wafer over an area close to the sample size. The sample is then gently placed on the melted Crystalbond as flat as possible, and immediately transferred from the hot plate to a cooling plate.

To remove the sample from its handle wafer, place on a hot plate pre-heated to 125 ºC. Using tweezers, gently slide the sample off the handle wafer and let cool before placing the sample on a surface. Minimize the time that the sample is exposed to the hot plate. Transfer the handle wafer to a cooling plate until cool.

Notes

1) Crystalbond is removable with acetone.

2) Do not get Crystalbond on the sample surface.

    a) If Crystalbond gets on the sample surface *before* patterning, remove the sample from its handle wafer and immerse in a beaker filled with acetone. When Crystalbond has been removed, remove sample from beaker, rinse with isopropanol and dry with an N_2 air gun.

    b) If Crystalbond gets on the sample surface *after* patterning, soaking in acetone will remove the Crystalbond and the AZ5214-E resist. Decide if this is acceptable or not.

3) Periodic cleaning of handle wafers is recommended for best results during sample mounting.

For electron beam (e-beam) evaporations, ion milling, and SiO_2 depositions, the equipment setup requires that samples are mounted on a 4" Si dummy wafer using double-sided Kapton tape. Wafers are designated for each tool to prevent cross contamination. SiO_2 depositions are an exception as each deposition requires that samples are mounted on a new 4" Si wafer.

To remove samples from the dummy wafer, use a razor blade to remove the sample from the Kapton tape.
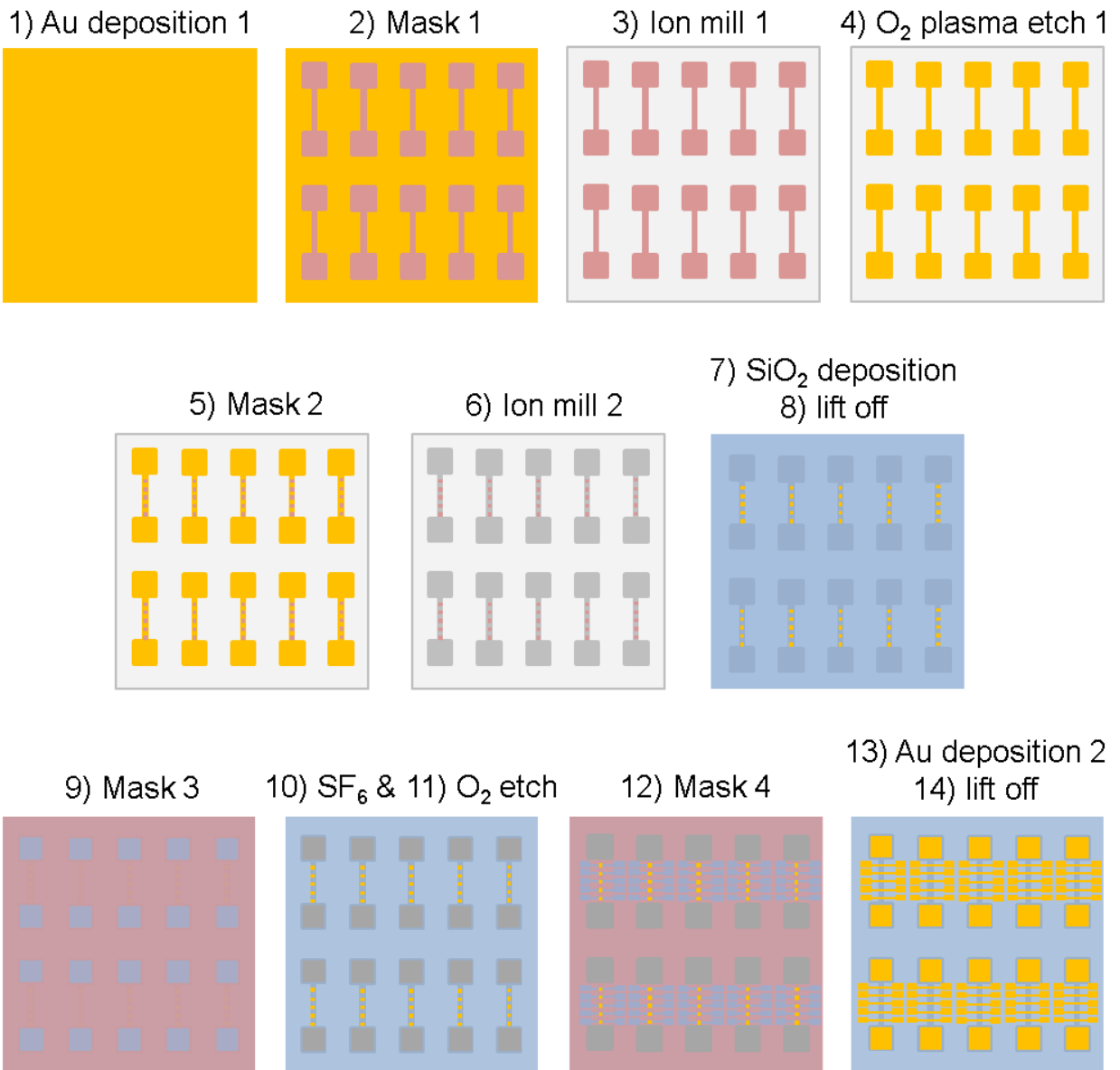
Figure A.1. Overview of the magnetic tunnel junction fabrication process.

Overview of Processing Steps

1) Deposit a 5 nm Cr adhesion layer followed by 100 nm of Au using e-beam evaporation.
2) Mask 1: first photolithography step defines and forms the bottom electrodes.
    a. Spin coat AZ5214-E photoresist at 4000 rpm for 30 seconds.
    b. Soft bake on a hot plate at 95 ºC for 45 seconds.
    c. Align sample to mask pattern 1 using contact mask aligner, then transfer pattern by exposing to ultraviolet light ($\lambda_{i\text{-}line}$ = 365 nm).
    d. Reversal bake on hot plate at 125 ºC for 45 seconds (image reversal).
    e. Remove mask and flood expose (image reversal).
    f. Develop pattern in AZ400K developer diluted 1:3 AZ400K:deionized (DI) H_2O and gently agitate until resist is visibly removed (~30 seconds).
    g. Immerse and gently agitate sample in DI water bath for ~30 seconds.
    h. Dry with N_2 air gun.
    i. Inspect quality of patterned sample using optical microscope.
3) Ion mill until the substrate. Regions protected by resist remain.
4) Remove the protective resist above the bottom electrodes with an O_2 plasma etch.
5) Mask 2: second photolithography step defines and forms junction pillars.
    a. Repeat mask 1 process steps a-i using mask pattern 2.
6) Ion mill just past tunnel barrier.
    a. This is not followed by an O_2 etch.
7) Deposit SiO_2 using room temperature ECR PECVD.
8) Lift off resist and SiO_2 above junction pillars by soaking in acetone.
9) Mask 3: third photolithography step defines the areas to remove SiO_2 in order to form contacts to the bottom electrode in subsequent contact pad patterning.
    a. Repeat mask 1 process steps using mask 3 and eliminating steps d & e.
    b. This step does not require an image reversal.
10) Remove SiO_2 with SF_6 plasma etch.
11) Remove remaining resist with O_2 plasma etch.
12) Mask 4: fourth lithography step defines contact pads to bottom and top electrodes.
    a. Repeat mask 1 process steps using mask 4 and eliminating steps d & e.
    b. This step does not require an image reversal.
    c. Inspect and record good junctions, bad junctions, scratches, etc.
13) Deposit 5 nm of Cr followed by 100 nm of Au using e-beam evaporation.
14) Lift off Cr/Au and underlying resist by soaking in acetone.

1) Au deposition 1
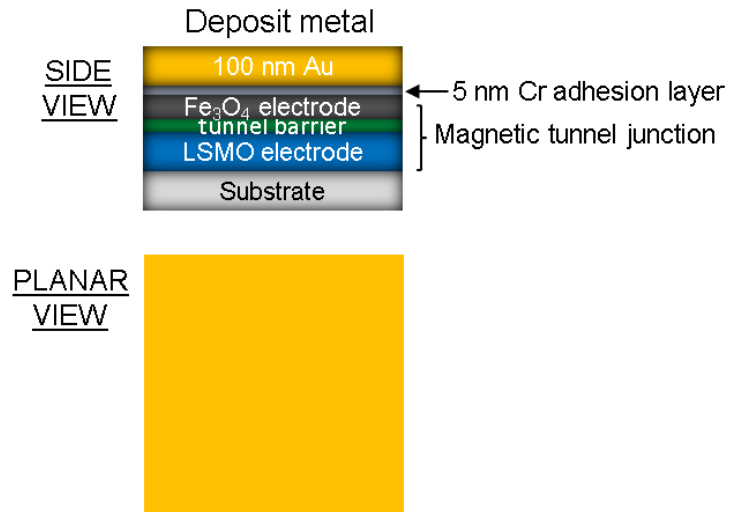
Figure A.2. Cr/Au deposited on a MTJ heterostructure using e-beam evaporation.

E-beam evaporation is used to deposit a 5 nm Cr adhesion layer followed by 100 nm of Au in order to protect the surface of the heterostructure and ensure ohmic contact between the electrodes and leads. The metallic layers are sequentially deposited without breaking vacuum to prevent oxidation of the Cr layer. At the end of the deposition, samples are removed from the dummy wafer.

Notes

1) Au is inert and will not oxidize when exposed to atmosphere.

2) Au is soft and scratches easily. Use care when removing samples from dummy wafer to prevent deep scratches.

3) To further improve adhesion, an intermediate layer of Ti can be inserted between the Cr and Au. The drawback of the Ti layer is the increased ion milling time due to a seemingly lower Ti mill rate.

2) Mask 1

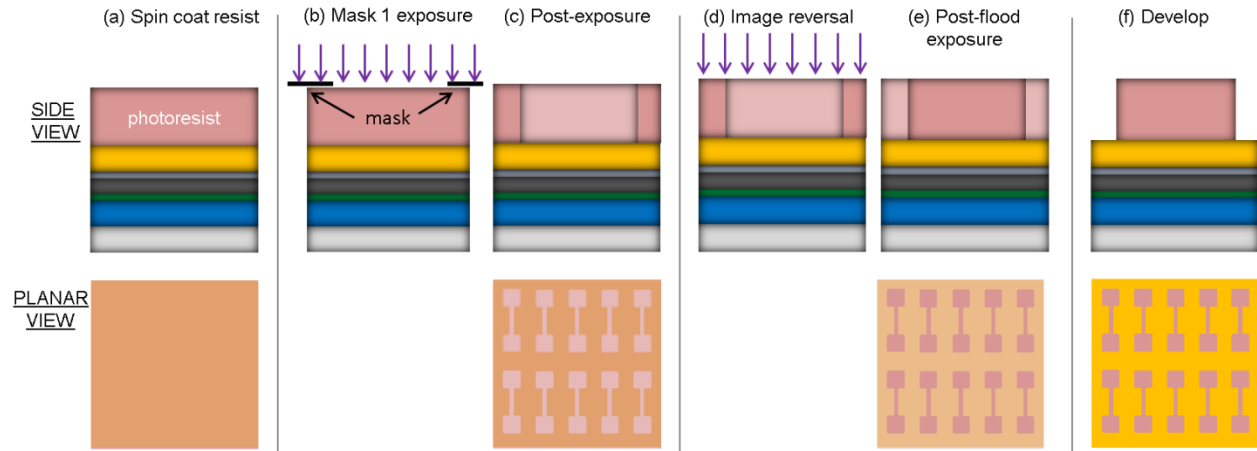**Figure A.3**. (a) Spin coat AZ5214-E photoresist followed by soft bake. (b) Sample is aligned and resist is exposed to mask 1. (c) Contrast in resist properties are highlighted after exposure. (d) Sample is image reversal baked and followed by a flood exposure (mask is removed) reversing the resist properties. (e) Contrast in resist properties after flood exposure. (f) Resist is developed.

The first photolithography step uses mask 1 to define and form the bottom electrodes.

Resist Application

AZ5214-E resist is spin-coated on the sample at 4000 rpm for 30 seconds yielding a thickness of ~1.4 μm. Next, the sample is soft-baked on a hot plate at 95 ℃ for 45 seconds to evaporate the resist solvents.

Exposure and Image Reversal

The sample is aligned and exposed to mask pattern 1 using a contact mask aligner (Fig. A.3(b,c)). The exposure time is calculated based on the required energy and the measured intensity of the UV light source ($\lambda_{\text{i-line}} = 365$ nm). It is recommended that the lamp intensity is checked at least once in a seven day period. After exposure, an image reversal bake follows at 125 ℃ for 45 seconds activating the crosslinking agent. Combined with the photoactive compound of the resist, the exposed resist becomes insoluble in developer. The mask is removed and the sample is flood exposed to reverse the properties of the unexposed resist (Figure A.3(d,e)).

Develop

The pattern is developed by immersing the sample in diluted 1:3 AZ400K developer and gently agitating for approximately 35 seconds or until the resist is visibly removed. The sample is immediately immersed in DI water for approximately 30 seconds. After 30 seconds, the sample is removed and dried with an N_2 air gun. The samples are inspected with an optical microscope to ensure proper pattern transfer and to assess the feature quality. Overdeveloping can remove

smaller features. Underdeveloping results in incomplete resist removal affecting uniformity in subsequent mill steps. Finally, samples are removed from handle wafers.

Notes

If problems are encountered during patterning, the following may be of help assuming chemical compatibility. For any of these three scenarios, first remove samples from the handle wafer.

1. For problems identified after spin coating resist (pre- or post-soft bake), resist is easily removed by soaking the sample in acetone. Once the resist is removed, the sample is rinsed with isopropanol and dried with an N_2 air gun.

2. For problems identified post-exposure, resist is removed with acetone but with increased difficulty. Heating the acetone is a more aggressive resist removal method. Ultrasonication will help but should be used sparingly as it can easily cause the Au to flake off. As an alternative, soaking the sample for ~30 minutes in AZ400T stripper heated to 80 ℃ followed by a DI water rinse and N_2 dry should easily remove the resist.

3. For post–image reversal problems, crosslinked regions are difficult to remove with acetone alone. Soak samples in AZ400T stripper heated to 80 ℃ for ~30 minutes followed by a DI water rinse and N_2 dry.
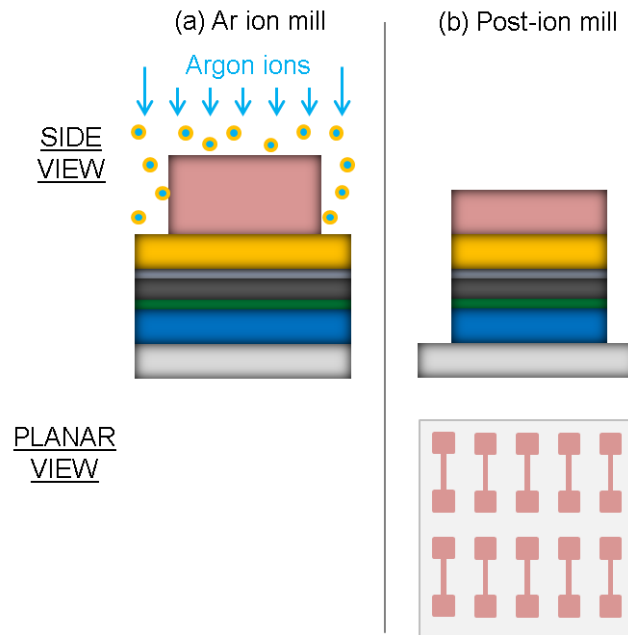
3) Ion mill 1

Figure A.4. (a) Ar ion beam sputters away material unprotected by resist until the substrate is reached. (b) Post-ion mill structure.

Argon ion beam milling sputters away material unprotected by resist. In this dry etch step, ion milling forms ten distinct and separate dog bone-shaped bottom electrodes. This is accomplished by milling through the Cr/Au layers, top electrode, tunnel barrier, and bottom electrode until the substrate is reached. For heterostructures grown on STO substrates, the STO will appear clear when the substrate has been reached. At the end of the etch, samples are removed from dummy wafer.

Notes

1) This step establishes subsequent mill rates and times serving as a calibration run with known layer thicknesses. Therefore, it is important to document milling times.

2) Undermilling leads to continuous coverage of the heterostructure materials preventing the formation of distinct and isolated electrodes. For STO substrates, overmilling the substrate can result in lower substrate resistance and conductive STO.

4) O_2 plasma etch (descum) 1
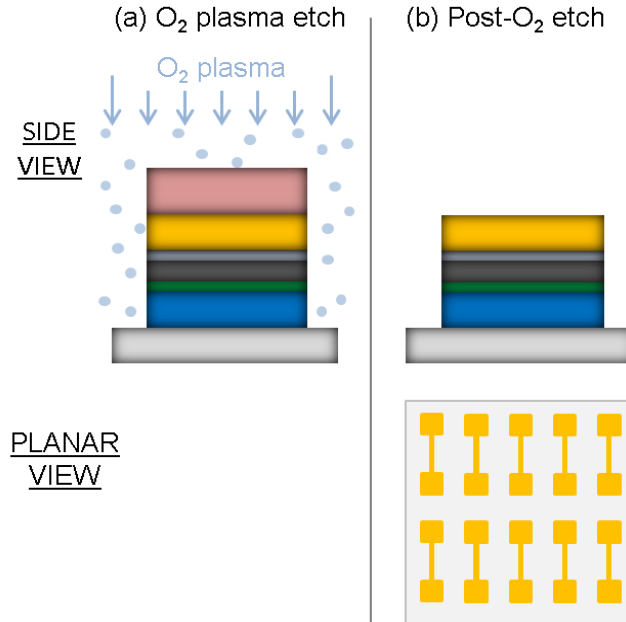
Figure A.5. (a) Descumb using an O_2 plasma etch. (b) O_2 plasma etch removes protective resist layer covering the heterostructure stack.

Oxygen plasma etching removes the remaining resist used to form the mask 1 feature. This is performed with a parallel plate etch system that allows for the selection of gas, gas pressure, and power. The sample chamber is pre-cleaned by wiping with acetone followed by pumping down to a base pressure less than 10 mTorr. Once this base pressure is achieved, a 20 minute O_2 clean begins. After cleaning, the chamber is vented, the samples are loaded, the chamber is pumped down to a base pressure less than 10 mTorr followed by the O_2 plasma etch.

5) & 6) Mask 2 and ion mill 2
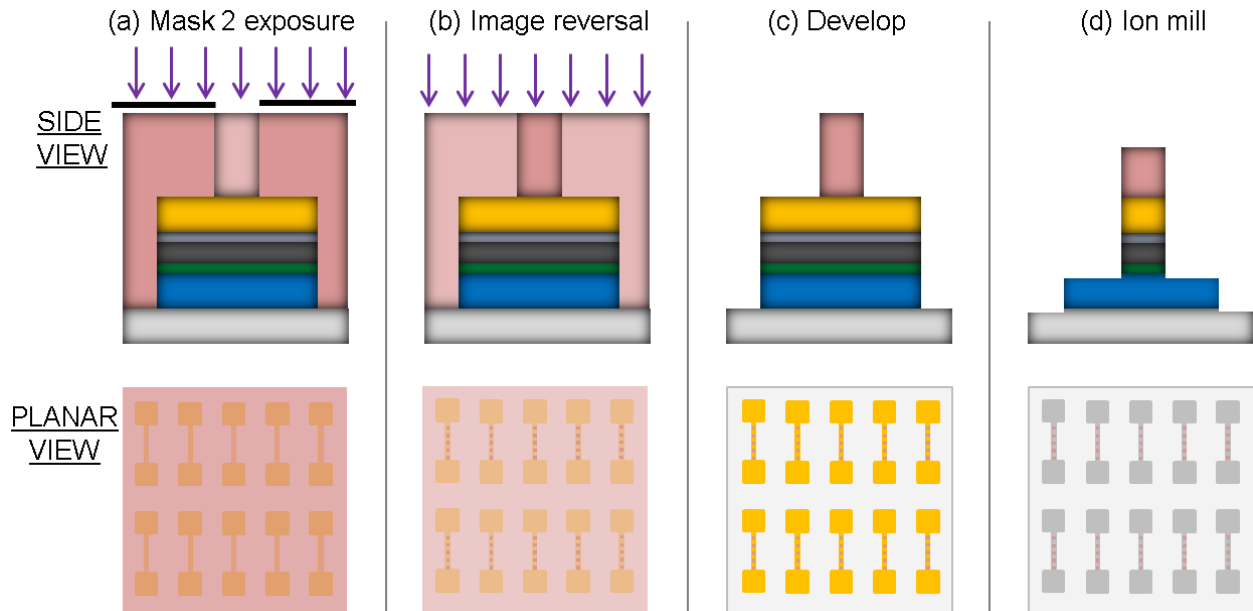
Figure A.6. (a) Sample is aligned and resist is exposed to mask 2. (b) Sample is reversal baked then flood exposed (mask was removed) reversing the resist properties. (c) Resist is developed. Remaining resist covers only the junction pillar. (d) Ion mill to the bottom electrode, just past tunnel barrier.

The second photolithography step uses mask 2 to define and form the junction pillars. The procedure for patterning the junction pillars is identical to mask 1. However, ion milling occurs only until the bottom electrode just past the barrier as shown in Figure A.6(d). Without chemical analysis of the ejected ions, the milling time is established based on mill rates calculated during the first ion mill step and/or checking the magnetic properties of the sample with a magnetometer. There is no subsequent O_2 plasma descum step.

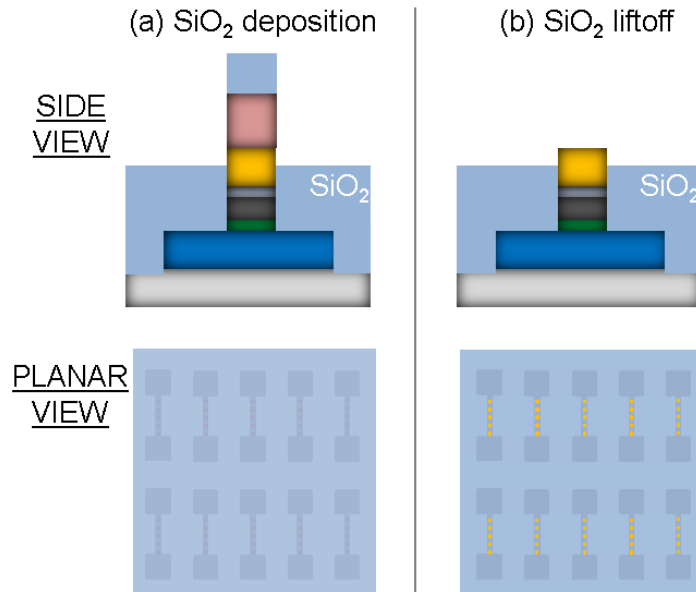## 7) & 8) SiO$_2$ deposition and liftoff

Figure A.7. (a) SiO$_2$ is deposited using room temperature ECR PECVD. (b) SiO$_2$ and protective resist above the pillars are lifted off with an acetone soak.

A conformal layer of SiO$_2$ is deposited using room temperature electron cyclotron resonance plasma-enhanced chemical vapor deposition (ECR PECVD). The SiO$_2$ must be thick enough so the sides of the junctions are covered to prevent electrical shorts between the top Au contact and the bottom electrode. When Au is deposited for contacts in step 13, it should only touch the top of the Au-capped junction pillars. SiO$_2$ thicknesses that exceed the height of the Au-capped junction pillars result in unsuccessful liftoffs. At the completion of each deposition, samples are removed from the 4" Si wafer, inspected, and soaked in acetone-filled vials for liftoff.

Notes

1) Prior to the SiO$_2$ deposition, write on the wafer with a Sharpie marker. After the deposition, cleave the wafer. Select a chip with writing and soak in an acetone-filled vial along with the samples. When the ink is gone, it is one indication that liftoff is complete. However, because the samples and the Si dummy wafer are subjected to different levels of processing, use a microscope to check the Au-capped junction pillars. They will be shiny if liftoff is complete.

2) This liftoff step is often challenging as processing exposes the sample to elevated temperatures causing baked-on resist. In particular, these steps include the SiO$_2$ deposition and/or long ion milling sessions. Soaks have ranged from one day up to several weeks. Ultrasonic agitation may be employed but often causes the SiO$_2$ to flake off resulting in electrical shorts.

9) Mask 3
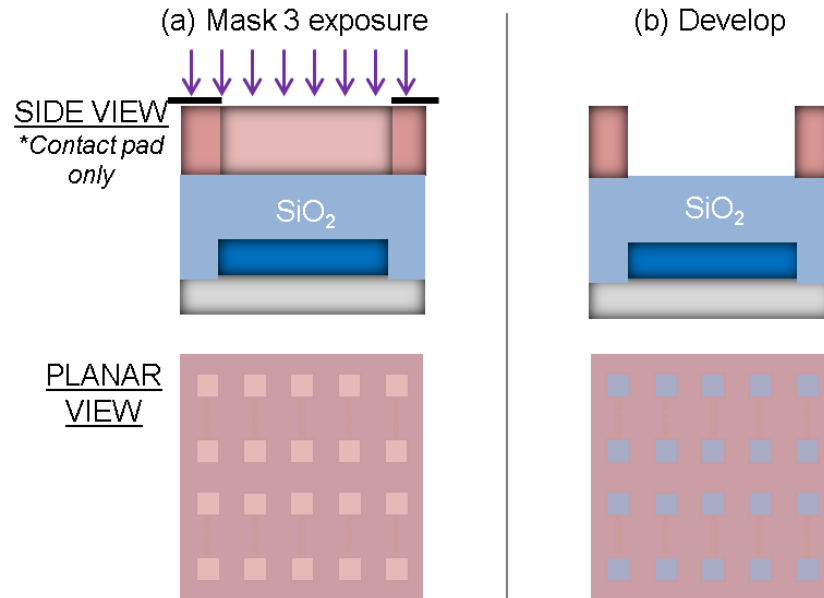
Figure A.8. (a) Sample is aligned and exposed to mask 3. (b) Final pattern creates a window to the SiO_2 covering the contact pads.

The third photolithography step uses mask pattern 3 to define the contact pad area for the bottom electrodes to create a window in the underlying SiO_2. This mask uses the positive tone of AZ5214-E (no image reversal). The patterning procedure uses a modified version of the mask 1 process steps eliminating steps d & e.

10) & 11) SF$_6$ and O$_2$ etches
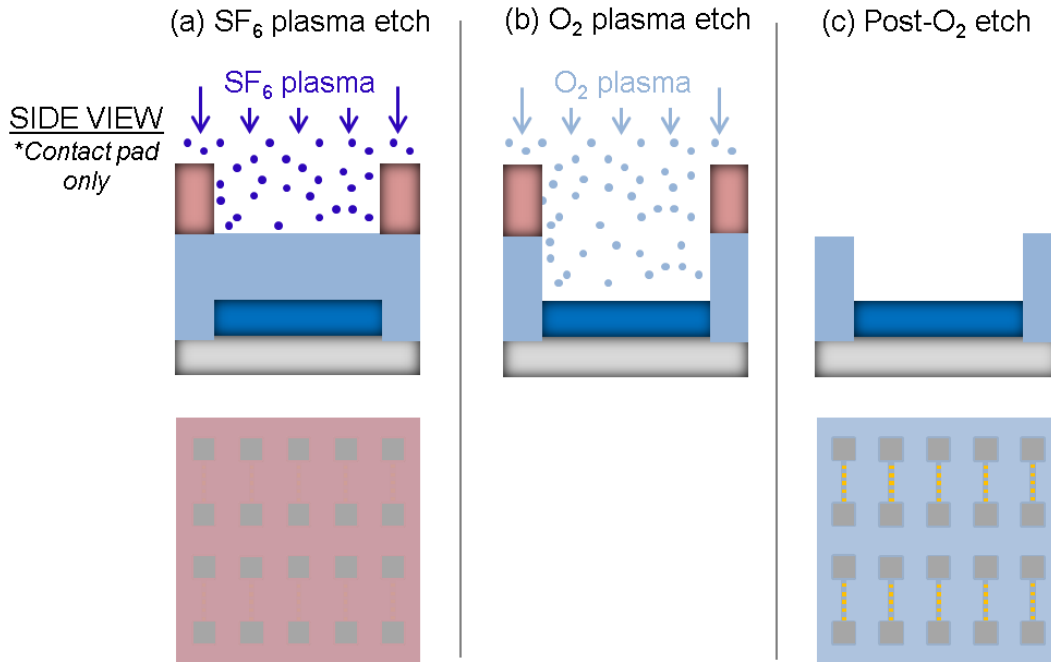
Figure A.9. (a) An SF$_6$ plasma etch removes the exposed SiO$_2$ creating an opening to the bottom electrode. (b) An O$_2$ plasma etch removes the protective resist covering the remainder of the sample exposing the underlying SiO$_2$. (c) Post-O$_2$ etch, final mask 3 structure.

To open up the SiO$_2$ above the bottom electrode, the sample is exposed to a series of etches. After pre-cleaning the sample chamber, the samples are loaded including a piece of the cleaved silicon wafer from steps 7 & 8. First a SF$_6$ plasma etch selectively removes the exposed SiO$_2$ creating an opening to the bottom electrode. The chamber is then vented (requires multiple vent-purge steps as SF$_6$ is toxic) and the Si wafer is inspected to ensure that the SiO$_2$ is completely removed. The wafer is then reloaded into the sample chamber for the subsequent O$_2$ descum step removing the remaining resist.

12) Mask 4

(a) Mask 4 exposure

Top electrode contact pad (horizontal bar)

Bottom electrode contact pad

(b) Develop

Top electrode contact pad

Bottom electrode contact pad

SIDE VIEW

PLANAR VIEW
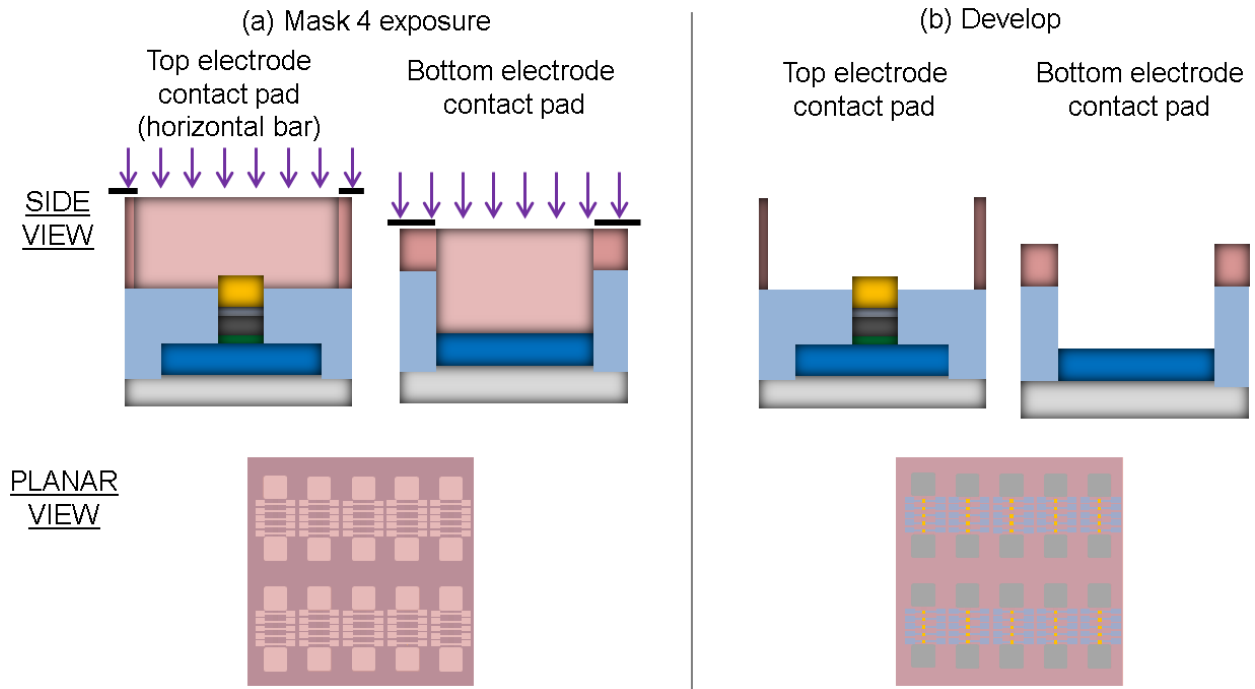
Figure A.10. (a) Sample is aligned and exposed to Mask 4. The cross-sections shown are along the horizontal bar contacting the top electrode and the big contact pads contacting the bottom electrode. (b) Patterned sample.

The fourth photolithography step uses mask 4 to define the contact pads for both the top and bottom electrodes. The mask pattern uses the positive tone of the AZ5214-E resist (no image reversal). The patterning procedure uses a modified version of the mask 1 process steps eliminating steps d & e. At this point, create a record of good junctions, missing junctions, scratches, possible shorts, etc.

13) & 14) Au deposition 2 and liftoff

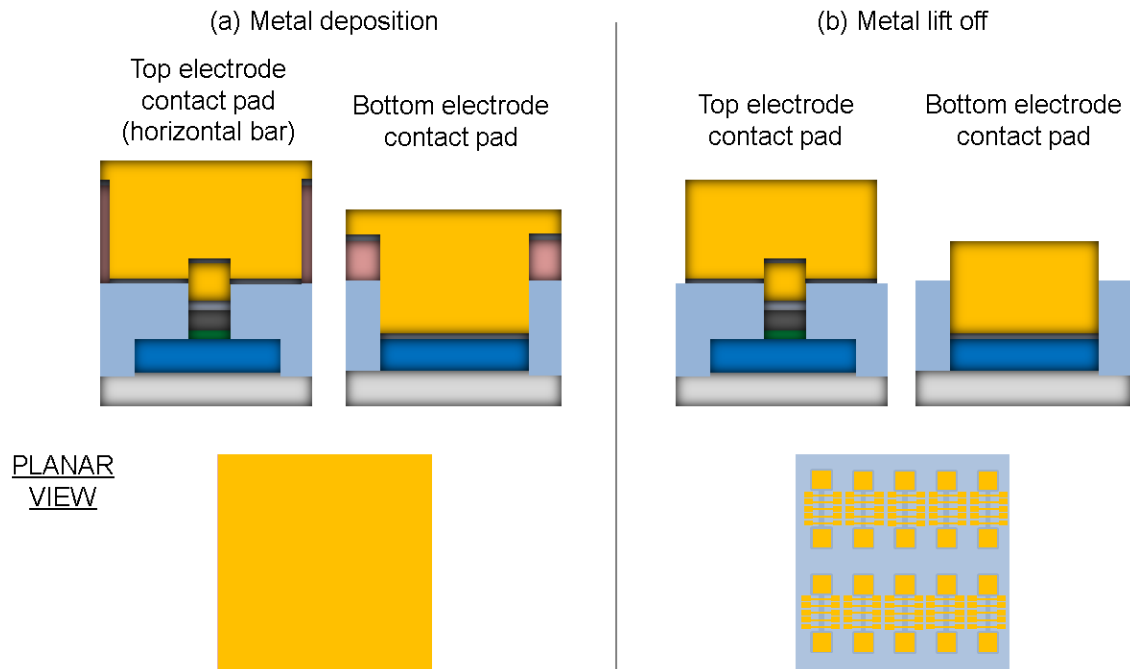**Figure A.11**. (a) Deposit 5 nm of Cr followed by 100 nm of Au. (b) Soaking in acetone for metal liftoff removes remaining resist and metal above it forming distinct contact pads. Final structure.

E-beam evaporation is used to deposit a 5 nm Cr adhesion layer followed by 100 nm of Au. The stated Au thickness is a baseline value and is adjusted as deemed necessary. At the completion of the deposition, samples are removed from handle wafer and soaked in acetone for at least an hour. During the acetone soak, samples are gently agitated to facilitate liftoff. Before the samples are removed from the acetone, they are sonicated very quickly (1-2 seconds) to accelerate liftoff in problematic areas. This must be done with care as sonicating can remove the metallic contact pads. Upon removal samples are rinsed with isopropanol and dried with an N_2 gun.

Chapter One

[1] N. A. Spaldin, in Magnetic Materials: Fundamentals and Applications, (Cambridge University Press, New York, 2003).

[2] S. Chikazumi, in Physics of Ferromagnetism, (Oxford University Press, Oxford, 2009).

[3] B. D. Cullity, in Introduction to Magnetic Materials, (Addison-Wesley, Reading, MA, 1972).

[4] P. A. Cox, in Transition Metal Oxides, (Oxford University Press, New York, 1992).

[5] J. D. Dunitz and L. E. Orgel, J. Phys. Chem. Solids **3**, 318 (1957).

[6] C. J. Ballhausen, J. Dan. Mat. Fys. Medd. **29**, (1954).

[7] F. A. Cotton, in Chemical Applications of Group Theory, (Wiley, New York, 1990).

[8] J. D. Dunitz and L. E. Orgel, J. Phys. Chem. Solids **3**, 20 (1957).

[9] R. C. O'Handley, in Modern Magnetic Materials, (Wiley, New York, 2000).

[10] A. Navrotsky and O. J. Kleppa, J. Inorg. Nucl. Chem. **29**, 2701 (1967).

[11] T. A. Kaplan, Phys. Rev. **116**, 888 (1959).

[12] A. P. Ramirez, in Handbook of Magnetic Materials, edited by K. J. H. Busch (Elsevier Science, Amsterdam, 2001).

[13] F. Nori and A. Tonomura, Science. **311**, 344 (2006).

[14] E. Prince, Acta Crystallogr. **10**, 554 (1957).

[15] S- H. Lee, et al., J. Phys. Soc. Jpn. **79**, 011004 (2010).

[16] H. Takagi and S. Niitaka, in Introduction to Frustrated Magnetism**,** edited by C. Lacroix, F. Mila, P. Mendels (Springer, Berlin, 2011).

[17] J. Smit and H. P. J. Wijn, in Ferrites, (Wiley, New York, 1959).

[18] J. B. Goodenough, in Magnetism and the Chemical Bond, (Krieger, New York, 1976).

Chapter Two

[1] R. Ramesh, O. Auciello, V. G. Keramidas, R. Dat, in Science and Technology of Electroceramic Thin Films, edited by O. Auciello, R. Waser (Kluwer, Dordrecht, The Netherlands, 1995).

[2] D. H. Lowndes, D. B. Geohegan, A. A. Puretzky, D. P. Norton, and C. M. Rouleau, Science **273**, 898 (1996).

[3]   D. P. Norton, Mat. Sci. Eng. R **43**, 139 (2004).

[4] P. R. Willmott, Prog. Surf. Sci. **76**, 163 (2004).

[5] M. Mayer, SIMNRA version 6.05 User's Guide, (Max-Planck-Institut für Plasmaphysik, Garching, Germany, 2009).

[6] J. Stöhr and H.C. Siegmann, in Magnetism: From Fundamentals to Nanoscale Dynamics, (Springer-Verlag, Berlin Heidelberg, 2006).

[7] B. B. Nelson-Cheeseman, University of California, 2009.

Chapter Three

[1]   J. M. Iwata-Harms, F. J. Wong, U. S. Alaan, B. J. Kirby, J. A. Borchers, M. F. Toney, B. B. Nelson-Cheeseman, M. Liberati, E. Arenholz, and Y. Suzuki, Phys. Rev. B **85**, 214424 (2012).

[2] J. M. Iwata, R. V. Chopdekar, F. J. Wong, B. B. Nelson-Cheeseman, E. Arenholz, and Y. Suzuki, J. Appl. Phys. **105**, 07A905 (2009).

[3] A. P. Ramirez, in Handbook of Magnetic Materials, edited by K. J. H. Busch (Elsevier Science, Amsterdam, 2001).

[4] J. M. Hastings and L. M. Corliss, Phys. Rev. **126**, 556 (1962).

[5] N. Menyuk, K. Dwight, and A. Wold, J. Phys. **25**, 528 (1964).

[6] G. Shirane, D. E. Cox, and S. J. Pickart, J. Appl. Phys. **35**, 954 (1964).

[7] E. Prince, Acta Crystallogr. **10**, 554 (1957).

[8] K. Tomiyasu and I. Kagomiya, J. Phys. Soc. Jpn. **73**, 2539 (2004).

[9] A. Navrotsky and O. J. Kleppa, J. Inorg. Nucl. Chem. **29**, 2701 (1967).

[10] T. A. Kaplan, Phys. Rev. **116**, 888 (1959).

[11] S. -H. Lee, H. Takagi, D. Louca, M. Matsuda, S. Ji, H. Ueda, Y. Ueda, T. Katsufuji, J.- H. Chung, S. Park, S. - W. Cheong, and C. Broholm, J. Phys. Soc. Jpn. **79**, 011004 (2010).

[12] Y. Yamasaki, S. Miyasaka, Y. Kaneko, J. - P. He, T. Arima, and Y. Tokura, Phys. Rev. Lett. **96**, 207204 (2006).

[13] C. Ederer and M. Komelj, Phys. Rev. B **76**, 064409 (2007).

[14] Y. Tokura and S. Seki, Adv. Mater. **22**, 1554 (2010).

[15] S. Bordács, D. Varjas, I. Kézsmárki, G. Mihály, L. Baldassarre, A. Abouelsayed, C. A. Kuntscher, K. Ohgushi, and Y. Tokura, Phys. Rev. Lett. **103**, 077205 (2009).

[16] G. Hu and Y. Suzuki, Phys. Rev. Lett. **89**, 276601 (2002).

[17] R. V. Chopdekar, B. B. Nelson-Cheeseman, M. Liberati, E. Arenholz, and Y. Suzuki, Phys. Rev. B **83**, 224426 (2011).

[18] J. M. Iwata, R. V. Chopdekar, B. B. Nelson-Cheeseman, F. J. Wong, U. S. Alaan, K. M. Yu, C. A. Jenkins, E. Areholz and Y. Suzuki, (unpublished).

[19] M. Bibes, J. E. Villegas, A. Barthélémy, Adv. Phys. **60**, 5 (2011).

[20] M. G. Blamire, J. L. MacManus-Driscoll, N. D. Mathur, Z. H. Barber, Adv. Mater. **21**, 3827 (2009).

[21] A. Grutter, F. Wong, E. Arenholz, M. Liberati, A. Vailionis and Y. Suzuki, Appl. Phys. Lett. **96**, 082509 (2010).

[22] S. Miyahara and H. Ohnishi, J. Phys. Soc. Jpn. **11**, 1296 (1956).

[23] Y. Yafet and C. Kittel, Phys. Rev. **87**, 290 (1952).

[24] J. D. Dunitz and L. E. Orgel, J. Phys. Chem. Solids **3**, 20 (1957).

[25] Yu. S. Dedkov, A. S. Vinogradov, M. Fonin, C. König, D. V. Vyalikh, A. B. Preobrajenski, S. A. Krasnikov, E. Yu. Kleimenov, M. A. Nesterov, U. Rüdiger, S. L. Molodtsov, and G. Güntherodt, Phys. Rev. B **72**, 060401(R) (2005).

[26] M. Grioni, J. B. Goedkoop, R. Schoorl, F. M. F. de Groot, J. C. Fuggle, F. Schäfers, E. E. Koch, G. Rossi, J.-M. Esteva, and R. C. Karnatak, Phys. Rev. B **39**, 1541 (1989).

[27] B. B. Nelson-Cheeseman, R. V. Chopdekar, M. F. Toney, E. Arenholz, and Y. Suzuki, J. Appl. Phys. **111**, 093903 (2012).

[28] C. F. Majkrzak, Physica B **221**, 342 (1996).

[29] C. F. Majkrzak, K. V. O'Donovan, and N. Berk, in Neutron Scattering from Magnetic Materials, edited by T. Chatterji (Elsevier Science, New York, 2005).

[30] B. J. Kirby, D. Kan, A. Luykx, M. Murakami, D. Kundaliya, and I. Takeuchi, J. Appl. Phys. **105**, 07D917 (2009).

[31] V. F. Sears, in International Tables for Crystallography, edited by E. Prince, (Wiley, New York, 2006).

[32] In order to maintain beam polarization, the measurements were limited to fields below 700 mT. Hence reported PNR magnetization values are not obtained at saturation.

[33] J. B. Goodenough, in Magnetism and the Chemical Bond, (Krieger, New York, 1976).

[34] T. A. Kaplan, K. Dwight, D. Lyons, and N. Menyuk, J. Appl. Phys. **32**, S13 (1961).

Chapter Four

[1] C. Chappert, A. Fert, F. Nguyen Van Dau, Nature Mater. **6**, 813-823 (2007). .

[2] M. Jullière, Phys. Lett. **54A**, 225 (1975).

[3] E. J. W. Verwey, Nature **144**, 327-328 (1939).

[4] E. J. W. Verwey and P. W. Haayman, Physica **8**, 979-987 (1941).

[5] G. Hu and Y. Suzuki, Phys. Rev. Lett. **89,** 276601-1-4 (2002).

[6] L. M. B. Alldredge, R. V. Chopdekar, B. B. Nelson-Cheeseman, Y. Suzuki, Appl. Phys. Lett. **89**, 182504 (2006).

[7] B. B. Nelson-Cheeseman, R. V. Chopdekar, L. M. B. Alldredge, J. S. Bettinger, E. Arenholz, Y. Suzuki, Phys. Rev. B **76**, 220410(R) (2007).

[8] S. S. P. Parkin, C. Kaiser, A. Panchula, P. M. Rice, B. Hughes, M. Samant, and S.-H. Yang, Nat. Mater. **3** 862-867 (2004).

[9] J. S. Moodera and G. Mathon, J. Magn. Magn. Mater. **200**, 248-273 (1999).

[10] A. F. Panchula, Stanford University, 2003.

[11] A. Chainani, T. Yokoya, T. Morimoto,T. Takahashi, S. Todo, Phys. Rev. B 51, 17976-17979 (1995).

[12] J.-H. Park, L. H. Tjeng, J. W. Allen, P. Metcalf and C. T. Chen, Phys. Rev. B **55**, 12813-12817 (1997).

[13] L. M. B. Alldredge, Cornell University, 2006.

[14] A. Saffarzadeh, J. Magn. Magn. Mater. **269**, 327-332 (2004).

[15] T. Nagahama, T. S. Santos, and J. S. Moodera, Phys. Rev. Lett. **99**, 016602 (2007).

[16] A. V. Ramos, M.-J. Guittet, J.-B. Moussy, R. Mattana, C. Deranlot, F. Petroff, C. Gatel, Appl. Phys. Lett. **91**, 122107 (2007).

[17] G. Hu, Cornell University, 2003.

[18] R. V. Chopdekar, B. B. Nelson Cheeseman, M. Liberati, E. Arenholz, Y. Suzuki, Phys. Rev. B **83**, 224426 (2011).

[19] E. Prince, Acta Crystallogr. **10**, 554 (1957).

[20] Yu. S. Dedkov, A. S. Vinogradov, M. Fonin, C. König, D. V. Vyalikh, A. B. Preobrajenski, S. A. Krasnikov, E. Yu. Kleimenov, M. A. Nesterov, U. Rüdiger, S. L. Molodtsov, G. Güntherodt, Phys. Rev. B **72**, 060401(R) (2005).

[21] M. Grioni, J. B. Goedkoop, R. Schoorl, F. M. F. de Groot, J. C. Fuggle, F. Schäfers, E. E. Koch, G. Rossi, J.-M. Esteva, R. C. Karnatak, Phys. Rev. B **39**, 1541 (1989).

[22] R.V. Chopdekar, M. Liberati, Y. Takamura, L. F. Kourkoutis, J. S. Bettinger, B. B. Nelson-Cheeseman, E. Arenholz, A. Doran, A. Scholl, D. A. Muller, Y. Suzuki, J. Magn. Magn. Mater. **322**, 2915-2921 (2010).

[23] N. Menyuk, A. Wold, D. B. Rogers, K. Dwight, J. App. Phys. supp. **33**, 1144 (1962).

[24] B.B. Nelson-Cheeseman, R. V. Chopdekar, M. F. Toney, E. Arenholz, Y. Suzuki, J. App. Phys. **111**, 093903 (2012).

[25] M. Robbins, G. K. Wertheim, R. C. Sherwood, D. N. E. Buchanan, J. Phys. Chem. Solids **32**, 717-729 (1971).

[26] J. M. Iwata-Harms, F. J. Wong, U. S. Alaan, B. J. Kirby, J. A. Borchers, M. F. Toney, B. B. Nelson-Cheeseman, M. Liberati, E. Arenholz, and Y. Suzuki, Phys. Rev. B **85**, 214424 (2012).

[27] V. Garcia, M. Bibes, A. Barthélémy, M. Bowen, E. Jacquet, J. − P. Contour, and A. Fert, Phys. Rev. B **69,** 052403 (2004).

[28] J. S. Moodera and G. Mathon, Annu. Rev. Mater. Sci. **29**, 381-432 (1999).

[29] D. Ephron, Stanford University, 1996.

[30] D. Ihle and B. Lorenz, J. Phys. C **19**, 5239 (1986).

[31] S. K. Park, T. Ishikawa, Y. Tokura, Phys. Rev. B, **58** 3717-3720 (1998).